# Application of Micromachined Structures to the Study of Mechanical Properties and Adhesion of Thin Films

*by*

Mehran Mehregany

B.S.E.E., University of Missouri–Columbia

(1984)

*submitted in partial fulfillment*

*of the requirements for the degree of*

MASTER OF SCIENCE

IN ELECTRICAL ENGINEERING AND COMPUTER SCIENCE

*at the*

MASSACHUSETTS INSTITUTE OF TECHNOLOGY

May 23, 1986

©1986 Massachusetts Institute of Technology

Signature of Author ____________________
Department of Electrical Engineering and Computer Science
May 23, 1986

Certified by ____________________
Stephen D. Senturia
Thesis Supervisor

Accepted by ____________________
Arthur C. Smith
Chairman, Departmental Committee on Graduate Students

MASSACHUSETTS INSTITUTE OF TECHNOLOGY

Archives JUL 23 1986

LIBRARIES

# Application of Micromachined Structures to the Study of Mechanical Properties and Adhesion of Thin Films

by

Mehran Mehregany

Submitted to the Department of Electrical Engineering
and Computer Science on 23 May 1986 in partial
fulfillment of the requirements for the Degree of
Master of Science in Electrical Engineering and Computer Science

## Abstract

A set of structures are designed and fabricated which can characterize the mechanical properties of thin films *in situ*. Quantitative measurements were obtained for BTDA-ODA/MPDA polyimide on silicon for the film's residual stress, elastic modulus, and the elongation at break. These measurements are reliable and reproducible. Suspended polyimide membranes are used in the blister test to measure the work of adhesion of polyimide to silicon dioxide quantitatively.

Silicon micromachining constitutes the basis of the technique for sample fabrication. A 50-50 hydrazine-water solution was used for anisotropic etching of silicon. The etching characteristics of this solution were studied in detail. Micromechanical structures including thin silicon diaphragms, beams, bridges, and fibers were fabricated to show the feasibility of silicon micromachining using Hydrazine. A reliable method was developed for coating and pattering of wafers with thin membranes.

Thesis Supervisor: Stephen D. Senturia
Title: Professor of Electrical Engineering and Computer Science

# Acknowledgements

It is a pleasure to acknowledge the following people who have contributed to this research:

Professor Stephen D. Senturia, who provided not only the key ideas, keen insight and professional guidance that made this work possible, but also a humane and friendly atmosphere that led to a fruitful education at M.I.T.

Professor Rodger T. Howe who initially conceived the idea of released structures (chapter 5) and provided valuable guidance throughout.

Professor David Edell who provided valuable suggestions for the Hydrazine anisotropic etching studies presented in the second chapter of this document.

My graduate student co-workers: Marty Schmidt for technical discussions and Mark Allen for his collaboration on suspended membrane studies (chapter 4).

The staff of the M.I.T. Microelectronics Laboratory for their valuable guidance in processing.

3M Corporation for sponsoring this work through a graduate fellowship.

Dr. Soraya and Javad Kashani for their support throughout my graduate studies.

My family for their loving support and encouragement.

# Dedication

*to Vafa*

# Contents


Abstract 1

Acknowladgements 2

1 Introduction 8

2 Hydrazine Characterization 11

2.1 High Concentration Boron Deposition . . . . . . . . . . . . . . . . . 12

2.2 Why Hydrazine ? . . . . . . . . . . . . . . . . . . . . . . . . . . 15

2.3 Etching Reactor Design . . . . . . . . . . . . . . . . . . . . . . 16

2.4 Safety Precautions . . . . . . . . . . . . . . . . . . . . . . . . 16

2.5 Hydrazine Etching Characteristics . . . . . . . . . . . . . . . . . 18

2.6 Appropriate Masks for Hydrazine . . . . . . . . . . . . . . . . . . 25

3 Silicon Micromachining 27

3.1 Boron Doped Silicon Diaphragms . . . . . . . . . . . . . . . . . . 27

3.2 Silicon Diaphragm Pressure Transducer . . . . . . . . . . . . . . . 34

3.3 Under Etching by Hydrazine . . . . . . . . . . . . . . . . . . . . 36

3.4 Thin Silicon Fibers . . . . . . . . . . . . . . . . . . . . . . . . 42

3.5 Suspended Polyimide Membranes . . . . . . . . . . . . . . . . . . 47

3.6 Fabrication of Released Structures . . . . . . . . . . . . . . . . . 51

4 Suspended Membranes 54

4.1 Load-deflection Behavior of Suspended Membranes . . . . . . . . . . 54

4.2 Mechanics of Blister Test . . . . . . . . . . . . . . . . . . . . . 61

4.3 Experimental Instrumentation . . . . . . . . . . . . . . . . . . . 64

4.4 Calibration of the Pressure Transducers . . . . . . . . . . . . . . . 66

4.5 Load-deflection Measurement Methodology . . . . . . . . . . . . . . 66

4.6 Suspended Membrane Load-Deflection Results . . . . . . . . . . . . 68

4.7 Adhesion Measurement Methodology . . . . . . . . . . . . . . . . . 74

4.8 Polyimide-Silicon Dioxide Adhesion Data . . . . . . . . . . . . . . 76

5 Released Structures 81

5.1 T-shape Polyimide Structures . . . . . . . . . . . . . . . . . . . 86

5.2 Fixed-end Polyimide Beams . . . . . . . . . . . . . . . . . . . . 97

5.3 Short Polyimide Cantilever Beams . . . . . . . . . . . . . . . . . . . . 105
5.4 Overall View of the Released Structures . . . . . . . . . . . . . . . . . 107

**6 Conclusion** **109**

**Appendices** **110**

**A Boron Spreading Resistance Data** **110**

**B Etching System Parts** **116**

**C Silicon Diaphragm Fabrication** **117**

**D Micromachining by Under-etching** **120**

**E Fabrication of Silicon Fibers** **123**

**F Fabrication of Polyimide Membranes** **126**

**G Fabrication of Released Structures** **128**

**References** **131**

# List of Figures


1 Sheet resistance profiles from solid source boron deposition at 1175°C . . . 14
2 Reflux system for Hydrazine etching . . . 17
3 Silicon etch rates in Hydrazine . . . 21
4 Effect of Hydrazine aging on (110) silicon etch rate . . . 23
5 Angle lapping technique for measuring the stop layer thickness . . . 26
6 Thin silicon diaphragm fabrication steps . . . 29
7 SEM of a 4.7 $\mu$ thick, 1x1 mm, silicon diaphragm from the back . . . 31
8 Magnified corner of figure 7 . . . 31
9 SEM of the same silicon diaphragm as in figure 7 at an angle . . . 32
10 SEM of figure 8 at an angle . . . 32
11 SEM of the same silicon diaphragm as in figure 10 with back oxide removed . . . 33
12 Photograph of a 2800 Å, 1x1 mm, oxide diaphragm from the back . . . 33
13 Pressure measurement set-up for the silicon pressure transducer . . . 34
14 Static pressure response of the silicon diaphragm pressure transducer . . . 35
15 Fabrication of a silicon cantilever beam by under-etching . . . 37
16 SEM photograph of a wide silicon cantilever beam . . . 39
17 Magnified view of a beam corner in figure 16 . . . 39
18 SEM photograph of a silicon torsional mirror . . . 40
19 SEM photograph of a silicon bridge . . . 40
20 SEM of an etched + sign showing the corner rounding due to diffusion . . . 41
21 SEM photograph of a silicon plate held by four necks . . . 41
22 Fabrication steps for thin silicon fibers . . . 43
23 SEM picture of many fibers attached to the frame on one side . . . 44
24 Top view of three fibers connected to the support frame . . . 45
25 SEM picture showing the flexibility of the thin silicon fibers . . . 45
26 SEM picture of the side-wall of a thin silicon fiber . . . 46
27 Fabrication process for polyimide diaphragms . . . 48
28 Top part of the vacuum spinning chuck . . . 49
29 Bottom part of the vacuum spinning chuck . . . 50
30 Fabrication process for a suspended polyimide structure . . . 52
31 SEM photograph of several suspended structures . . . 53

32 Load-deflection behavior of a circular membrane under uniform pressure . . . 56
33 Description of parameters for a circular membrane . . . 58
34 The membrane testing assembly . . . 65
35 Calibration of pressure sensors . . . 67
36 Typical load-deflection data for six different size membranes . . . 71
37 Consecutive load-deflection measurements on sample #12 . . . 73
38 Typical data for blister pressure versus injected air volume . . . 75
39 Peel data for the first sample . . . 78
40 Peel data for the second sample . . . 79
41 Apparent re-adherence after peel . . . 80
42 Various structures before and after release . . . 82
43 Released 8.0 micron thick couple-loaded polyimide plate . . . 84
44 Magnified view of the rotated plate . . . 84
45 Released 8.0 micron thick transverse loaded polyimide beam . . . 85
46 Released 8.0 micron thick supported plate structure . . . 85
47 Parameter description for the T structure . . . 87
48 SEM of a released 5.5 micron thick T structure . . . 90
49 Magnified view of the cross-bar region . . . 90
50 Improved structure for more accurate deflection measurement . . . 93
51 A shear sensitive structure for measurements of Poisson's ratio . . . 95
52 Parameter description for the fixed end beam . . . 98
53 A typical released fixed-end beam . . . 102
54 A magnified view of the displaced width-change boundary . . . 102
55 Breaking the film by exceeding its ultimate strain . . . 104
56 Seven micron thick polyimide cantilever beams . . . 106

# List of Tables


1 Angle lap data for several samples . . . . . . . . . . . . . . . . . . . . 26
2 Residual stress and modulus data . . . . . . . . . . . . . . . . . . . . . . 69
3 Data on slender-beam T structures . . . . . . . . . . . . . . . . . . . . . 91
4 Data on stocky-beam T structures . . . . . . . . . . . . . . . . . . . . . 91
5 Data on fixed end beam structures . . . . . . . . . . . . . . . . . . . . . 101
6 Data for the polyimide cantilever beams . . . . . . . . . . . . . . . . . . 106

# 1 Introduction

The importance of mechanical properties of VLSI materials, in particular thin films, are well known in integrated circuit fabrication and packaging. Large stresses in thin films and insulating layers can cause cracking and adhesive or cohesive failure, leading to component failure. Stress relaxation due to creep can alter device performance in time. Loss of adhesion in multilayer structures causes performance failure. Adhesion degradation of passivation layers leads to corrosion.

An understanding of the mechanical properties of thin films is becoming even more essential with the rapid growth of solid state sensor applications. The ability to fabricate many micromechanical structures depends greatly on the mechanical characteristics of the material. Structures fabricated from films with compressive stress can buckle, causing undesirable deformations. On the other hand, structures made of materials with tensile stress demonstrate significant performance deviation from the expected performance for the material with zero stress (i.e. thin silicon diaphragm pressure sensors in which the diaphragm is under tension).

To fully characterize the mechanical properties of a thin film material, the stress in the film, Young's Modulus and Poisson's ratio of the film, and the yield stress and ultimate strength of the film should be determined. In addition, effects such as fatigue and creep must be studied. In general, it is more difficult to make such measurements in polymeric thin films. The final mechanical properties of these films depend on the exact molecular formulation and the details of the curing process. Environmental factors such as moisture absorption can have significant influences on the mechanical properties in time. Polymer films may be viscoelastic which might complicate such studies even further. With the increasing application of polymer films to microelectronics, it is necessary to study the mechanical properties of these films.

Adhesion tests are usually destructive, and seldom quantitative [1]. The widely used peel tests measure the force necessary to overcome the adhesive bond, and are complicated both by elastic and plastic deformation of the film.

Studies of mechanical properties have only concentrated on measuring the stress in thin films. The basic technique is to deposit the film of interest on the substrate and measure the stress-induced curvature of the substrate [2,3]. The curvature of the substrate is typically detected optically using either a laser beam deflection system or an interferometric technique such as Newton's rings. It is evident that

the measured stress would be an average stress in the film. In addition, the degree of the induced curvature depends on the flexural rigidity of the thin film and the substrate and on the stress in the thin film. For VLSI materials where the substrate is normally silicon, substantially thicker than the thin film, the induced curvatures are small and difficult to measure accurately. To overcome this problem, thin films are deposited on other thin substrates. However, this alters the system of interest and measurements made on this system may not correspond to the ones where the thin film is on silicon. Finally, using this technique, many other parameters of interest are not addressed, and elaborate experimental instrumentation for curvature measurements is needed.

In this work, a different approach is taken in studying mechanical properties and adhesion of polyimide films. The approach is to remove the substrate from under the film in particular areas, where the measurements are to be conducted. Suspended membranes of polyimide are fabricated and the stress and the modulus of the film are measured by load-deflection studies. In some cases, the film is patterned to particular structural shapes that are sensitive to the mechanical properties of interest. The removal of the substrate releases the structures (referred to as "released structures") which then deform as predicted by the mechanical properties of the film.

The adhesion of polyimide to silicon dioxide is studied using the Blister method [4] which was previously demonstrated by Hinkley [5] to be of value in studying adhesion of polymer films quantitatively. In this work, the adhesion test sites (thin film membranes) are fabricated by a lithographic technique. The test is preformed by injection of known quantities of air under the blister rather than by applying a constant pressure for peeling the film. This eliminates the problem of uncontrollable peel, characteristic of a constant pressure peel.

Silicon Micromachining was used as the technique for removing the substrate in selective areas. An anisotropic etch was characterized and used that is less throughly studied than EDP and KOH. This etchant is a 50-50 hydrazine water solution. The details in operating this anisotropic etching system are explained. Processes for fabrication of the thin polymer membranes and the released structures are designed and implemented. The silicon micromachining techniques are used to fabricate other silicon microstructures such as diaphragms, beams, bridges, and fibers. Applications for these structures are considered.

Chapter 2 explains in detail the anisotropic etching system used in this work.

Chapter 3 reviews the fabricated structures and the fabrication processes (detailed process recipes are available in the Appendices). Chapter 4 discusses the load-deflection and adhesion studies on suspended polyimide membranes. Chapter 5 covers the design, analysis, and measurements on the released structures. Chapter 6 contains an overview of the work.

The suspended membrane studies (chapter 4) were done in collaboration with Mark Allen [6]. Sample fabrication was the responsibility of this author. The experimental instrumentation and measurements were joint efforts, while the modeling was carried out by Allen.

# 2 Hydrazine Characterization

Anisotropic etching of crystalline silicon resulting from differential etch rates along various crystallographic directions has been used to fabricate a variety of active and passive three dimensional device structures including X-ray masks [7]–[12], optical waveguides [13]–[16], high resolution patterns [17]–[21], nozzles [22]–[26], microtools [27], diodes [28], bipolar and MOS circuits [29]–[35], electromechanical and micromechanical [36]–[42] devices. The most commonly used anisotropic etchants of silicon are potassium hydroxide (KOH) [43]–[47] and ethylenediamine-pyrocatechol-water solution (EDP) [48]–[57]. Several extensive reviews [58]–[62] of basic techniques, etchant properties, and novel structures fabricated are available.

The anisotropic etchants etch the (100) and (110) directions rapidly while etching the (111) direction slowly. For KOH, the etchant composition is typically 44 grams of potassium hydroxide and 100 ml of water [60]. The etch rate of this solution in the (100) direction is 1.4 micron/min at 85$^0$C. For KOH solutions, etch rate ratios of 400/1 for (100)/(111) [60] and 600/1 for (110)/(111) [59] are reported. EDP etchant composition is typically 750 ml of ethylenediamine, 120 grams of pyrocatechol, and 240 ml of water [60]. The etch rate for this solution is about 1.25 $\mu$/min at 115°C with an etch rate ratio of 35/1 for (100)/(111). The etching process using KOH or EDP can be significantly slowed down by doping the sample with high concentrations of boron. While the etch rate of EDP drops to nearly zero for substrates with boron doping greater than 7x$10^{19}$ $cm^{-3}$ [50,51,57], for KOH, a boron doping of higher than $10^{20}$ $cm^{-3}$ is required to drop the etch rate by a factor of twenty [60].

In this work, high temperature boron solid sources supplied by Owens Illinois, Inc. [63] are used for boron deposition at 1175°C to create the etch stop regions. In addition, an anisotropic etchant has been studied which has been less throughly investigated than KOH or EDP. This etchant is a mixture of hydrazine and water solution [64]–[67]. The composition is 50% hydrazine and 50% water, and is commercially available [68]. The premixed solution is convenient because it eliminates the need for handling and storing of pure hydrazine. To differentiate between this particular solution and a general hydrazine-water anisotropic etchant of any composition, the capitalized name, Hydrazine, is used when referring to this premixed 50-50 hydrazine-water solution.

In the sections to follow, the boron deposition process is discussed in detail,

and spreading sheet resistance data collected on samples doped for different lengths of time are presented. Advantages and disadvantages of the three etchants, KOH, EDP, and Hydrazine are discussed. A basic reactor design for the Hydrazine etching process is presented. Safety issues related to processing and handling Hydrazine are reviewed. Etch rates for silicon of various resistivities and orientations are studied. The concentration of boron needed to stop the etching process, and appropriate non-organic and metallic masks for the hydrazine water solution are discussed.

## 2.1 High Concentration Boron Deposition

High temperature deposition from solid sources is used to create the boron doped layers which act as etch-stop regions. These solid sources are produced from a glass containing $B_2O_3$ and the oxides BaO, MgO, $Al_2O_3$, and $SiO_2$ and are capable of deposition at the temperature range of 1050 to 1200°C [63]. The operating temperature for deposition was selected to be 1175°C, somewhat below the upper limit of the sources, but high enough for rapid diffusion of boron. At this temperature, the solid solubility limit of boron in silicon is close to $3\text{x}10^{20}$ $cm^{-3}$. The 2 inch diameter sources were used in a 10 cm diameter three zone furnace tube with a nitrogen gas flow of 0.6 SCFH and an oxygen gas flow of 0.07 SCFH. The oxygen added to the carrier gas protects the surface of the wafer from being damaged from the volatile species that are formed at the surface during deposition. In addition, it oxidizes the boron-silicon phase for subsequent removal in HF. This combination of gas flows was empirically found to optimize the deposition level and uniformity without surface damage.

The samples can be loaded and unloaded into and out the furnace at the operating temperature, but this will cause significant warping of the sources and the samples due to the thermal stress. To reduce this damage, the samples are loaded in the furnace at 900°C. The temperature is then ramped to 1175°C in 40 minutes. At the time of unloading, the temperature is ramped down to 900 in 45 minutes and the samples are then unloaded. For a two hour deposition at 1175°C, the additional deposition due to ramping makes a negligible contribution to the doping profile.

A quartz boat recommended for the Boron+ sources is used to hold the sources and samples [69]. Dummy wafers are placed between the sources while they are stored, or when they are not used in a deposition. A maximum of ten wafers can be doped at once while the minimum number is two (back to back). Under the foregoing conditions, when two wafers are placed back to back each facing a source,

there is very little deposition on the backside of the wafers. This eliminates the need for backside removal after deposition. If the gas flow rates are changed, the backside doping may become significant.

To determine the doping profiles that can be achieved by these sources, six 10-20 Ω-cm, n-type, 2 inch silicon samples were doped at 1175°C. The first five were doped for 30, 45, 60, 90, and 120 minutes, respectively. The sixth sample was doped for 120 minutes, but the temperature was ramped as described above. Spreading sheet resistance data for these samples are included in appendix A. Figure 1 shows the high concentration region of five of these profiles. The 120 minutes deposition data is excluded since it corresponds closely to the 120 minutes deposition with temperature ramping.

The measured doping profile cannot be explained by simple diffusion theory for two reasons. First, the deposition is done in an oxidizing ambient; 10% oxygen is added to the carrier gas. This enhances the boron diffusivity in silicon. The second reason is that at high concentrations, the interaction of boron with neutral and positively charged vacancies, $V^{o}$ and $V^{+}$, has to be considered, such that the diffusivity is given by:

$$D = h[D_i^{o} + D_i^{+}(\frac{p}{n_i})], \tag{1}$$

where h is the field enhancement factor, $D_i^{o}$ is the diffusivity due to the neutral vacancies, and $D_i^{+}$ is the diffusivity due to the singly charged vacancies. Qualitatively, the dopant profile is more abrupt than the *erfc* case [70].

These two factors, especially the latter, work to our advantage in making deep, high-concentration boron depositions. As evident from the spreading sheet resistance data, a two hour deposition results in a junction of close to 7.5 $\mu$ deep, which when etched in hydrazine leaves a 4.7 $\mu$ thick silicon diaphragm behind. If the high concentration of boron in the diaphragm is undesirable, it can be reduced by thermal drive out in nitrogen atmosphere. Typically, a drive-out for more than twice the deposition time at the initial diffusion temperature is enough to reduce the boron concentration to below $10^{16}$ $cm^{-3}$ [28].

The described procedure for high temperature boron deposition is very reproducible and reliable. The uniformity of deposition on the same wafer and across the boat are better than 3% and 5% respectively. The reproducibility from deposition to deposition is better than 5% as long as the sources are stored in the furnace. The warping of the sources due to thermal stress cannot be avoided, even though the

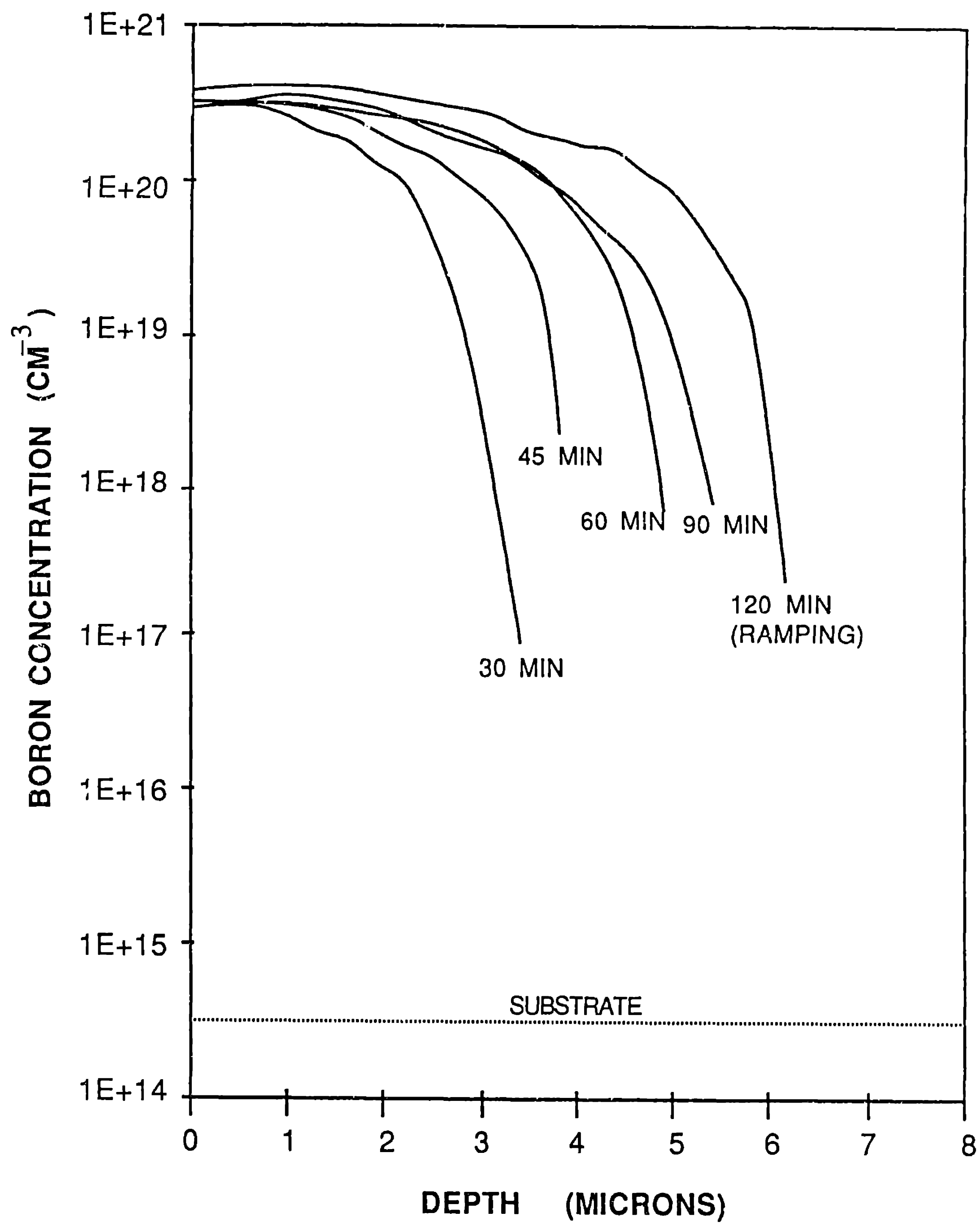


Figure 1: Sheet resistance profiles from solid source boron deposition at 1175 °C

loading and unloading into and from the furnace is done at 900°C and the temperature is then ramped. Warping of the samples is avoided if the temperature ramping procedure is used. Overall, this process is simple and produces very satisfactory results for creating boron doped etch-stop structures.

## 2.2 Why Hydrazine ?

The most commonly used anisotropic etchants of silicon are KOH and EDP. KOH is commonly used for etching (110) oriented substrates and can achieve very high (110)/(111) etch rate ratios. Silicon nitride can be used to effectively mask etching. Three main disadvantages of KOH are significant etching of $SiO_2$, undesirable etching of metallic films, and the potential for potassium contamination of integrated circuit devices that may be on the substrate. EDP is used to avoid the former and the latter problems. Even though EDP does not attack most metallic films, it does etch aluminum rapidly. The etch ratios attainable by EDP for (100)/(111) and (110)/(111) are not nearly as high as what can be done with KOH. When using EDP, etching has to be done in a specific temperature range to avoid formation of undesirable precipitates. In addition, the solution is very dark colored, which makes visual monitoring of the samples difficult as etching proceeds. It leaves a permanent yellowish color deposit on the glassware and in the air hood area. EDP is carcinogenic and extreme care must be taken to avoid endangering the operators' health.

All but one of the cited problems with EDP can be avoided by using a hydrazine based anisotropic etchant (in particular, Hydrazine etch described previously is used in this work). The etch rates of $Si_3N_4$ and $SiO_2$ in Hydrazine are very small. Metallic films are not attacked by hydrazine. No precipitates result during etching. No deposits are detected on the glassware or the air hood area. The color of the solution is clear which makes visual monitoring of the samples possible as etching proceeds. The etch rate of a moderately doped (100) oriented silicon is higher for Hydrazine as compared to EDP at the same etching temperature. Unfortunately, the etch rate ratios for (100)/(111) and (110)/(111) for Hydrazine are not as good as for EDP and KOH. Solutions containing hydrazine, in addition to being carcinogenic, can also be explosive at high hydrazine concentrations. The 50-50 solution, Hydrazine, is claimed to be stable because of the degree of dilution [68].

Because of its many advantages over KOH and EDP, Hydrazine was selected in this work. A basic reflux reactor, described next, is used for etching. The safety

issues for the process and handling are then reviewed. The last sections present the characterization of the particular etch solution used in this work.

## 2.3 Etching Reactor Design

Hydrazine is used in a standard reflux system shown in figure 2. A heating jacket is used to uniformly heat a 1000 ml reflux container fitted with a 13 inch long reflux tower. The reflux container is appropriate for etching 2 or 3 inch diameter substrates. Twenty 2 inch substrates can be fitted in a quartz boat and etched simultaneously. A glass transfer rod shaped to a hook at one end and fitted through the top of the reactor can be used to lower or raise the boat containing the samples into or out of the solution. The reactor is continuously flushed with nitrogen flowing at a rate of 15 $in^3/min$. A thermometer is fitted through the top of the reactor to monitor the temperature of the solution. The individual parts needed for this set-up are listed with part number in appendix B along with information on the supplier.

## 2.4 Safety Precautions

In addition to being a carcinogen, hydrazine can be highly explosive at high concentrations. Hydrazine fumes constitute a serious threat to human health. Studies on laboratory rats have shown that extended exposure to hydrazine can cause nasal tumors. The upper limit of exposure for an eight hour day is recommended not to exceed 0.1 ppm [68]. To avoid exposure, etching should be carried out in a high flow hood environment in a reflux reactor such as the one described in the previous section. Protective clothing consisting of rubber apron, rubber gloves, and goggles should be used by the operator. We recommend a pair of long rubber gloves which covers the operators arms beyond the elbows to protect the arms against the condensation of hydrazine fumes on them. Rubber gloves are not affected by hydrazine, but the permeability of the solution through the gloves over long periods of use is not known. It is recommended to wear disposable gloves underneath the permanent rubber gloves.

Air level monitors with sensitivity of 0.1 ppm are available for detecting hydrazine in the environment or monitoring exposure of the operator [71]. These white paper-like monitors change to yellow when exposed to hydrazine. The shade of the yellow color can be easily compared to the specific color-chart to get a reading. The reactor described in the previous section is set up in a high flow hood.

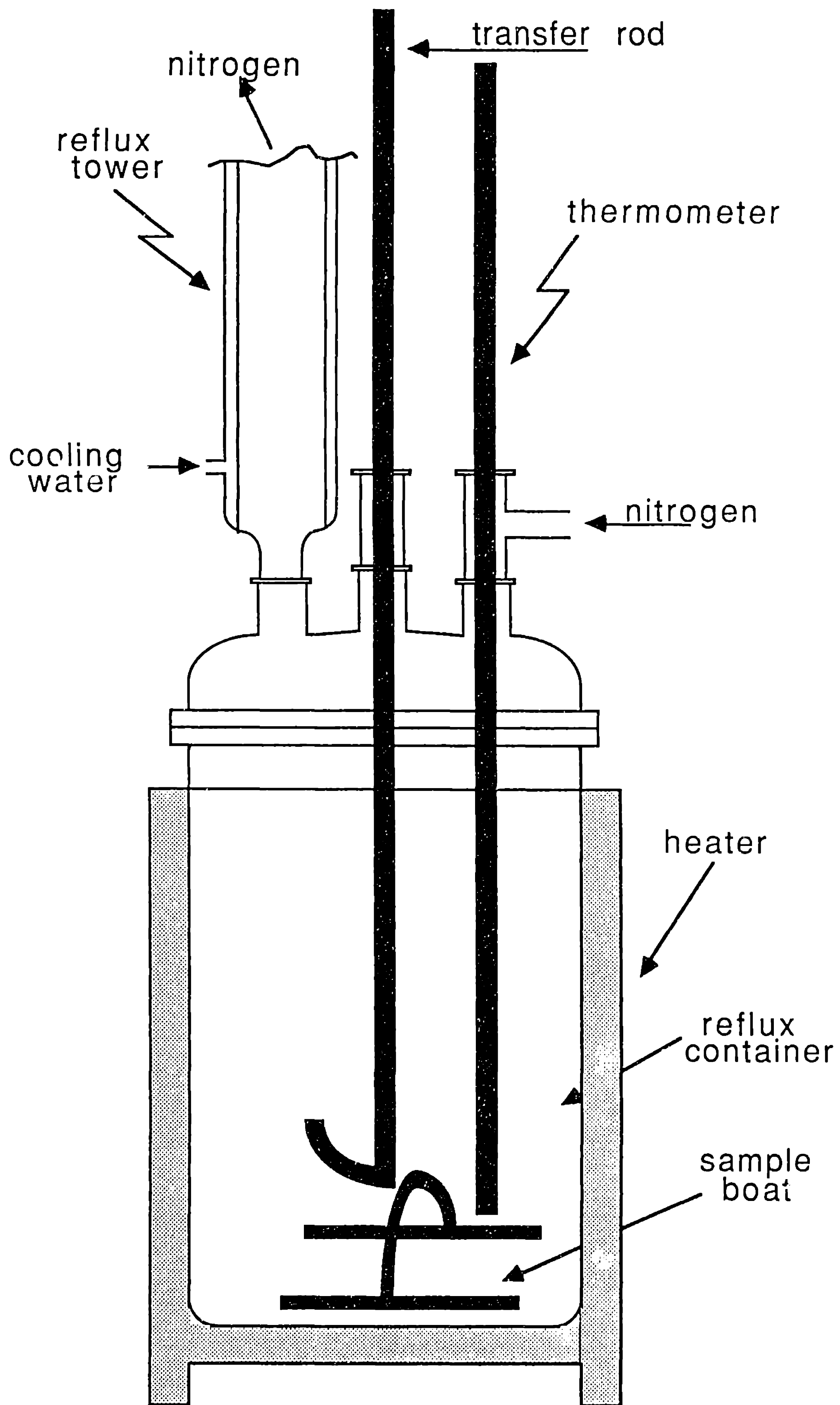


Figure 2: Reflux system for Hydrazine etching

This set up has been used continuously for the past year and no hydrazine contamination has yet been detected by the monitors on the operator or in the lab area outside the hood. If concerned, a mask fitted with ammonia cartridges can be used by the operator at the times of handling hydrazine. The monitors in the hood area instantaneously change color when Hydrazine is introduced into the hood. It is recommended that the reactor is only opened when the temperature of the solution is below 50°C. At higher temperatures, the excessive fumes of hydrazine which are released into the hood area might leak out of the hood and create a hazard. The solution can be poured into the reactor while the boat containing the samples is held above the solution level by the transfer rod. After the desired temperature is reached, the samples can be lowered into the solution. If it is not critical, the samples can be immersed in the cold solution from the start, and the solution is then heated up. At lower temperatures, the etch rate of silicon is small. At the end of etch, the reactor can be lifted out of the heating jacket and immersed in cold water to quickly bring the temperature below 50°C. The samples can be raised out of the solution by the rod or left immersed in hydrazine during the cooling.

After removing the samples from the solution, they should be rinsed (normally with DI water) for at least five minutes. The used hydrazine must be collected and stored for disposal. The reactor components should be throughly rinsed after each run. If this is done with tap water, a final rinse with DI water is necessary. If the reactor components are not kept clean, undesirable precipitates can form on the sides of the reflux container walls. The hydrazine itself should be stored in a vented area, preferably refrigerated.

## 2.5 Hydrazine Etching Characteristics

Even though hydrazine-water solutions are desirable for silicon micromachining, information on etching characteristics of these solutions is scarce. Silicon etch rates in different compositions of hydrazine, iso-2-propyl alcohol, and water have been studied [66]. Another study has focused on etch rates, quality of etched side-walls and bottom surfaces, and corner rounding [67]. In these references, the etch rates have been studied for moderately doped n-type (100) silicon substrates. It is found that a 50% hydrazine and 50% water composition has the highest etch rate and boiling point. This work concentrates on studying the etch rate characteristics of this solution (Hydrazine) which is commercially available [68]. In this section, the etch rate studies of different resistivities and orientations are presented.

To study the effect of resistivity and orientation of the substrate on the etch rate, the following samples were selected: 10-20 Ω-cm boron and phosphorus doped (100), 5-10 Ω-cm boron and phosphorus doped (110) substrates, 3-5 Ω-cm boron doped (111) substrates, and 0.2 Ω-cm antimony doped (100) substrates.

Sample preparation was done in the following way. A native oxide of 3200 angstroms was grown on the sample at 990°C with a combination of 15 minutes dry $O_2$, 45 minutes steam at 95°C, and 15 minutes dry $O_2$. The oxide on the polished surface of the wafers was pattern by standard lithographic techniques to expose a 1x1 inch square window of bare silicon aligned to the wafer flat. The oxide on the back side of the wafer was left intact. The weight of each sample was measured using a Metler balance accurate to $10^{-6}$ grams. Immediately prior to etching, the wafers were given a 20 seconds dip in 20:1 HF and then rinsed with DI water at room temperature.

All the experiments were carried out in the reflux reactor described previously. At the initial stage of the work, the reactor was not flushed with nitrogen during the experiments. The results were not reproducible and the etch rates were lower than expected. The problem was solved by flowing nitrogen through the reactor at the rate of 15 $in^3/min$. For each etching experiment, the boat holding the samples was loaded in the reactor and was held up by the transfer rod such that it would be three inches above the solution initially. 500 ml of Hydrazine at room temperature was funneled in the reflux container from one of the openings through the top of the reactor. The solution was then brought up to the appropriate temperature at which time the samples were lowered in the solution. The samples were etched for the specific length of time and raised out of the solution using the transfer rod. The solution was quickly cooled below 50°C by immersing the reactor into cold water. The samples were removed, rinsed in DI water, and dried. By weighing the samples, the etch rate of the substrates could be measured at the specific etching temperature.

It might be argued that the samples are being etched initially while the solution is being brought up to temperature, due to fume condensation on the samples. However, since the samples are above the solution, their temperature is close to room temperature, at which the etch rate in Hydrazine is negligible compared to the etch rate at the elevated temperature. The same argument can be made for the last stage at which the samples are raised out of the solution and are waiting to be removed after the solution is cooled down. The reason for taking this approach is

to avoid the release of excessive fumes into the hood area by opening the reactor when the solution is hot.

Experiments were done at six temperatures 70, 84, 86, 98.5, 110, 112.5 °C. Each time six sample were etched (one of each resistivity and orientation listed above) using the procedure outlined. At the temperatures above 90°C, the samples were etched for a total of 15 minutes while for the temperatures below 90°C, the samples were etched for 30 minutes. The short times were selected to avoid the possibility of etch rate decrease due to saturation of the solution which was observed when etching large areas of silicon for extended periods.

Figure 3 shows the etch rate data taken for the temperature range 70 to 120°C. No difference was detected in the etch rate of moderately doped n-type and p-type silicon substrates of either (100) or (110) orientation. The activation energy for the moderately doped (100) silicon is 0.28 eV , in good agreement with Lee's results [66], and it is 0.16 eV for moderately doped (110) silicon. The highly doped antimony substrates etched slower than the moderately doped substrates of the same orientation. The activation energy for these substrates is 0.19 eV. The etch rate of the (111) oriented substrates is significantly higher than expected. The activation energy is 0.09 eV for the (111) samples. The etch rate curves should not be extrapolated to predict etch rates below 70°C. From previous work [66], it is expected that the activation energies are different in the temperature range below 50°C.

It is known that the etch rate of highly boron doped silicon substrates is slower in wet chemical anisotropic etchants. This etching behavior has not been explained adequately. Reference [60] discusses two possibilities for this phenomenon. First, at boron concentrations above $5x10^{19}$ $cm^{-3}$ boron enters the lattice interstitially due to high tensile forces created in the lattice because of substitutional boron atoms. The strong B-Si bond tends to bind the lattice more rigidly, increasing the energy required to remove silicon atoms. An alternative explanation is that high enough surface concentrations of boron, converted to boron oxides and hydroxides in an intermediate chemical reaction passivates the surface and prevents the further etching. The fact that KOH is not as effectively stopped by $P^+$ regions together with the fact that KOH attacks oxide supports this explanation. Raley, et. al. [57], have argued that the etch rate is only dependent on hole concentration and not the atomic concentration of boron or stress.

In either of the above cases, for moderately doped samples of either resistivity, no

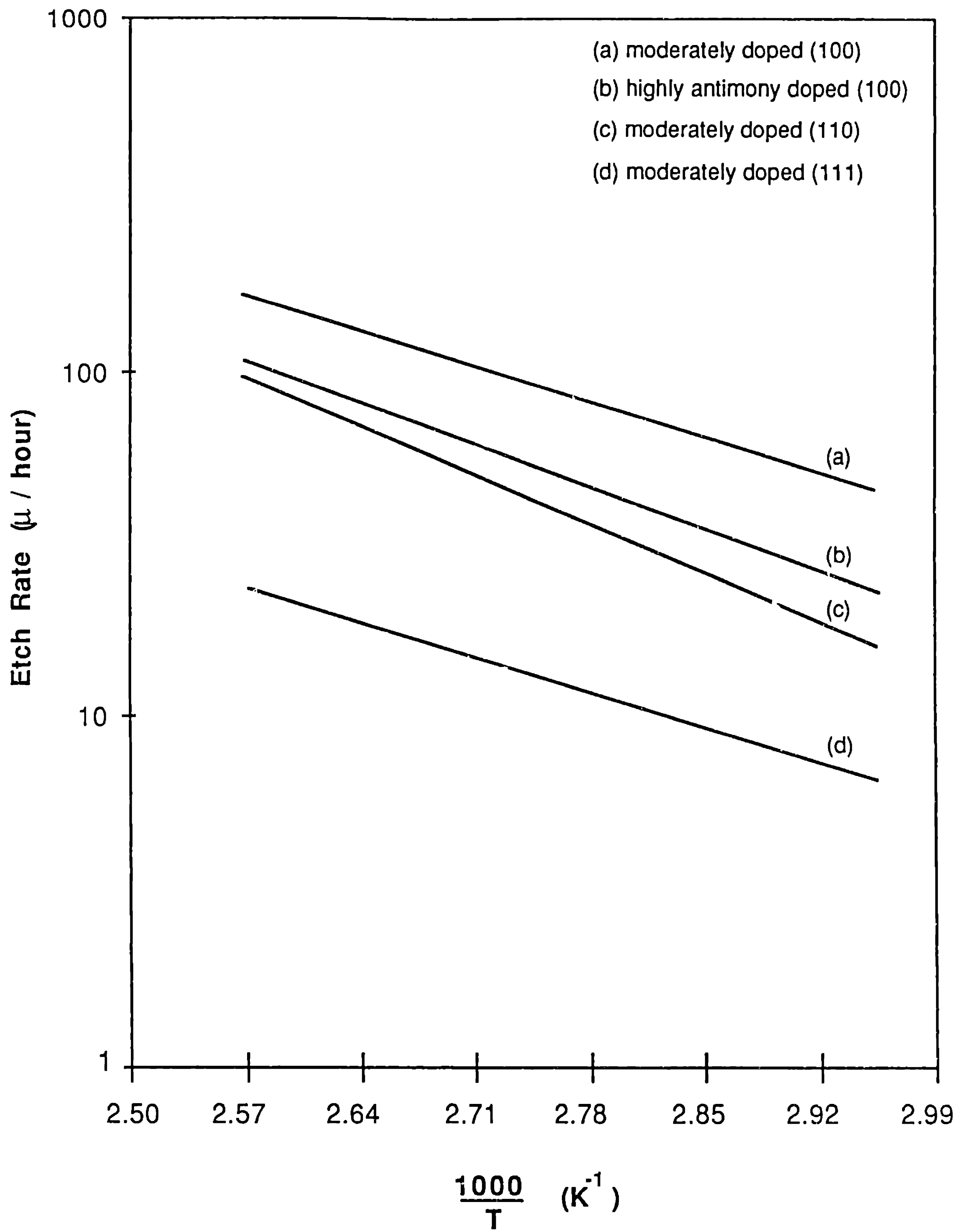


Figure 3: Silicon etch rates in Hydrazine

etch rate difference is expected, which is the observed behavior. The same result is obtained when using EDP solution [52,53]. The slower etch rate of n-type antimony doped samples is puzzling. It may be attributed to the local compressive stresses generated in the lattice due to the large-sized substitutional antimony atoms. This may be contradictory to the findings of Raley, et.al. [57] who propose that the etch rate is only a function of hole concentration. More careful studies are necessary to understand these mechanisms.

The unexpected high etch rates obtained for the (111) samples are attributed to the inaccurate orientation of the substrates. X-ray studies on these samples indicated a tilt of 0.1 degrees in the (111) axis. This would cause an increase in the etch rate measured, which is not truly the etch rate of (111) planes.

To more accurately measure the etch rate for the (111) planes, circular features of 25 $\mu$ diameter were patterned in the oxide on the smooth surface of the wafer. Since the (111) planes etch slowest, the circular openings can be under etched to square features, with the the (111) planes constituting the side-walls of the square pits. By etching the samples for 165 minutes at 118°C in Hydrazine, the under etch of the oxide in the (111) plane directions could be measured accurately. This was done on (100) and (110) substrates with either $SiO_2$ or $Si_3N_4$ used as etch mask. In all cases, the (111) plane etch rate at this temperature was $11 \pm 0.5$ $\mu$/hr. The etch rate ratios of (100) and (110) to (111) for the moderately doped samples are 16 and 9 at 118°C, respectively.

As mentioned above, reproducible etch rate results could only be obtained when the reactor was continuously flushed with nitrogen. In addition, another problem was noticed. The premixed Hydrazine etch is supplied in one gallon size sealed containers. It was found that highest etch rates were attained, when solution from a freshly opened container was used. When the seal on the container was broken and the solution aged, the etch rates dropped, and results were not accurately reproducible. Figure 4 shows etch rate data collected for the (110) samples while the reactor was not flushed with nitrogen and solution from the same container was used for all the temperatures. The data point at 111.5°C was obtained using solution from the container when the seal was just broken. The next point was obtained using solution from the same gallon but five hours latter. An additional five hour period elapsed before the next etch experiment was done. The last point was obtained after twenty four hours had passed since the first point. Data on other samples have the same general trend. Note that even when solution from a freshly

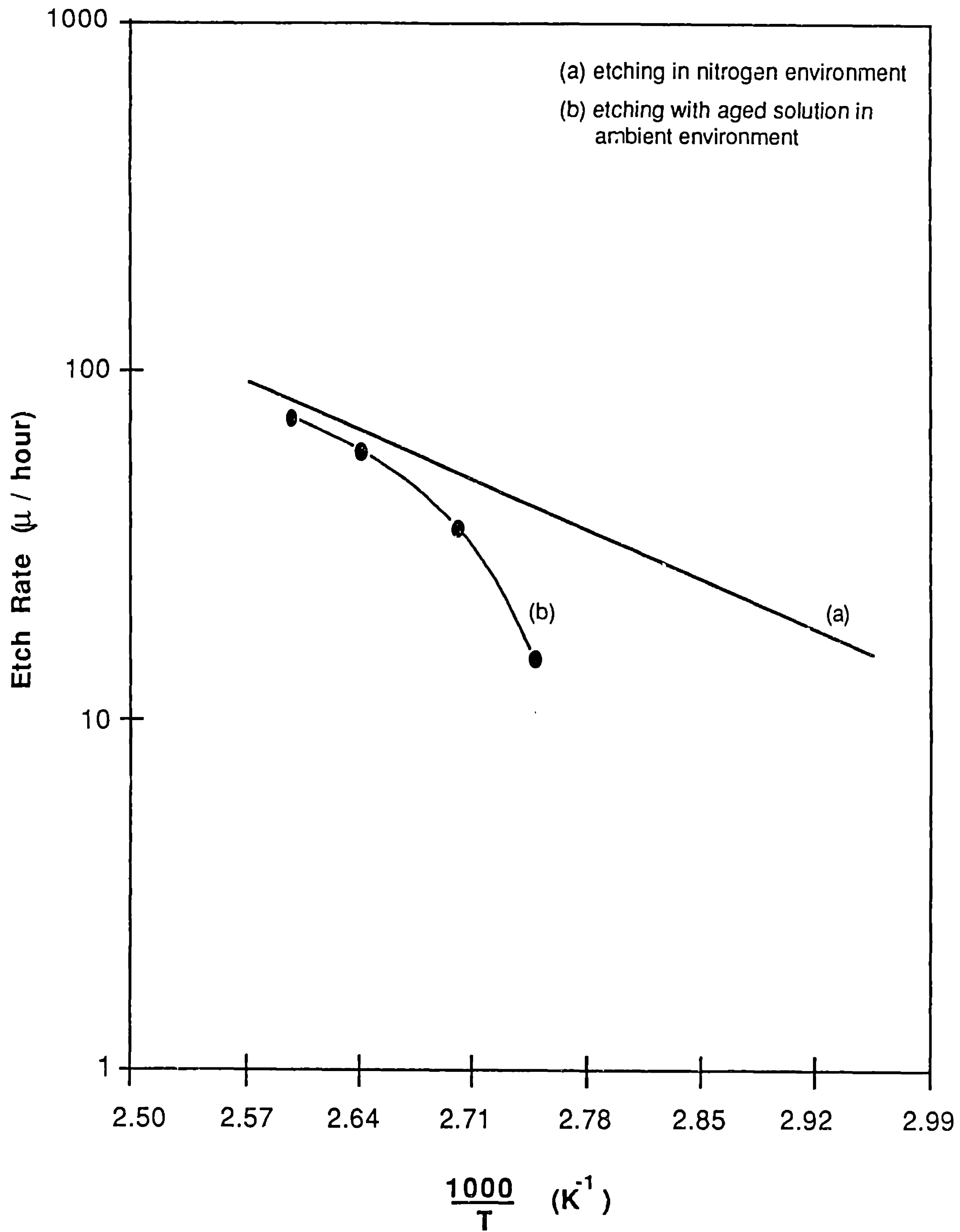


Figure 4: Effect of Hydrazine aging on (110) silicon etch rate

opened container is used (data point at 111.5°C), the etch rate is still lower than when etching is carried out in a nitrogen environment.

Since opening a new gallon of solution for every experiment is not cost effective and requires storage of large volumes of Hydrazine, the following approach was taken, to avoid the aging problem. The content of a gallon of solution was partioned to 500 ml volumes in separate 550 ml containers immediately after breaking the seal on the gallon. The separate containers were sealed immediately. For each experiment, one of the 550 ml containers was opened and used. This eliminated the reproducibility problem and the non-linear relation between the log of etch rate and reciprocal temperature. However, the etch rates are still 10% lower than Lee [66] found for a 50-50 hydrazine-water solution. Even though it is not specified, he may have mixed fresh solution for each of the experiments. This would be like using a solution from a freshly opened gallon in our case. To confirm this, an experiment was done at 85°C in nitrogen ambient using solution from a freshly opened gallon. The etch rates for all the samples at this temperature were consistently higher than the etch rates coded in figure 3. Hydrazine etching ability degrades in the presence of oxidizing ambient. Even for a solution taken from a freshly opened container, the etch rate is lower when etching is done in ambient as compared to a nitrogen environment, as mentioned previously.

In summary, reliable etch rate characteristics can be obtained by using Hydrazine in a glass reflux system continuously flushed with nitrogen. The etch rates are much higher than the results obtained for EDP (for (100) moderately doped silicon, Hydrazine etches 100% faster at 115°C than an EDP solution of the composition cited earlier). The (100)/(111) and (110)/(111) etch rate ratios are significantly poorer than those possible by KOH and EDP. However, this is not a limitation in most applications, especially when features have large dimensions.

## 2.6 Appropriate Masks for Hydrazine

One of the primary advantages of hydrazine-water solutions is that they do not attack most metal films. In addition, silicon dioxide and silicon nitride are etched very slowly, providing excellent masking ability. The etch rate of $SiO_2$ (thermally grown at 990°C and 95°C steam) was measured at close to 100 angstroms/hr at 118°C. Silicon nitride etch rate is lower but could not be measured accurately. 1000 angstroms of Ag, Au, Ti, and Ta were sputtered on glass slides and etched for four hours in Hydrazine at 118°C. No attack on the metal surfaces was observed. Surprisingly, filament evaporated Al on a glass slide was etched under the above conditions, but the etch rate was not measurable. Copper and zinc are not compatible with Hydrazine [68]. Polymer films such as resist and polyimide are destroyed quickly in Hydrazine.

Since highly boron doped silicon is not etched in Hydrazine, the boron concentration needed to effectively stop etching was investigated. The samples used in section 2.1 for studying the boron diffusion profile were used for this experiment. These samples were already lapped with known angles, $\theta$, (figure 5.A) for spreading sheet resistance studies. The lapped samples were etched in Hydrazine at 118°C for 30 minutes. This produced a step (figure 5.B) and the dimension, d, could be easily measured. Knowing $\theta$ and d , the boron layer thickness, t, that was not etched, could be calculated. Since the profile was already measured on the sample, the boron concentration at that depth was determined. Table I shows $\theta$, d, and t for the six samples. The boron concentration corresponding to these depths is close to $1.5x10^{20}$ $cm^{-3}$ for all the samples. Etching of the boron doped layer beyond this concentration is extremely slow and for practical purposes can be assumed to be zero.

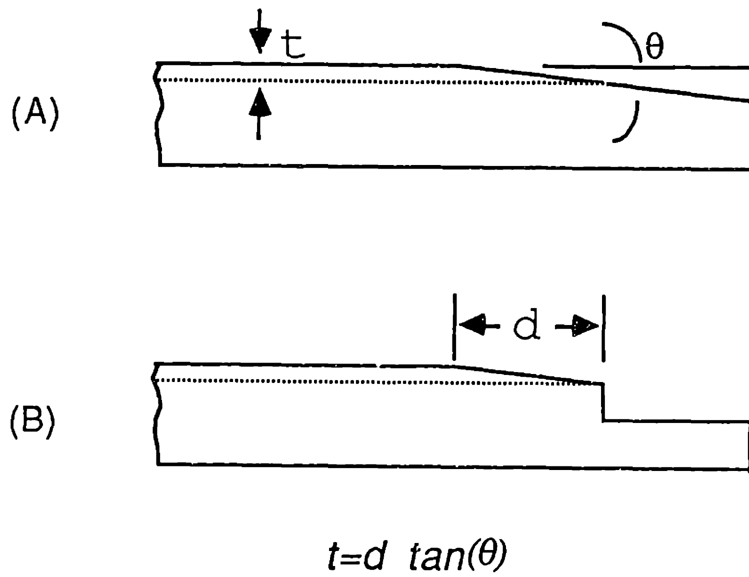


$t = d \tan(\theta)$

Figure 5: Angle lap technique for measuring the etch-stop layer thickness

| deposition time (min) | $\tan\theta$ | d (μ) | t (μ) |
|---|---|---|---|
| 30 | 0.0117 | 152 | 1.8 |
| 45 | 0.0217 | 108 | 2.34 |
| 60 | 0.0213 | 159 | 3.4 |
| 90 | 0.0192 | 174 | 3.4 |
| 120 ramping | 0.0493 | 95.5 | 4.7 |

Table I: Angle lap data for several samples

# 3 Silicon Micromachining

The anisotropic etchants KOH and EDP have been used to fabricated a variety of micro-mechanical structures in crystalline silicon. The results have demonstrated the etching quality that can be achieved using these etching systems. References of the previous chapter contain many of the work performed in this area, such as fabrication of diaphragms, beams, grooves, ink jet nozzles, and microtools. Additional references that discuss fabrication of micro-mechanical structures such as: silicon diaphragms [72]–[78], silicon diaphragms with center proof mass structure [79], polysilicon diaphragms [80], $SiO_2$ diaphragms [81], silicon and/or $SiO_2$ cantilever beams [82]–[85], thin silicon torsional elements [86], thin silicon hemispherical shells [87], isolation pits [88], grids [89], narrow vertical-walled shafts [90], V-grooves [91], and micro-probes [92,93] are available.

In this chapter, some basic structures and a few more complicated structures are presented which were anisotropically etched in (100) oriented silicon using Hydrazine with the procedure outlined in the previous section. Boron doped silicon diaphragms are fabricated by etching the substrate from the back and stopping at the thin boron doped silicon layer at the surface. Boron doped silicon cantilever beams, bridges, torsional mirrors, and suspended plates are fabricated by under etching from the surface. Thin boron doped crystalline silicon fibers are fabricated by selectively doping the surface of the substrate and then etching from the backside to create the fibers. These methods are then extended to fabricate suspended polyimide diaphragms and structures.

These structures demonstrate the excellent etching characteristics of Hydrazine. Side-walls constituted by the (111) planes are smooth, and corners are sharply defined. The etch stop surfaces, which are highly doped with boron, are very smooth and are highly reflective. Even though, the etch rate in (111) direction at 118°C is only one order of magnitude less than that of (100) direction, for large features, this does not constitute a problem. All the structures in this chapter are fabricated on 10-20 Ω-cm, 2 inch diameter, phosphorus doped, (100) silicon.

## 3.1 Boron Doped Silicon Diaphragms

Thin silicon diaphragms can be fabricated by doping the front surface of the sample with boron to a desired depth, opening a properly aligned window on the backside, and etching the substrate from the back in the exposed area until the etch stop boron doped layer is reached. This process is used here to fabricate 3-5 $\mu$ thick diaphragms in (100) silicon using Hydrazine at 118°C.

Solid source deposition at 1175°C (section 2.1) was used for creating the etch stop layer. Since the doping profiles resulting from such depositions had already been studied and the concentration of boron needed to stop etching was known, the deposition time could be adjusted to produce final diaphragms of desired thickness. To avoid significant altering of the doping profile after deposition, the native oxides were grown at 990°C. Oxide thicknesses were 3200 Å, resulting from 15 minutes dry $O_2$, 45 minutes steam at 95°C, and 15 minutes dry $O_2$.

Figure 6 outlines the fabrication process. The wafers are given a standard RCA clean and loaded into the boron deposition furnace at 900°C. The temperature ramping procedure is used (section 2.1) and deposition is done at 1175°C for the length of time necessary to produce desired thickness diaphragms (i.e. 2 hours would result in a 4.7 $\mu$ thick diaphragm) (figure 6.A). Under the furnace conditions outlined in section 2.1, the backside doping is very small, such that, the borosilicate glass can be stripped in HF after deposition and with adequate rinsing, the samples can be loaded in the oxidation furnace. If the backside deposition is significant, Hydrazine etching might be stopped on the backside and not proceed through the substrate. In this case, the highly doped layer on the back of the wafer must be removed either in plasma (i.e. $SF_6$) or a wet chemical isotropic etch (i.e. a hydrofluoric-nitric-acetic acid solution).

After the 3200 Å thermal oxide is grown, desired square windows are opened in the back oxide while leaving the front oxide intact (figure 6.B). Patterning is done by standard negative photoresist lithography, aligning the sides of the square windows to the (110) directed commercial flat of the wafer. The commercial flat on the (100) wafers (accurate within 1-2 degrees) is found to be sufficiently accurate for all the processes used in this work. The samples were given a 20 seconds 20:1 HF dip and adequate DI water rinse prior to Hydrazine etching. The Hydrazine etching process was carried out at 118°C until the diaphragms were etched out (figure 6.C). This

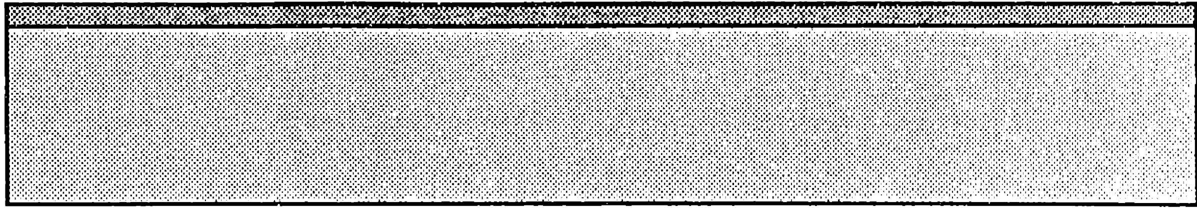

(A) Cross-section

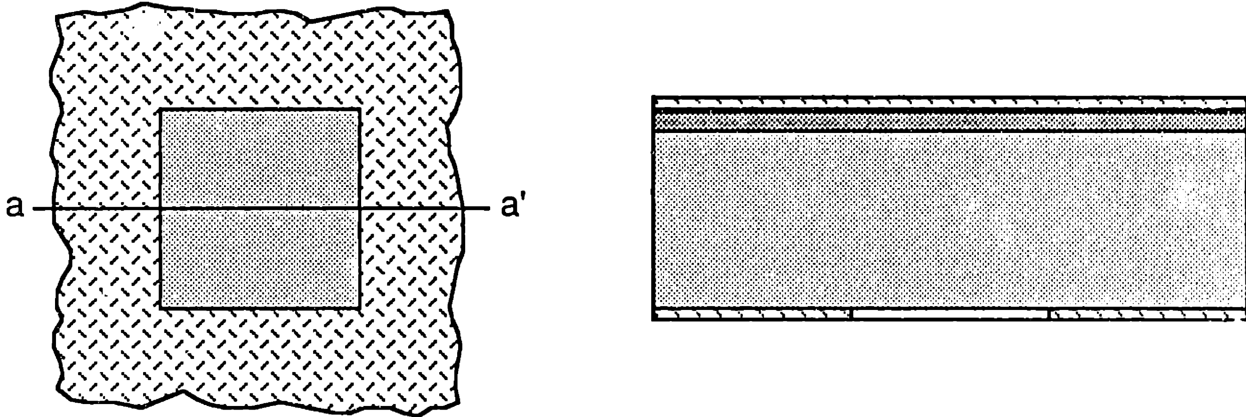


(B) Left: back view; Right: cross-section

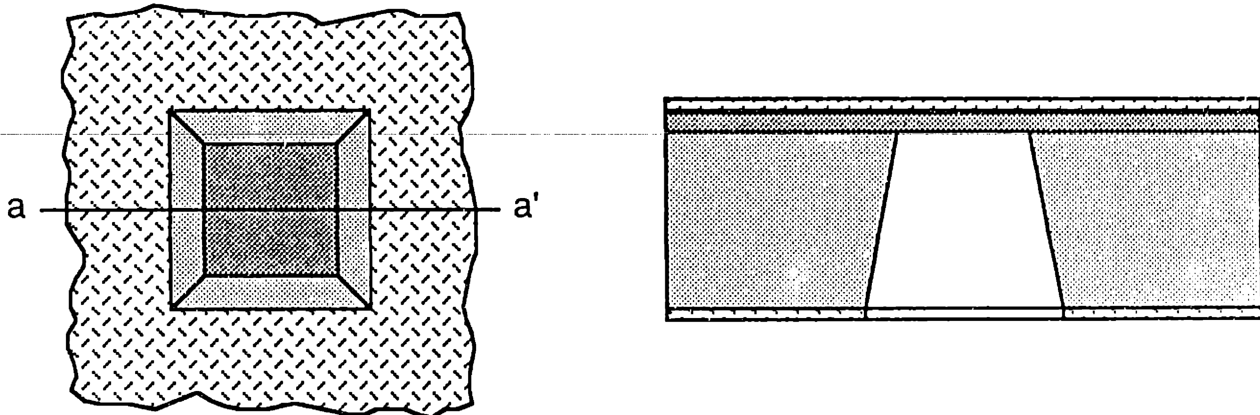


(C) Left: back view; Right: cross-section

Figure 6: Thin silicon diaphragm fabrication steps

could be easily monitored since Hydrazine is a clear solution and the surface of the boron doped layers is smooth and shiny. Appendix C outlines detailed processing steps.

The oxide on the front is not necessary since the boron doping on this side will automatically mask etching. This oxide was left intact for later applications in our work. It is important to have a good oxide, free of scratches, on the backside since any exposed region of the silicon substrate on the back is etched.

Using the above process, 3-5 $\mu$ thick diaphragms ranging in size from 100x100 $\mu$ to 1x1 inch was fabricated with perfect yield. Handling of diaphragms through standard VLSI process, even though delicate, is not difficult. Without the oxide on the front, silicon diaphragms up to 3x3 mm in size are perfectly flat in this thickness range but the larger diaphragms are buckled. Because of the large concentration of the boron in the diaphragm (above $1.5 \times 10^{20}$ $cm^{-3}$), most of the boron enters the lattice interstitially [60] which may create compressive stresses in the boron doped diaphragm. One of the 1x1 inch silicon diaphragms, 4.7 $\mu$ thick, was annealed in nitrogen at 1100°C for 4 hours in an attempt to leach out the boron, but the diaphragm did not flatten out.

Figure 7 is a SEM photograph of a 1x1 mm silicon diaphragm, 4.7 $\mu$ thick, with 2800 Å $SiO_2$. Figure 8 is a magnified view of the caption. The side walls are extremely smooth (almost featureless, making focusing very difficult at high magnifications). The bottom surface which is the boron doped etch stop layer is also very smooth. The resulting sharply defined 90 degree corners are well demonstrated in these figures and in figures 9 and 10, which are taken at an angle for better perspective. The white ring seen on the circumference of the structure is the under etch of the oxide due to etching of (111) planes and is evident in figures 8 and 10. Figure 11 shows the same view as figure 10 but now the oxide is removed.

Figure 12 is an optical photograph of a 1x1 mm 2800 Å thick oxide diaphragm. It was fabricated using essentially the same process that has been described, excluding the creation of a boron etch stop layer. The buckling of the oxide due to residual compressive stress is evident. These oxide membranes are extremely delicate such that they crack or break easily.

While etching in the (100) direction, Hydrazine does not produce smooth surfaces until the etch-stop layer is reached. This means that timed etching cannot be used to etch thick diaphragms with a smooth bottom surface. However, smooth

(100) surfaces are reported when using a hydrazine-water solution of 80% hydrazine and 20% water composition [67,73].

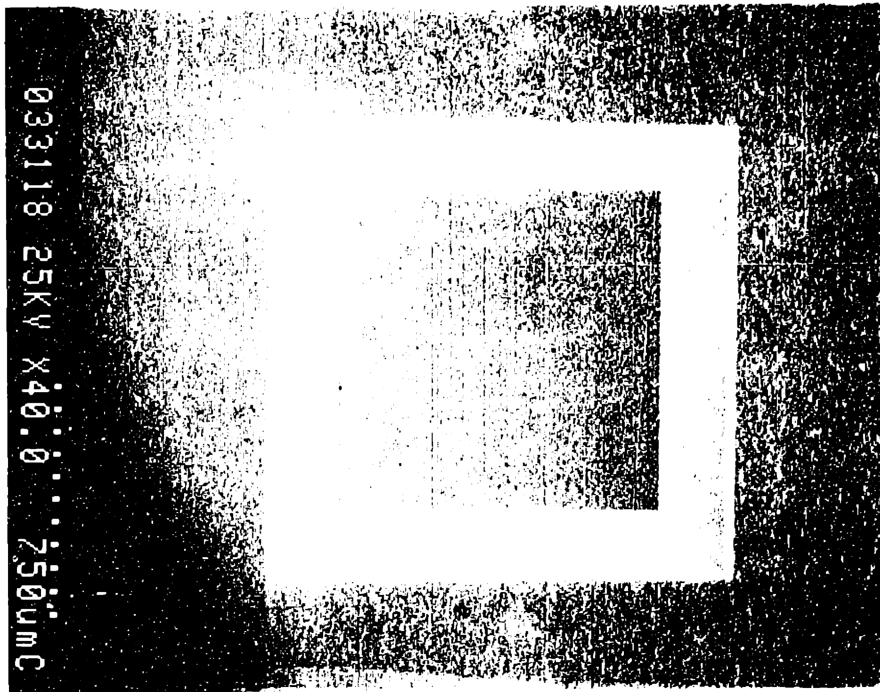


Figure 7: SEM of a 4.7 $\mu$ thick, 1x1 mm, silicon diaphragm from the back

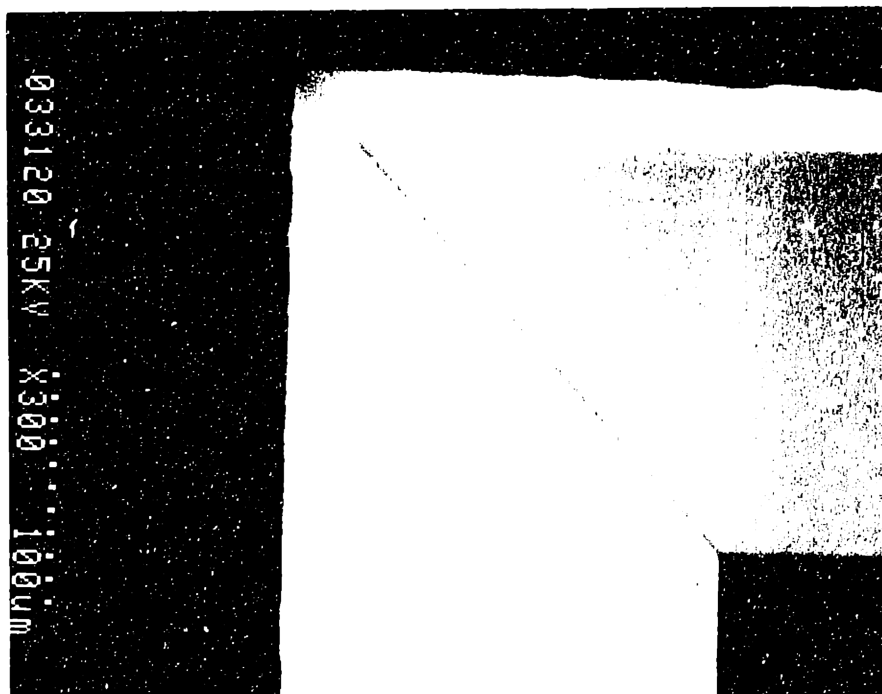


Figure 8: Magnified corner of figure 7

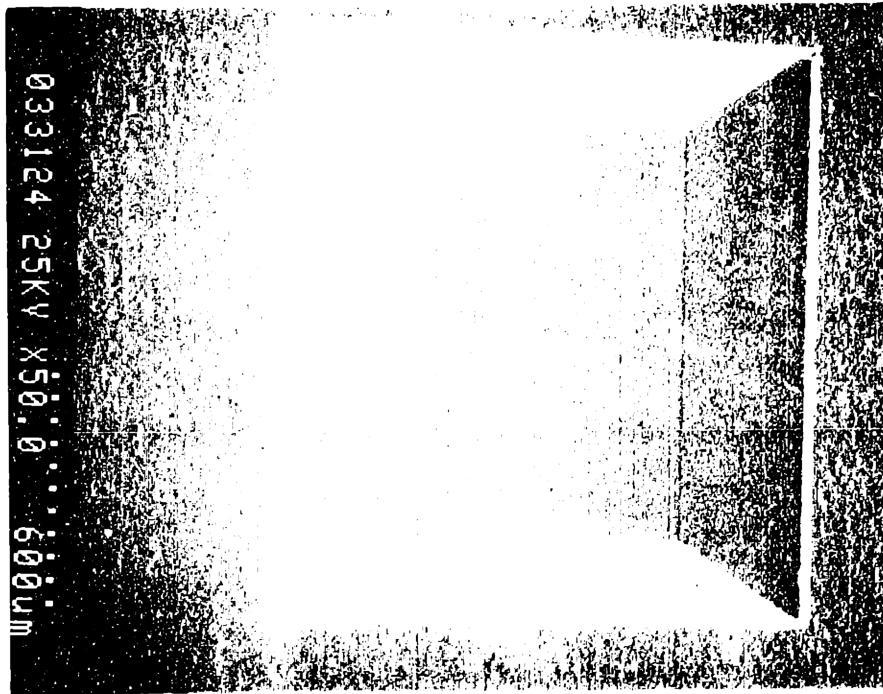


Figure 9: SEM of the same silicon diaphragm as in figure 7 at an angle

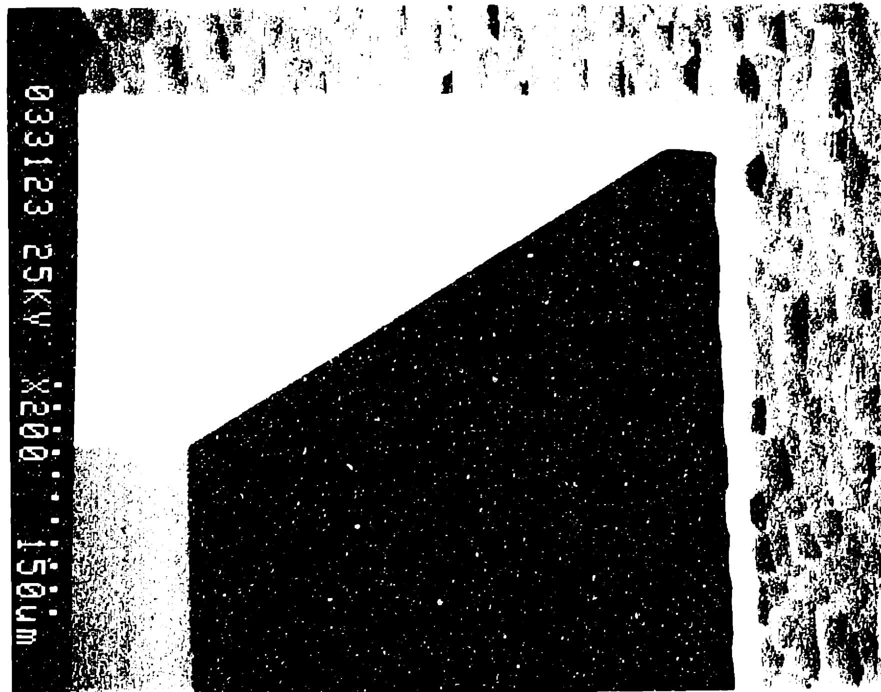


Figure 10: SEM of figure 8 at an angle

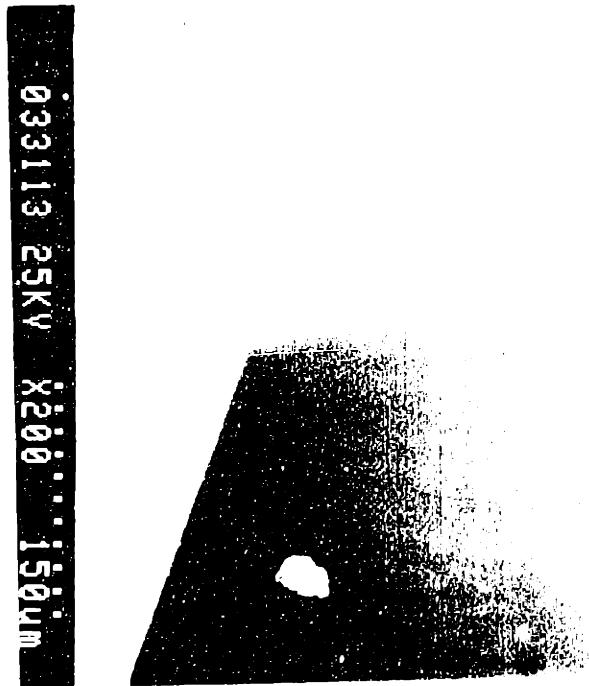


Figure 11: SEM of [illegible] same silicon diaphragm [illegible]
removed.

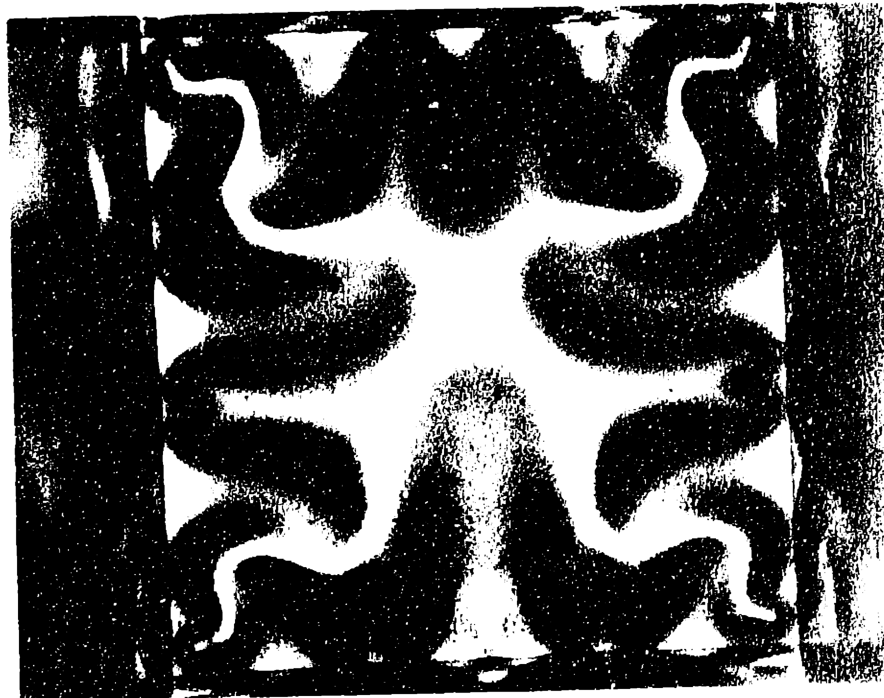

Figure 12: Photograph of a 2800 Å, 1x1 mm, oxide diaphragm [illegible] back

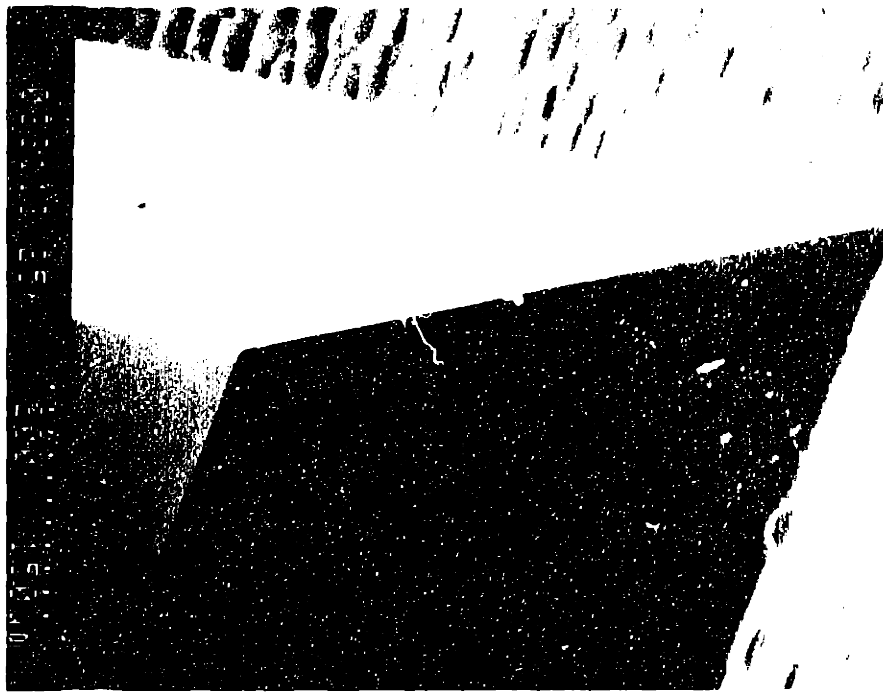

Figure 11: SEM of the same silicon diaphragm as in figure 10 with back oxide removed

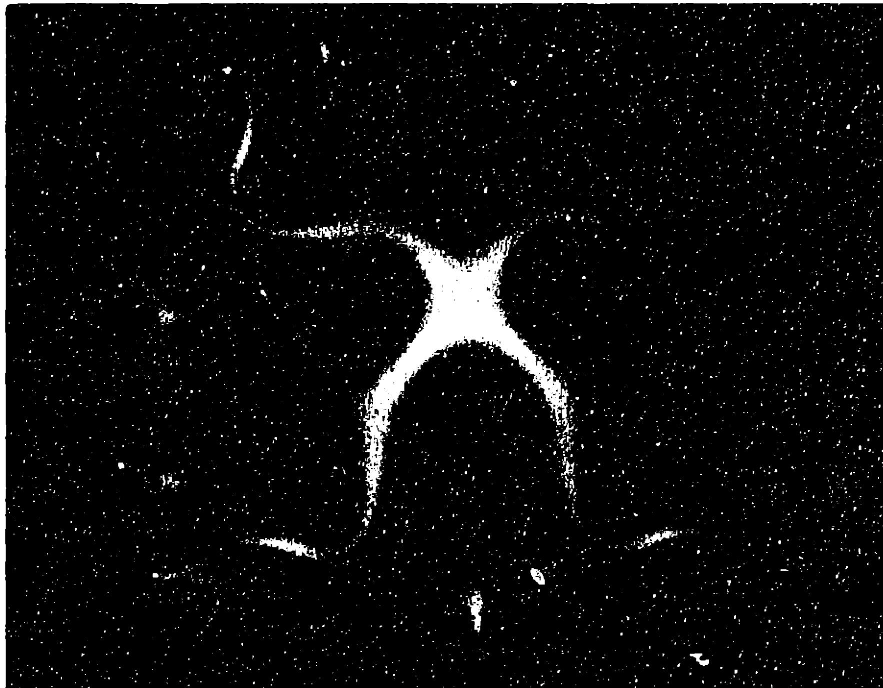

Figure 12: Photograph of a 2800 Å, 1x1 mm, oxide diaphragm from the back



INTENTIONAL DUPLICATE EXPOSURE

## 3.2 Silicon Diaphragm Pressure Transducer

Thin silicon diaphragms have long been used for accurate pressure measurements [72]–[75]. The response of a 1x1 mm silicon diaphragm, 4.7 $\mu$ thick, fabricated as outlined in the previous section, was measured under static pressure by Prof. J. Haritonidis and David Warkentin from the Aeronautics and Astronautics Department at M.I.T. A new readout technique was tried in which the deflection of the diaphragm under pressure was measured interferometrically as shown in figure 13. A 700 Å thick Al film was evaporated on the back surface of the diaphragm for better reflectivity.

The reflected laser rays from the back of the diaphragm and the beam splitter are interfered. The interference fringes are detected by a simple photodiode circuitry. Figure 14 shows the output voltage versus the deflection in the center of the diaphragm. The output voltage changes by approximately 3 volts when the static pressure is changed by 1 mmHg. Excellent sensitivity can be achieved by operating at the steep portion of the curve. Deflections of a few nanometers are easily measured.

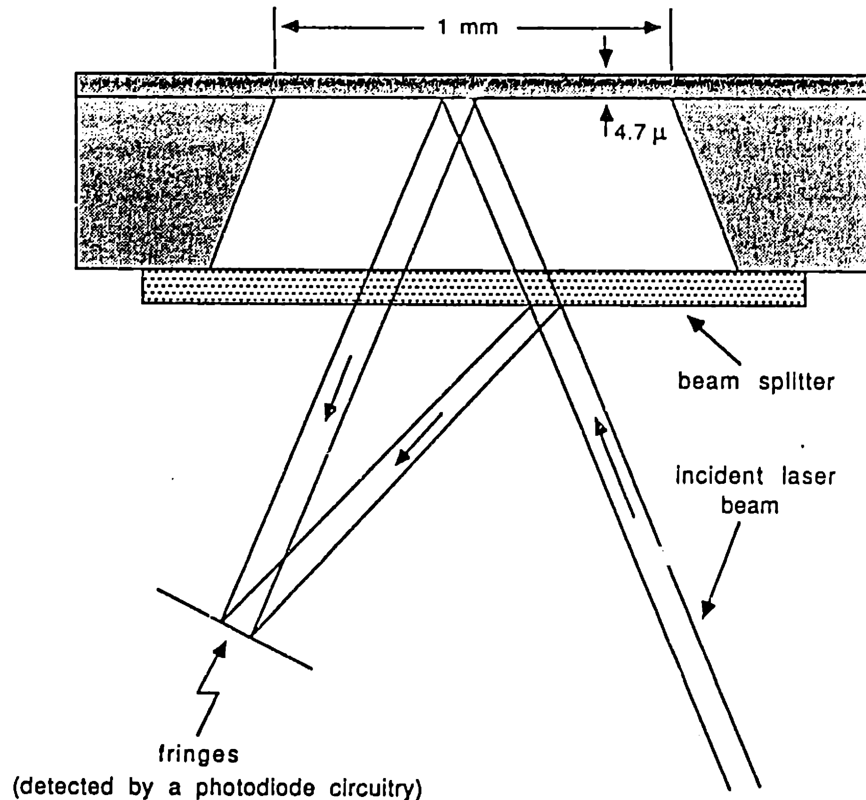


Figure 13: Pressure measurement set-up for the silicon pressure transducer

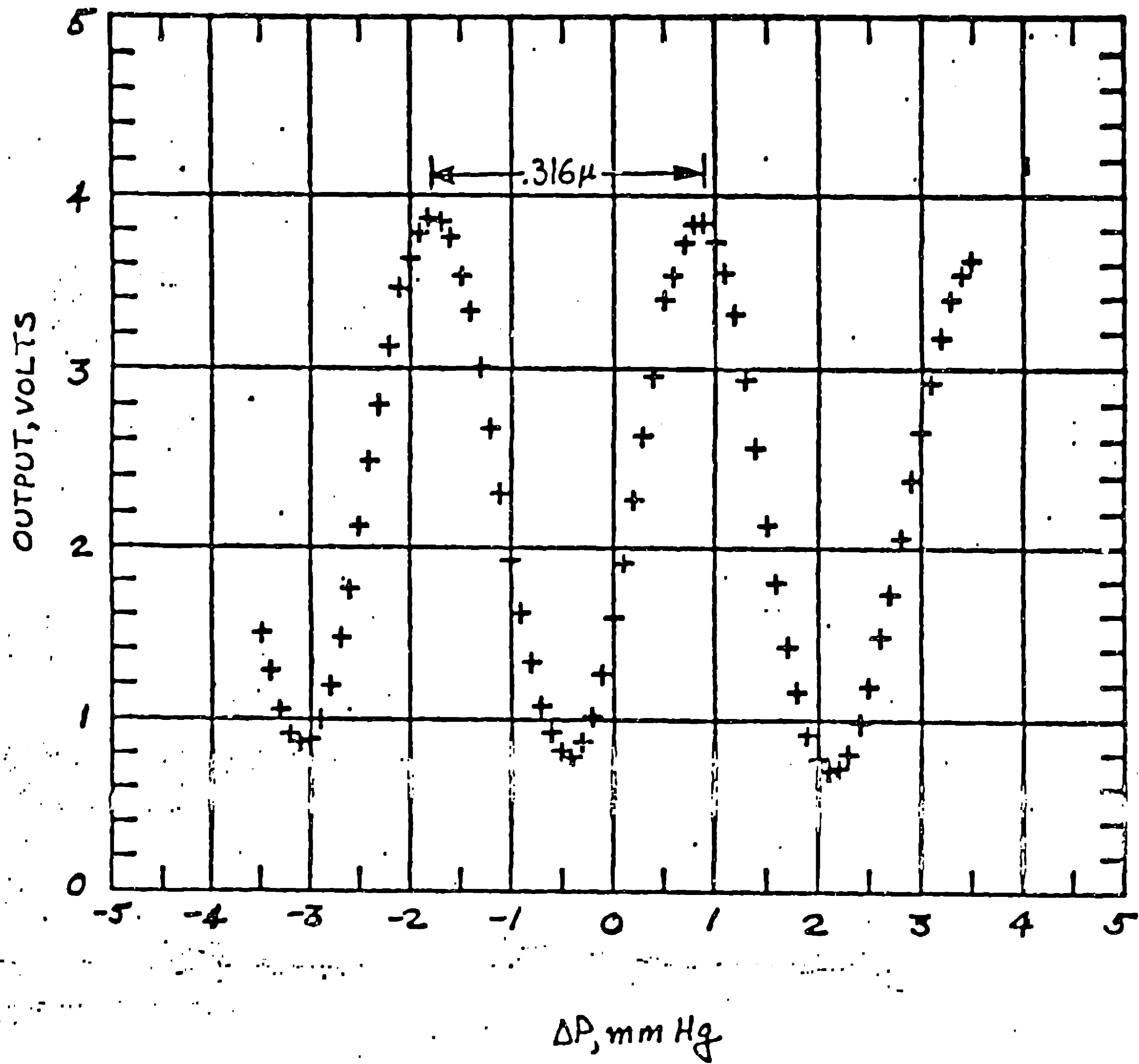


Figure 14: Static pressure response of the silicon diaphragm pressure transducer

## 3.3 Under Etching by Hydrazine

Mechanical microstructure can be fabricated in silicon by taking advantage of the fact that convex corners are etched by the anisotropic etchants. This is due to faster etching of higher index planes. Etching of convex corners have been used to fabricate structures such as cantilever beams in EDP [82]–[84]. It is demonstrated that the (211) planes are the fastest etching planes in hydrazine-water solutions [66]. This means that Hydrazine can be used for effective etching of convex corners. Fabrication of silicon cantilever beams, bridges, torsional mirrors, and suspended plates using boron doped etch-stop regions under-etched from convex corners is presented here.

Figure 15 outlines the process for fabricating a silicon cantilever beam. Other structures on the same mask are processed identically. The wafer is given a standard RCA clean and a thermal oxide is grown at 1100°C thick enough to mask boron deposition (figure 15.A). A standard negative resist lithographic process is used to pattern the features on the front surface such that the substrate is exposed where the feature is to be fabricated (figure 15.B). Solid source boron deposition is done using the temperature ramping procedure (section 2.1) at 1175°C for appropriate length of time (i.e. 2 hours if 4.7 $\mu$ thick boron etch-stop layer is desired) (figure 15.C). At this point, the oxide on both sides of the wafer is removed, the sample is cleaned (standard RCA), and a new thermal oxide is grown at 990°C for a thickness of 3200 Å. The oxide on the front is patterned, using the original mask and positive resist lithographic process, to expose the areas of the sample that are not doped with boron, leaving the back oxide intact (figure 15.D). The samples are then etched in Hydrazine until the structures are etched free (figure 15.E). Appendix D outlines the detailed steps of the process.

The oxide on the front surface is not necessary but was used to protect this surface and to indicate the endpoint for etching since the compressive stress in the oxide causes the under-etched structures to deform. For the particular samples shown here, boron deposition is done for 3 hours, resulting in etch-stop thickness of 6 $\mu$. The Hydrazine etch is carried out at 115°C. The sides of the features are aligned to the (110) direction in one case and are misaligned by 5 and 10 degrees in two other cases. The slight misalignment increases the under-etching speed because the side planes which are off from the (111) direction are etched in addition to the

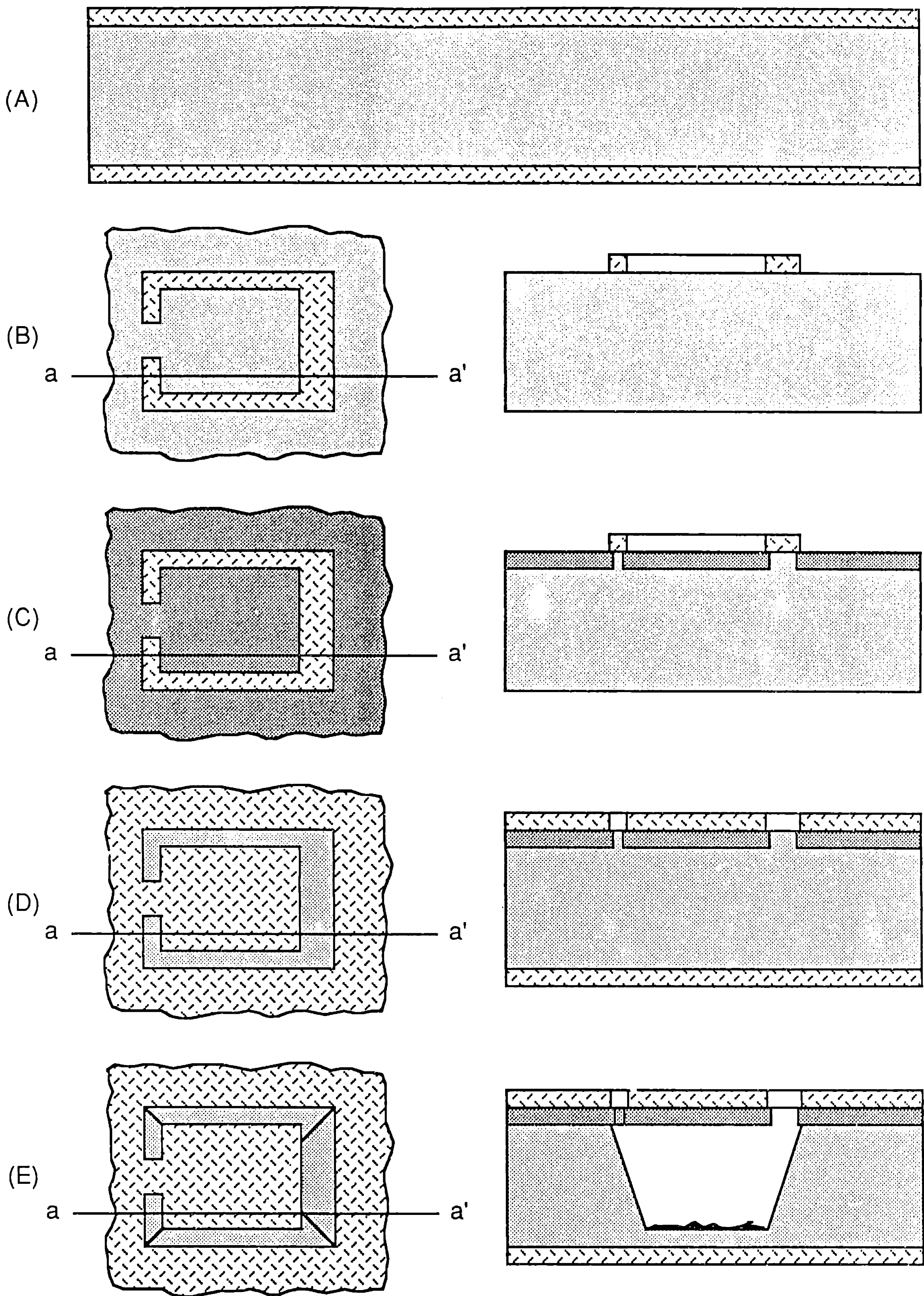


Figure 15: Fabrication of a silicon cantilever beam by under-etching

convex corners. It was found that after six hours of under-etching at 115°C, the 5 and 10 degrees misaligned features were etched free except for the suspended plates. Similar structure which were perfectly aligned are not etched completely but were close to completion.

Figure 16 is SEM photograph of a wide silicon cantilever beam with 2600 Å of thermal oxide. The sides of this structure are misaligned by 5 degrees from the (110) direction, which is evident in the photograph. The (111) side-walls are perfectly smooth. Figure 17 is a high magnification view of one corner of this beam. The rounding of this corner due to diffusion of boron is clearly shown. In addition, since the second oxide was patterned using the original mask and the boron diffused laterally under the original oxide mask (figure 15.C), the second oxide does not cover out to the edge of the beam. Overall, the etching quality is excellent.

Figure 18 is SEM photograph of a torsional mirror with the neck part in caption. The thin necks provide freedom of rotation for the plate around that axis. Figure 19 is the SEM picture of a bridge-like structure. Again, the rounding of the corners due to diffusion is observed. To show corner rounding due to the isotropic nature of diffusion, a plus-shaped feature area was masked during boron deposition which would be etched later. Figure 20 is the SEM picture of this feature after the process. The feature still holds its symmetry but all the corners are rounded. All of the above feature are misaligned by 5 degrees from the (110) direction.

Figure 21 is the SEM photograph of a silicon plate held by four necks. This structure was not etched free after six hours and needed longer time to be completed. This is attributed to the small size of the opening from which the solution has to penetrate and under-etch the structure.

The basic structures presented in this section show Hydrazine's ability for under-etching by attacking the convex corners. The surfaces and the (111) side-walls are extremely smooth. Under etching is reasonably fast at 115°C and can be sped up at temperatures close to boiling point of the solution (120°C). The overall etching characteristics of Hydrazine and its many advantages over KOH and EDP make Hydrazine a good choice for silicon anisotropic etching.

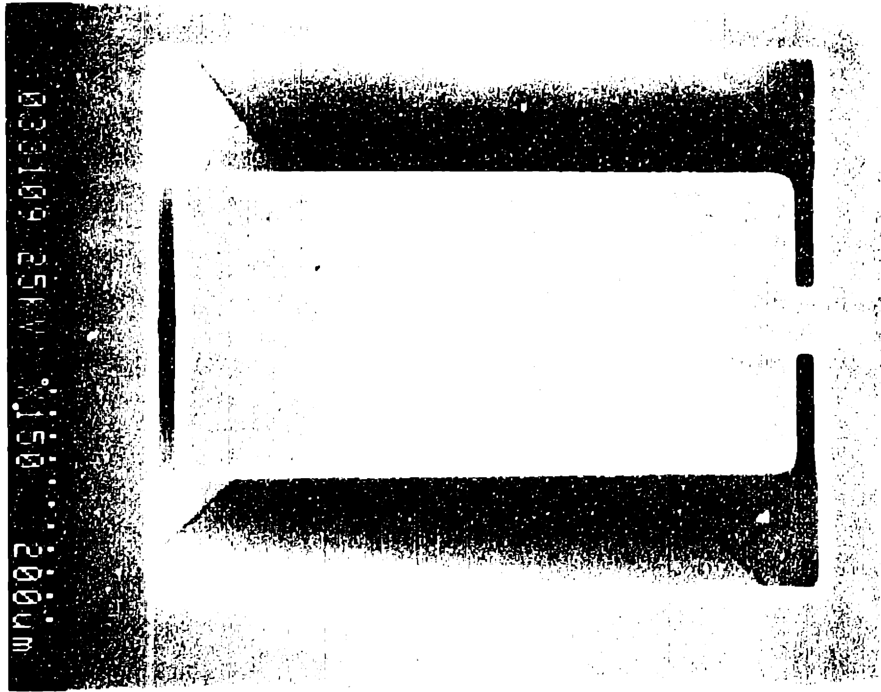


Figure 16: SEM photograph of a wide silicon cantilever beam

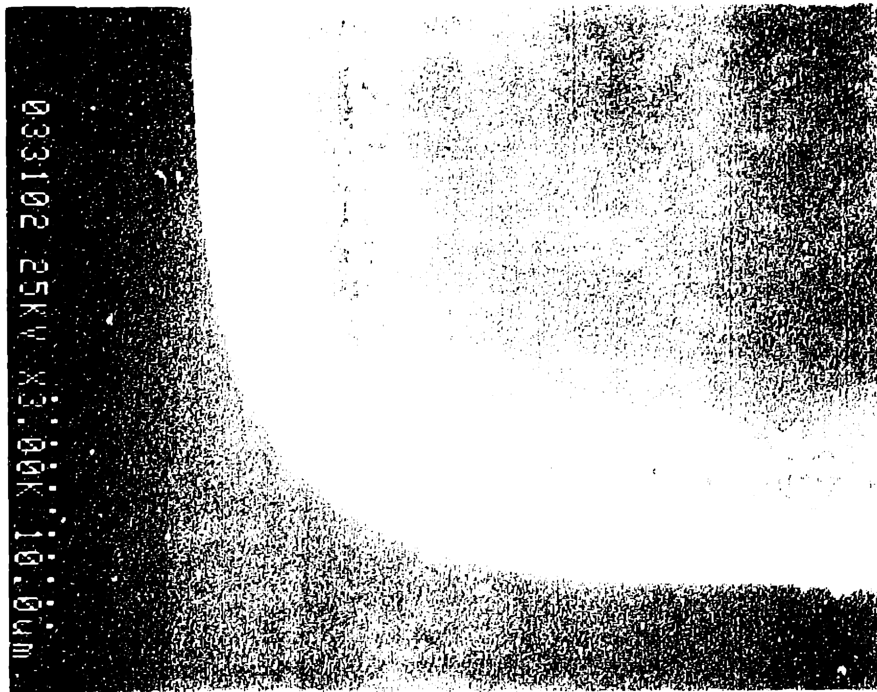


Figure 17: Magnified view of a beam corner in figure 16

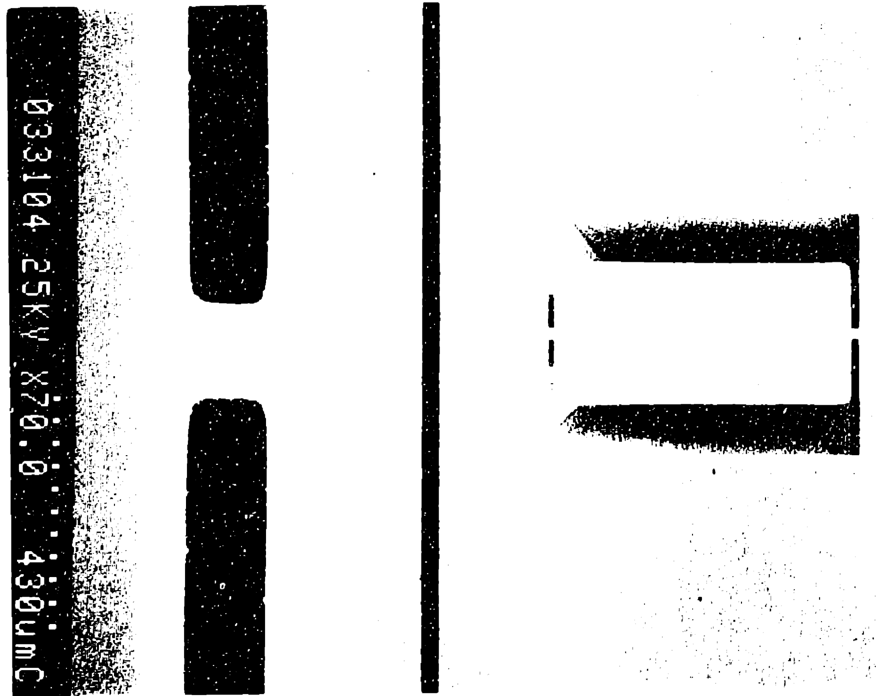


Figure 18: SEM photograph of a silicon torsional mirror

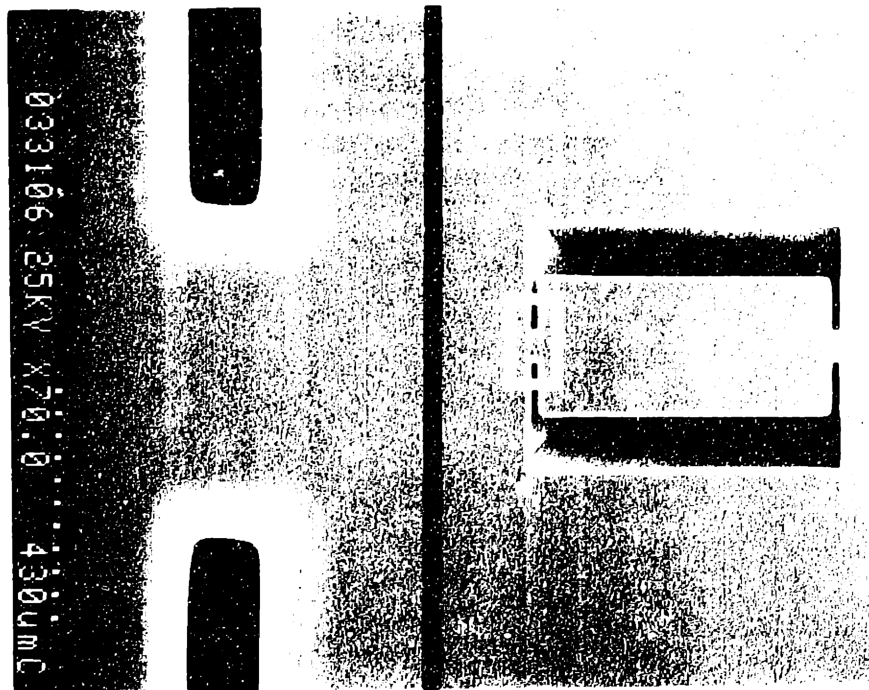


Figure 19: SEM photograph of a silicon bridge

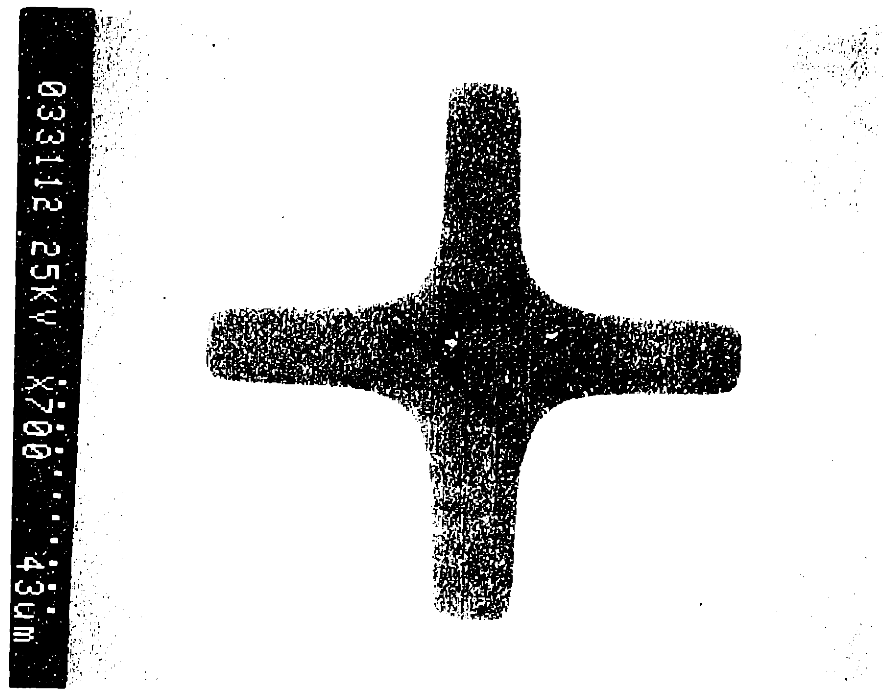


Figure 20: SEM of an etched + sign showing the corner rounding due to diffusion

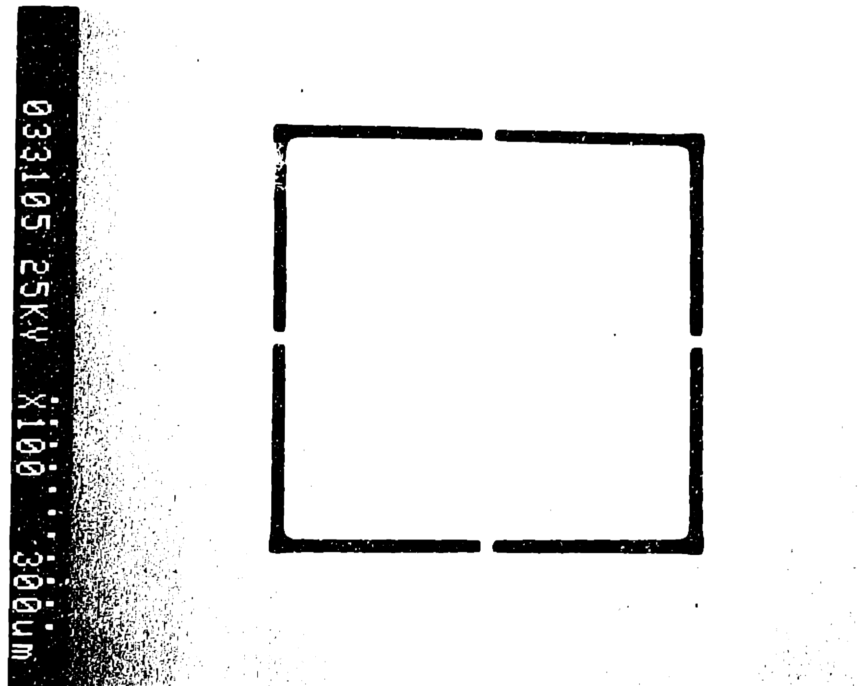


Figure 21: SEM photograph of a silicon plate held by four necks

## 3.4 Thin Silicon Fibers

With the advancing field of fiber composites, it is of interest to investigate the possibility of fabricating single crystal fibers from silicon. This can be done by employing the micromachining techniques that have been presented so far.

Figure 22 outlines the process steps. Silicon substrates are RCA cleaned and a thick native oxide is grown. This oxide is patterned with a basic grating pattern supported in a frame. The grating lines are 25 $\mu$ wide with 20 $\mu$ spacing, and three different lengths: 0.3, 0.5, and 0.7 inch. Using a negative resist process, 20 $\mu$ wide oxide lines remain which separate the 25 $\mu$ wide exposed areas. The mask pattern sides are aligned to the (110) direction (figure 22.A shows the mask pattern and alignment on the left and an enlarged portion of the grating on the right).

The temperature ramping procedure was used to deposit boron at 1175°C (figure 22.B). Due to isotropic nature of diffusion, the final width of the fibers is 35 $\mu$ with 10 $\mu$ spacing between the fibers. The oxide is removed and new oxide was grown at 990°C for a thickness of 3200 Å. At this point, the wafers were cleaved to the square shape of the pattern (giving a square sample of 1.4x1.4 inch). This provides the necessary alignment marks for front to back alignment. Three rectangular windows are opened in the back oxide exactly under the three grating windows using a negative resist lithographic process. The sizes of the back windows are slightly larger to take to account the reduction in size due to inclined (111) planes. As long as the backside features are aligned to the ones on the front, the sides of the opening windows on the back are aligned to the (110) direction (figure 22.C shows the backside of the cleaved sample on the left and an enlarged portion of one oxide window on the right). The front oxide is removed during this lithography step. The samples are then etched in Hydrazine at 118°C to leave the supporting frame with the fibers (the grating lines which are boron doped) (figure 22.D shows the top view of the completed sample on the left and an enlarged view of one anisotropically etched window on the right).

For the actual fibers presented here, boron deposition was done for 3 hours, resulting in a 6 $\mu$ thick etch-stop layer. The Hydrazine etch was carried out at 118°C. Appendix E outlines the detailed fabrication steps.

Figure 23 is SEM photograph of many fibers attached to the frame at one end. Figure 24 shows a closer view of three fibers connected to the support frame (for

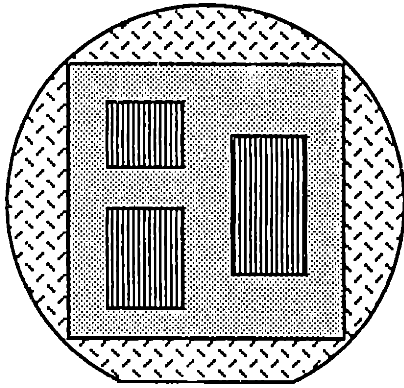
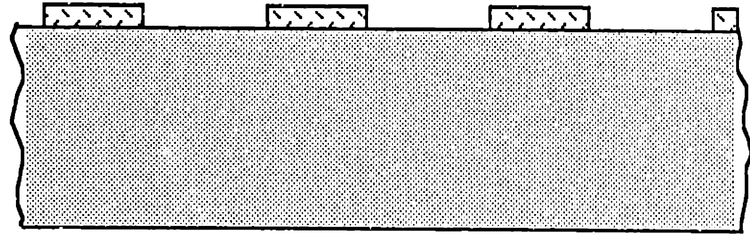

(A) Left: Pattern aligned to the flat of the 2 inch wafer; Right: enlarged cross-section of a grading region

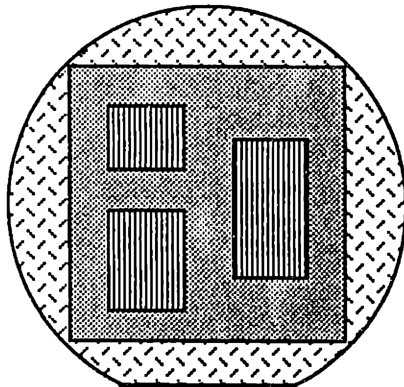
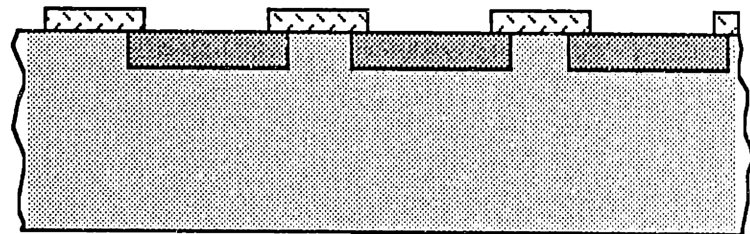

(B) Left: top view of the 2 inch wafer; Right: enlarged cross-section of a grading region

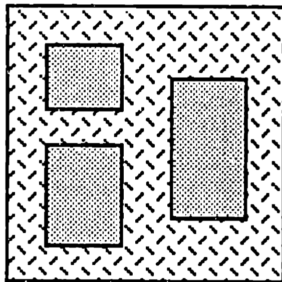
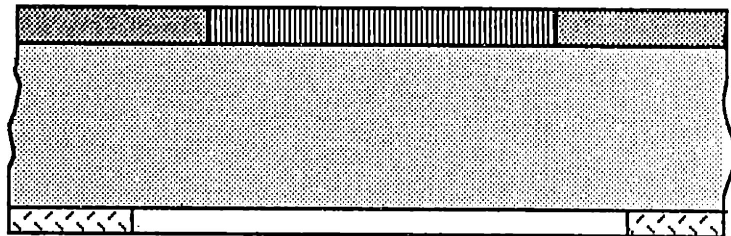

(C) Left: back view; Right: cross-section of one window

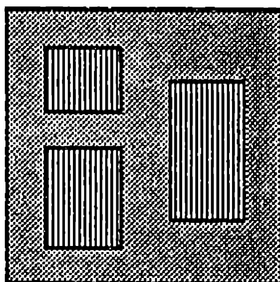

(D) Left: top view; Right: cross-section of an etched window

Figure 22: Fabrication steps for thin silicon fibers

better perspective, the SEM photograph is taken at a tilt angle). Figure 25 shows the flexibility of these thin single crystal silicon fibers. The top and bottom surfaces of these fibers are very smooth. The top is the polished surface of a silicon wafer while the bottom is the smooth surface of the etch-stop layer (the smoothness of this surface has been showed in the previous sections). Figure 26 shows a high magnification view of the side-walls which is also very smooth as expected.

These thin single crystal silicon fibers are extremely flexible. A 0.7 inch long fiber can be bent into a circle without breaking. Upon release, the fiber goes back to their original shape. The loop strength of these fibers was not tested.

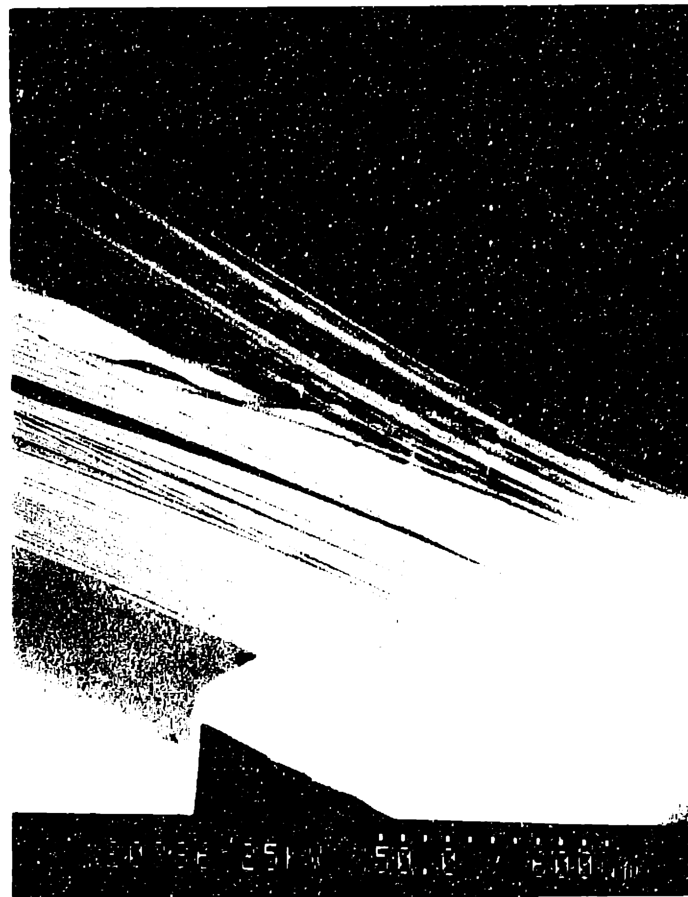

Figure 23: SEM picture of many fibers attached to the frame on one side

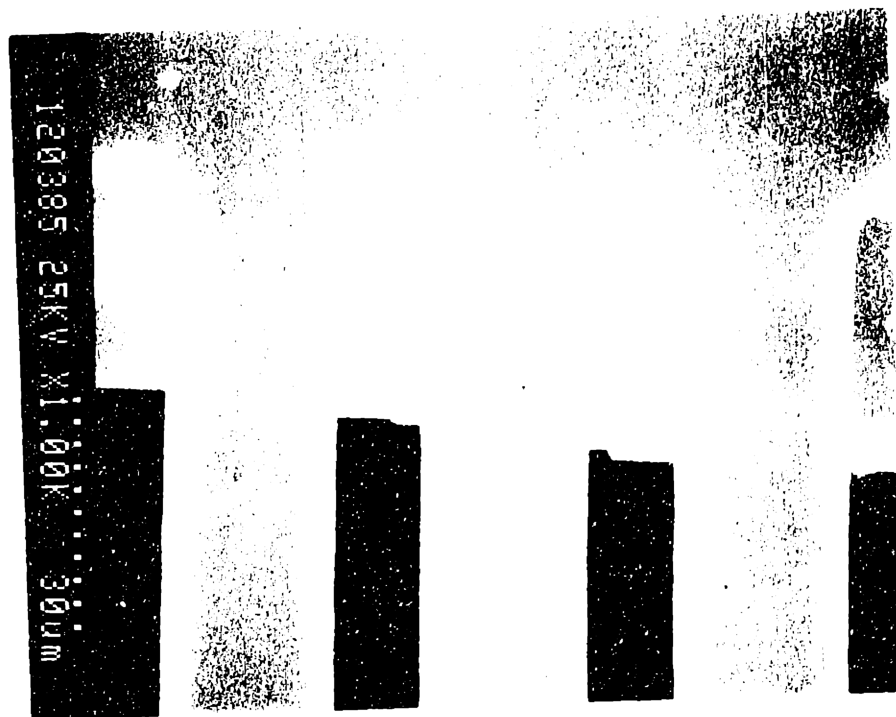


Figure 24: Top view of three fibers connected to the support frame

Figure 25: SEM picture showing the flexibility of the thin silicon fibers

Figure 24: Top view of three fibers connected to the support frame

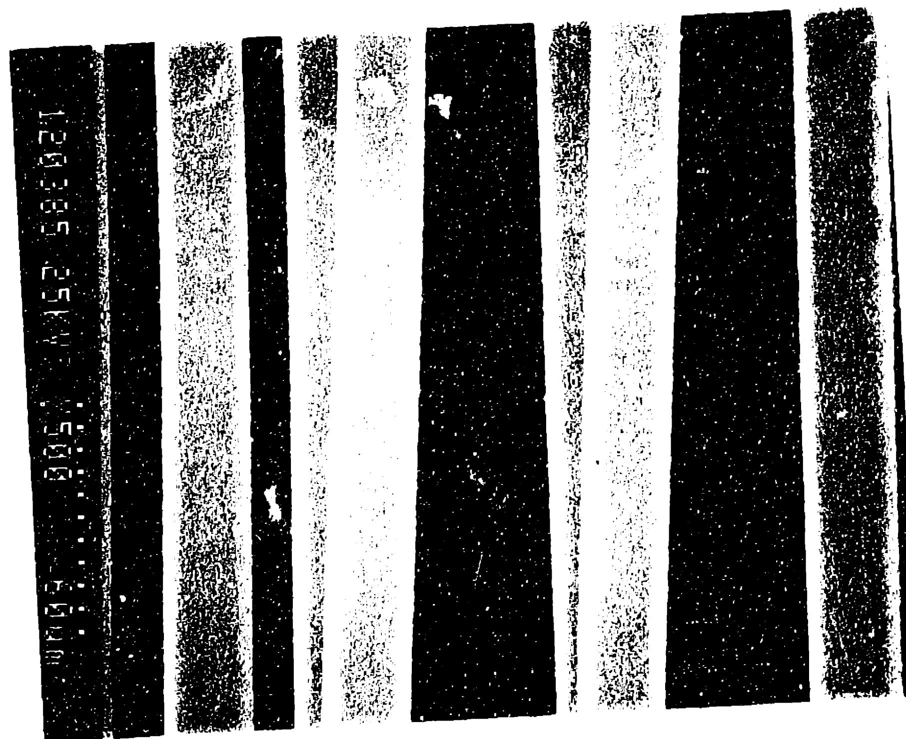

Figure 25: SEM picture showing the flexibility of the thin silicon fibers



INTENTIONAL DUPLICATE EXPOSURE

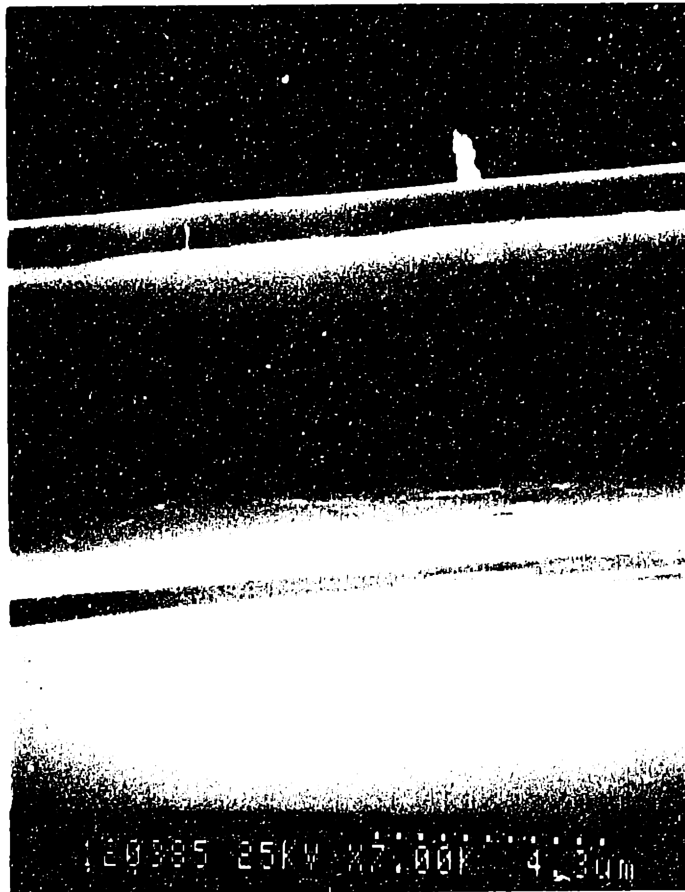


Figure 26: SEM picture of the side-wall of a thin silicon fiber

Figure 26: SEM picture of the side-wall of a thin silicon fiber



INTENTIONAL DUPLICATE EXPOSURE

## 3.5 Suspended Polyimide Membranes

Suspended membranes have been used for studying stress in thin films [94]. Such membranes have also been used in studying the adhesion of films to substrate [5]. A lithographic process is developed here for fabricating suspended polyimide films on a silicon dioxide/silicon substrate. These membranes are used in chapter 4 for studying stress in polyimide and adhesion of the film to substrate.

Figure 27 outlines the process steps. Initially, silicon membranes of the desired size and thickness (generally 4.7 $\mu$ thick) are fabricated as outlined in section 3.1 (figure 27.A). Polyimide is then spin-coated on the substrate in multiple layers (soft baked after each layer and cured at the end), resulting in the desired thickness (figure 27.B). The thin silicon layer is then removed in $SF_6$ plasma which also removes the oxide and leaves the polyimide diaphragm behind (figure 27.C). Appendix F outlines the detailed process steps.

A conventional vacuum spinning chuck cannot be used for spin-coating the silicon substrates incorporating the thin diaphragms. The vacuum can rupture the diaphragms. Even if the diaphragms survive, the coated film thickness is non-uniform due to diaphragm deformation under vacuum. To avoid this, a vacuum spinning chuck was designed that only applied vacuum to the periphery of the wafer. The chuck consists of two parts that were machined separately and were glued together at the end. Figure 28 and 29 show the design for the two parts. Using this vacuum spinning chuck, diaphragms as large as 1x1 inch and 4.7 $\mu$ thick could be spin-coated with no difficulties.

The outlined process is routinely used to fabricate polyimide diaphragms ranging in size from 100x100 $\mu$ to 1x1 inch with thicknesses between 5-10 $\mu$ with perfect yield. Note that the outlined process avoids the exposure of polyimide film to wet chemicals.

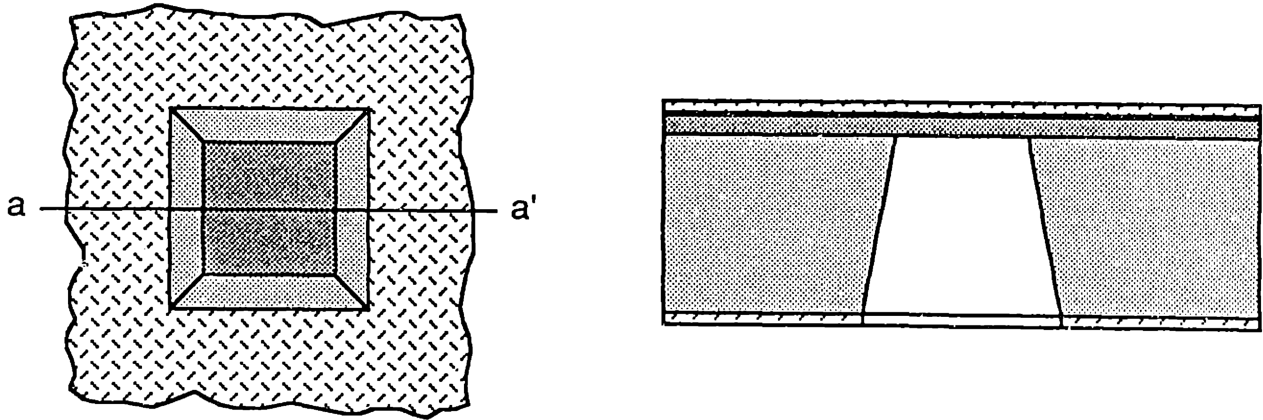


(A) Left: back view; Right: cross-section

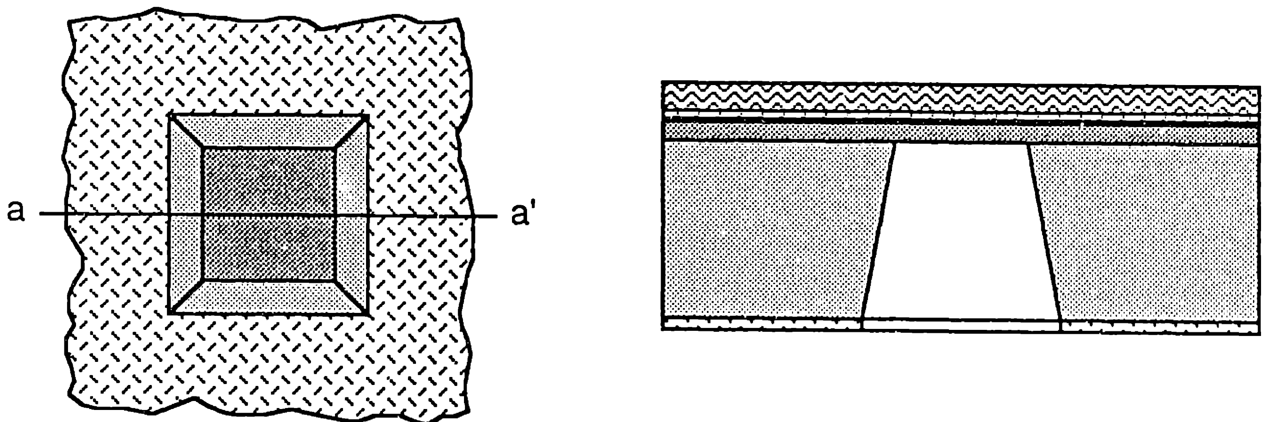


(B) Left: back view; Right: cross-section

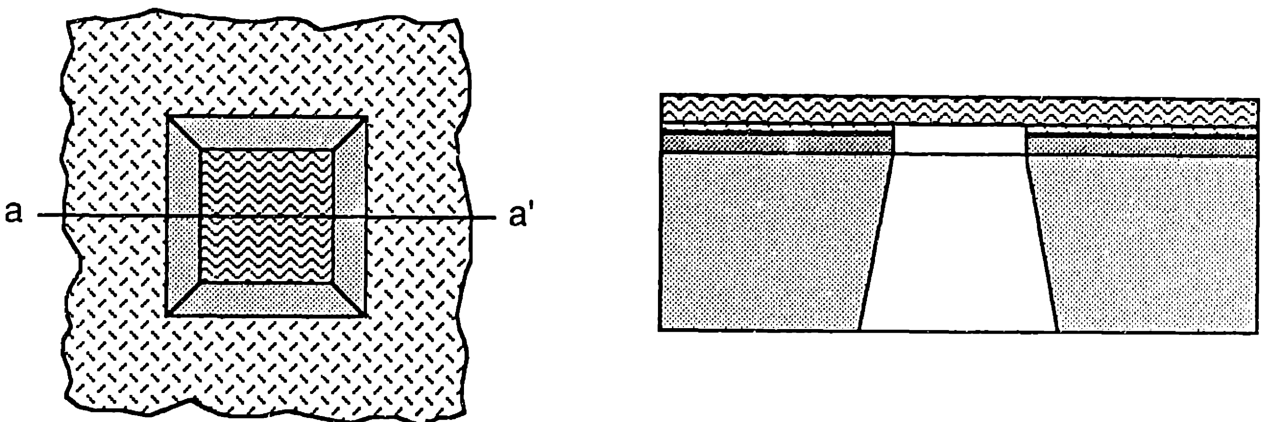


(C) Left: back view; Right: cross-section

Figure 27: Fabrication process for polyimide diaphragms

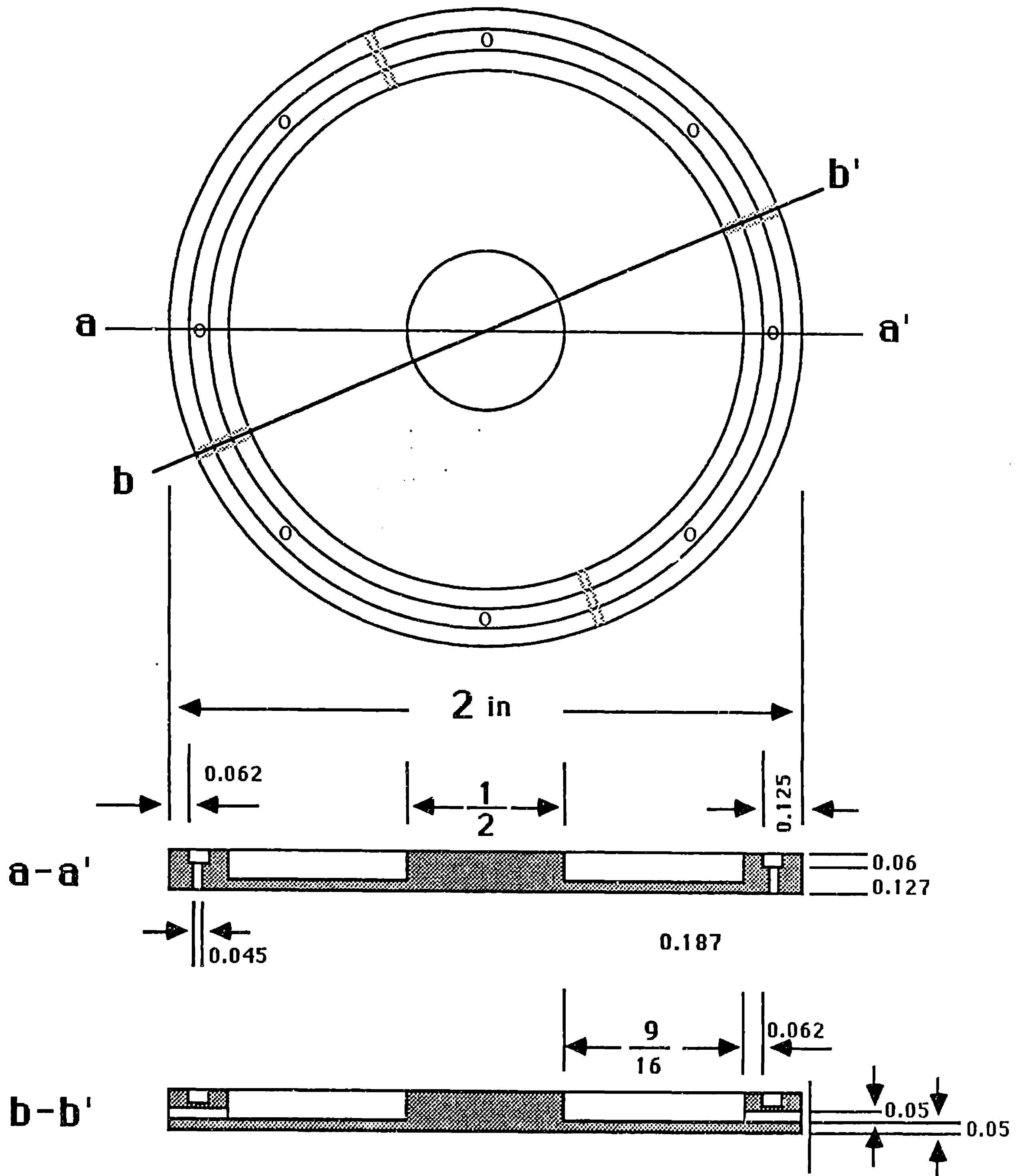


Figure 28: Top part of the vacuum spinning chuck
(all dimensions in inches)

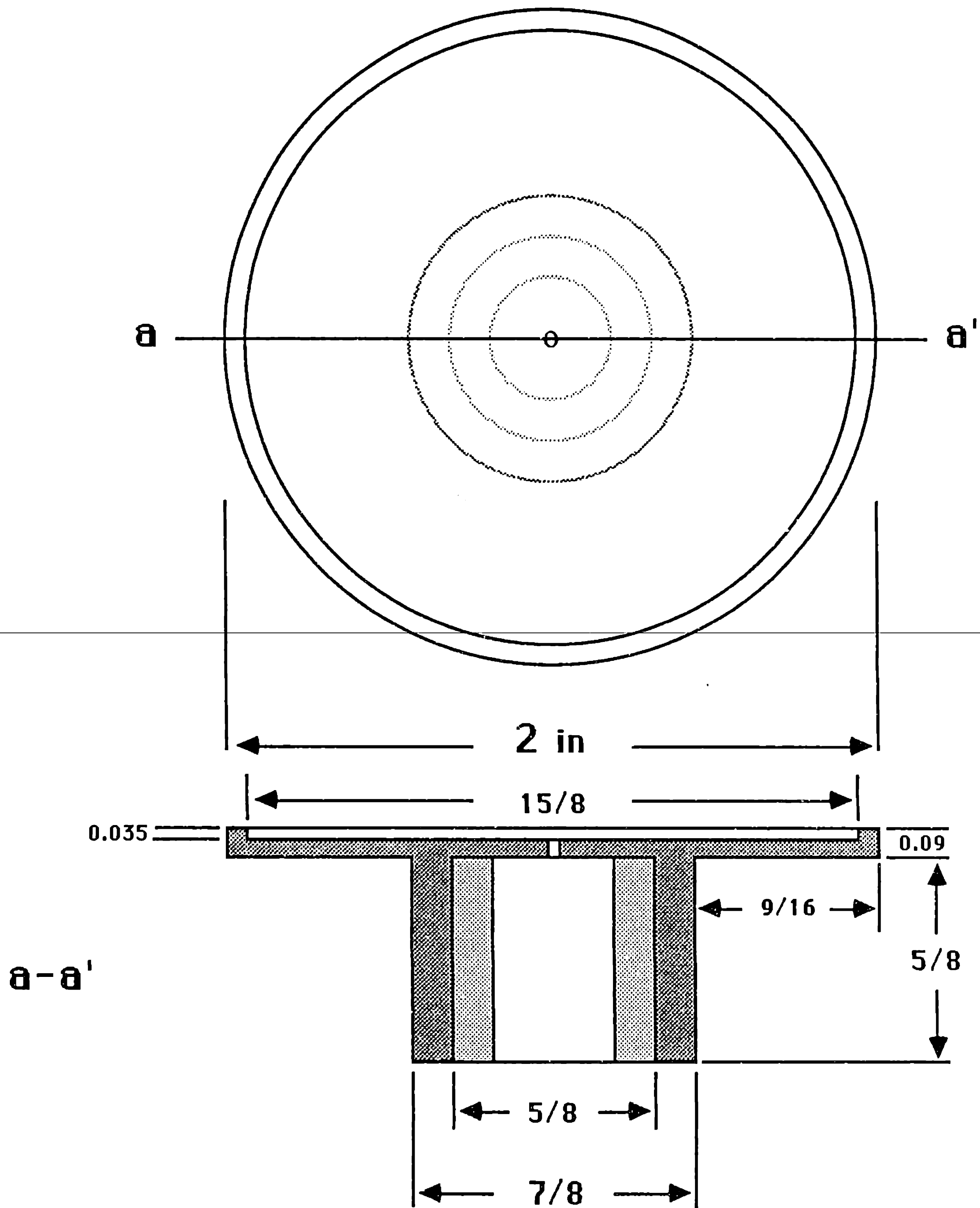


Figure 29: Bottom part of the vacuum spinning chuck

## 3.6 Fabrication of Released Structures

Particular suspended thin film structures are useful in studying the mechanical properties of that film. This concept is explained in detail in chapter 5. In this section, a process is outlined that can be used effectively to fabricate suspended polyimide structures.

Figure 30 outlines the process steps for fabricating one particular structure. Other structures on the same mask are processed identically. Initially, silicon diaphragms of appropriate size and thickness (normally 4.7 $\mu$ thick) are fabricated as outlined in section 3.1. The native oxide is removed since it deforms the diaphragms due to the compressive stress in the oxide (figure 30.A). Polyimide film is deposited on the substrate as outlined in section 3.5. At this point, 2000 Å of Al is evaporated on the polyimide film for masking and patterning (figure 30.B). The Al on the polyimide over the silicon membranes is patterned by negative resist lithographic process (figure 30.C). Al at this point acts as a mask to transfer the pattern to polyimde in $O_2$ plasma (figure 30.D). It is removed after patterning the polyimide. Finally, the thin silicon diaphragm is removed releasing the structures (figure 30.E). Appendix G outlines the details of the process.

The two steps in the above process involving etching of Al can be done either in a $CCl_4$ plasma or by a wet chemical etch (i.e. PAN etch). The plasma process provides excellent line definition and is better for the patterning step. On the other hand, the Al film is more effectively removed at the final stage by the use of a wet chemical etch. It is necessary to remove the Al before etching away the silicon support diaphragm. Otherwise, the stress in the Al film destroys the polyimide structures.

Figure 31 is SEM photograph of a regional view of the substrate with many suspended structures. The process is very reliable with perfect yield. There are no difficulties in carrying the substrate through lithographic processes as long as spinning is done using the custom designed vacuum spinning chuck previously explained.

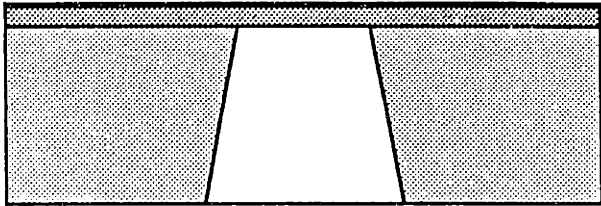
(A) cross-section

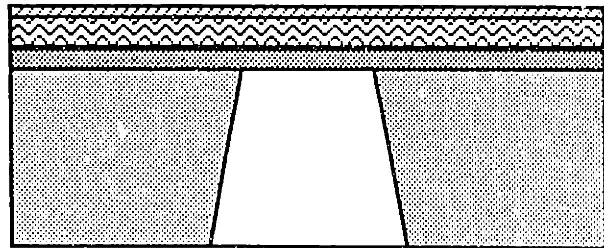
(B) cross-section

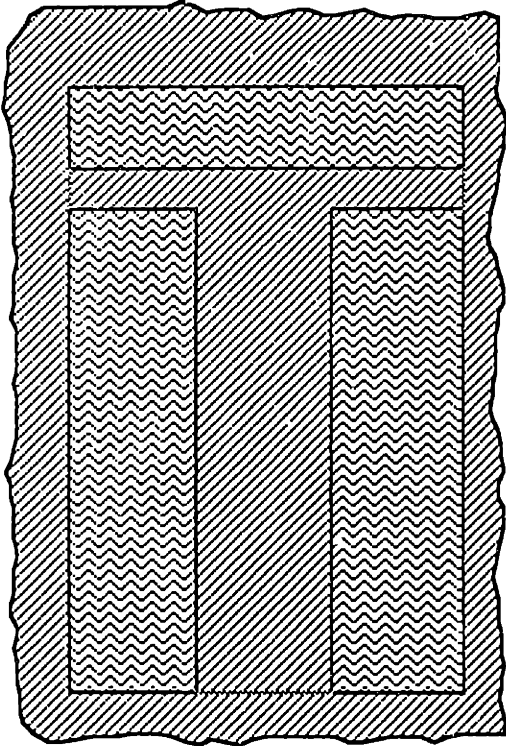
(C) top view

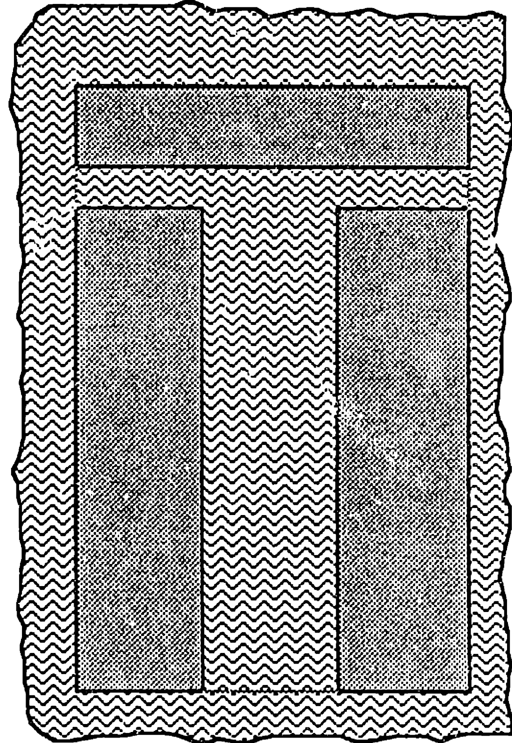
(D) top view

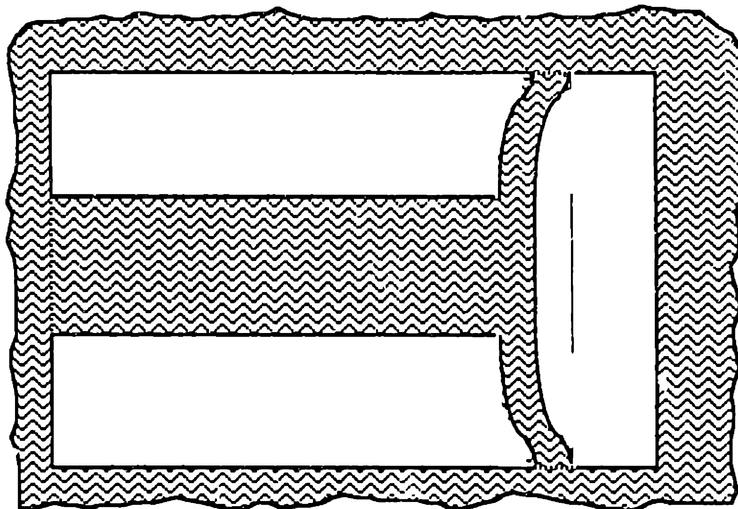
(E) top view

Figure 30: Fabrication process for a suspended polyimide structure

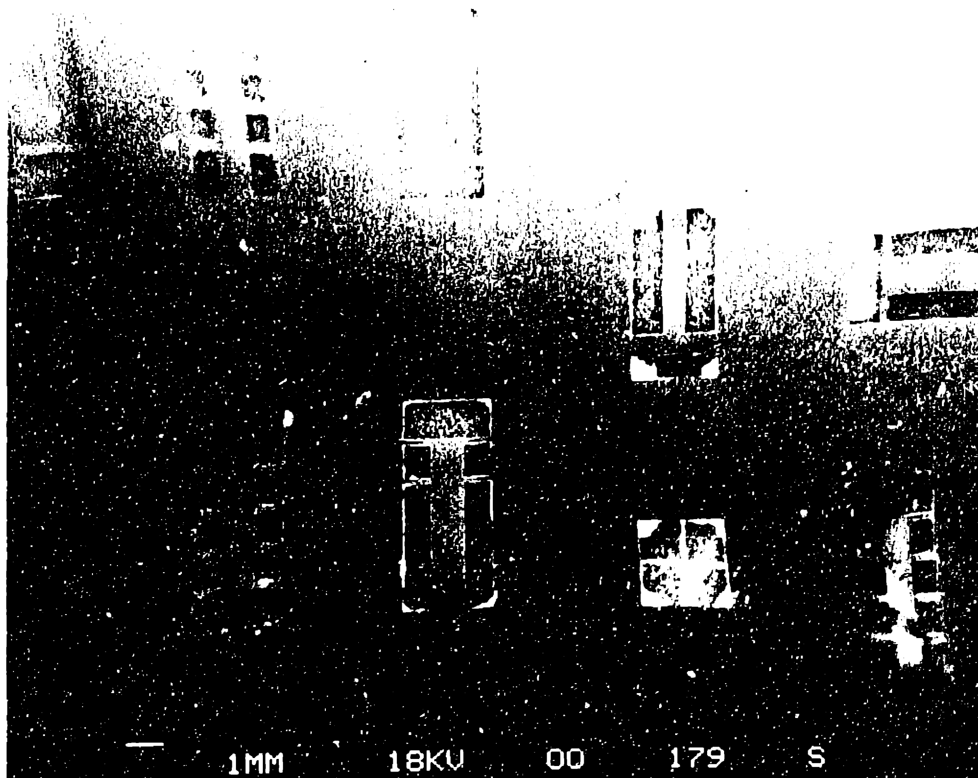


Figure 31: SEM photograph of several suspended structures

Figure 31: SEM photograph of several suspended structures



INTENTIONAL DUPLICATE EXPOSURE

# 4 Suspended Membranes

Suspended membranes can be used to study mechanical properties, including stress, Young's Modulus, yield strength, and fracture strength of the material [94]. A standard load-deflection study on the membrane provides the desired information. This method has been used extensively for studying mechanical properties of various films [95]–[110]. Such membranes can also be used in studying adhesion of the film to the substrate [4,111]. This is done by pressurizing the membrane from the back (to a bubble shape) until the film peels away from the substrate. By measuring the input work to the system and subtracting the strain energy of deformation for the membrane, the work of adhesion of the interface can be extracted. This method, also called the "blister test", has been used to study adhesion of thin films [1,5,112,113] films. Even though many of the cited work are not performed in the context of integrated circuit technology, the concepts can be transferred easily.

In general, metallic films have been studied more often for mechanical properties because reproducible results are easier to achieve. The final characteristics of polymer films are sensitive to the exact chemistry of the material started with and the subsequent processing. In addition, the requisite condition for conducting the above studies is the fabrication of defect (i.e. pin-holes) free membranes. In many cases, it is difficult to protect the polymer film during the membrane fabrication process, especially drilling of the substrate by wet chemicals. The silicon micromachining processes that have been discussed in the previous chapter are ideal for reproducible fabrication of thin film membranes, especially polymers such as polyimide.

In this chapter, the mechanics of load-deflection and peel behavior of such membranes will be discussed. The experimental method for studying load-deflection and peel behavior of polyimide membranes (fabricated using the detailed process of section 3.5 and appendix F) and the data are presented and discussed.

## 4.1 Load-deflection Behavior of Suspended Membranes

When a plate is loaded (in this case differential pressure is applied to the plate), it deflects. Initially, the deflection is a linear function of the load since the bending moment is the dominant component resisting the deflection. As the load increases, such that the deflections approach the thickness of the plate, the inplane tensile

stresses due to the stretching of the middle plane stiffen and add considerable load resistance to the plate. In this regime, the load is a cubic function of the deflection such that the plate becomes more resistant to bending. Figure 32 [115] demonstrates this behavior for a clamped-edge circular diaphragm under uniform pressure. Small deflection theory refers to the bending problem while large deflection theory accounts for the membrane stresses. Plate analysis are widely available [114]–[116] but mostly discuss the deflection behavior in the linear (small deflection domain). In this domain, closed form solutions for the deflection curve of square and circular plates are attainable by simple analysis. The problem of large deflection of plates, especially square plates, is difficult to solve accurately and closed form solutions are available only when simplifying assumptions are made (generally assumptions about the shape of the deflection curve).

Suspended thin polymer film diaphragms have negligible resistance to bending, meaning that the load-deflection behavior for these membranes is practically in the nonlinear region. The membrane stresses are the dominant component that resist bending, such that in interpretation of the load-deflection data, large deflection analysis must be used. By assuming that the thin polymer film acts as a membrane, meaning that stress is uniform across its thickness, the load-deflection analysis is simplified considerably. In this way, the three dimensional problem is reduced to a two dimensional one. This assumption is reasonable since the thickness of the film is very small compared to all other dimensions.

The load-deflection relation for square and circular membranes have the same functional form and parameter dependencies but differ in numerical constants that account for the change in the geometry. To demonstrate the mechanics of the problem, such as the contributions of membrane stresses and the intrinsic stress of the film, the load-deflection analysis for a clamped circular membrane [5] is presented here. This approach is chosen because analysis for circular membranes is simple and the concepts are clearly demonstrated. The ideas are then extended to analyze square membranes.

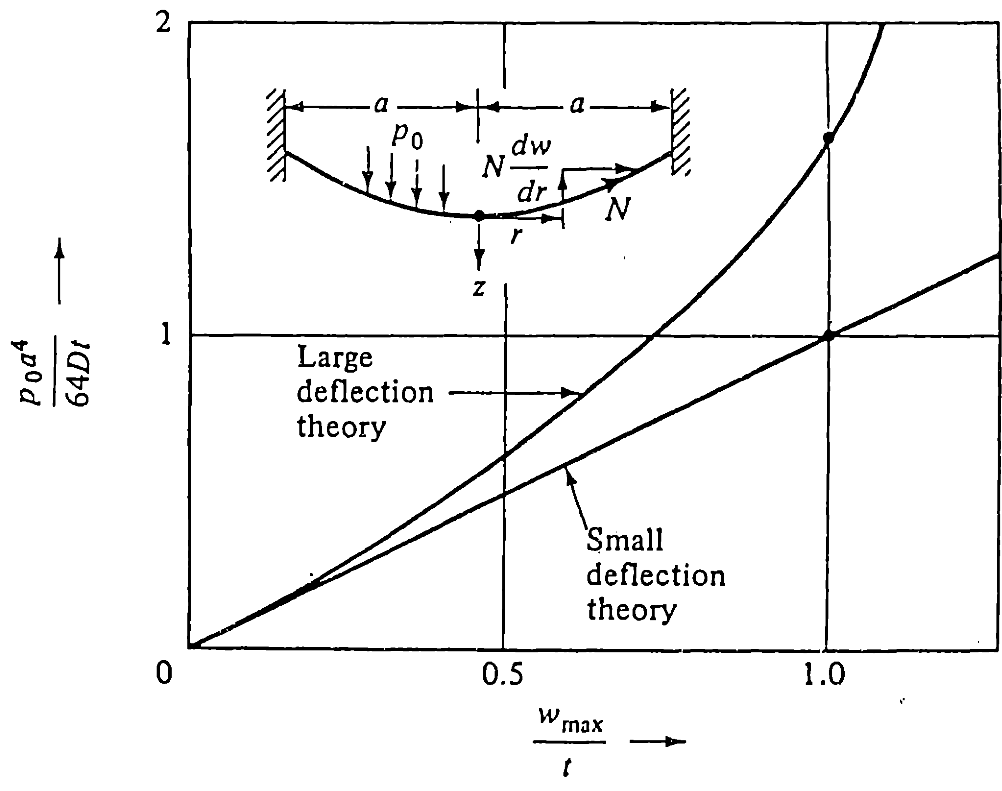


Figure 32: Load-deflection behavior of a circular membrane under uniform pressure

Figure 33 describes the parameters. In general, the strain, $\varepsilon_\phi$, is given by:

$$\epsilon_\phi = (\frac{1}{E})(N_\phi - \nu N_\theta), \tag{2}$$

where $N_\phi$ and $N_\theta$ are the maridonial and the circumferential stresses, and E is the modulus. The critical simplifying assumption that is made here is that the deflected membrane shape is a spherical cap. In that case,

$$N_\phi = N_\theta = \frac{pr}{2t}, \tag{3}$$

where p is the applied pressure. The strain in the spherical cap is

$$\epsilon_\phi = \frac{r\alpha}{a} - 1, \tag{4}$$

where

$$\alpha = \arcsin(\frac{a}{r}) \approx \frac{a}{r} + (\frac{1}{6})(\frac{a}{r})^3 + \ldots \tag{5}$$

equation (5) assumes that a, the radius of the membrane, is small compared to the radius of curvature, r. This is a good assumption since a deflection on the order of the radius of the diaphragm would cause very large strains (over 55%). For polyimide films [117], even if the film does not ruptured at these large strains, it is no longer linearly elastic.

By substituting equations (4) and (5) in equation (2) and rearranging,

$$N_\phi = \frac{Ea^2}{6(1-\nu)r^2}. \tag{6}$$

Setting equation (6) equal to equation (3), the following is derived:

$$p = \frac{Eta^2}{3(1-\nu)r^3}. \tag{7}$$

From the geometry,

$$r = \frac{a^2 + h^2}{2h} \approx \frac{a^2}{2h}. \tag{8}$$

Substituting equation (8) into equation (7), the result is

$$p = \frac{8Eth^3}{3(1-\nu)a^4}. \tag{9}$$

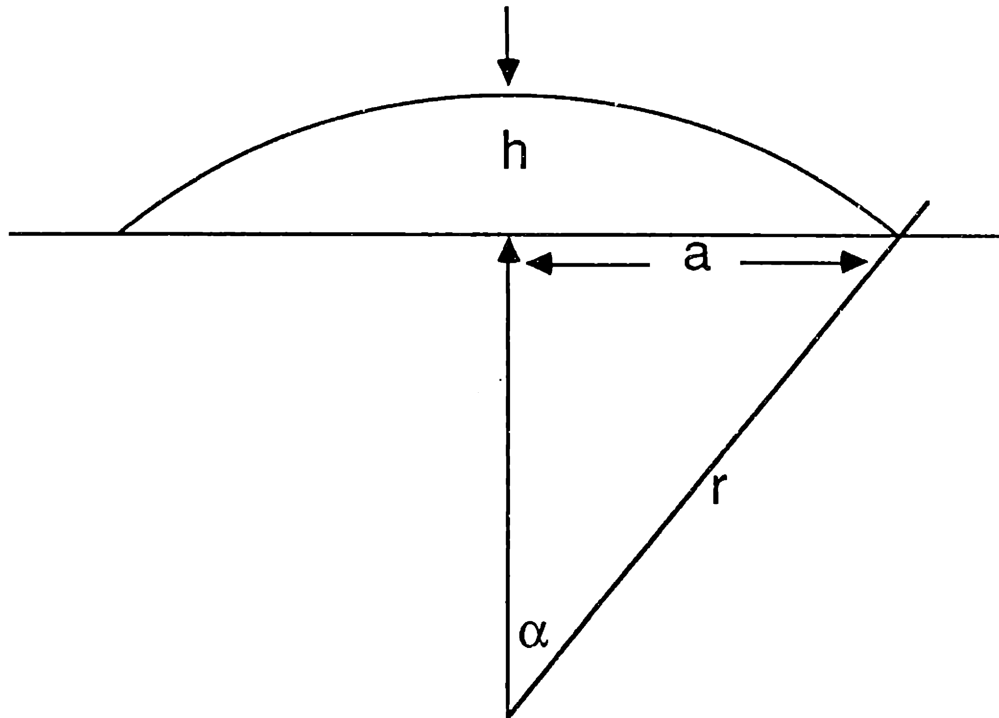


Figure 33: Description of parameters for a circular membrane

This result as expected shows the nonlinear relation between the load and the deflection. When the membrane is deflected, the middle plane is stretched and the supports exert a lateral tensile force that increases as the square of the deflection. This force creates a bending moment that opposes deflection and gives rise to the cubic relation.

The above derivation assumes that when the membrane is not loaded, it should be flat and without any stress. This is observed from equation (6) which reduces to zero when $r = \infty$; (membrane is flat). But thin films deposited on substrate of a different material develop both thermal and intrinsic stress. In the case of a polymer film such as polyimide, the film as deposited is under tensile stress due to volume shrinkage at cure and thermal coefficient of expansion mismatch effect. This intrinsic tensile stress in the film has to be accounted for since it will create a bending moment that resists deflection. Since the tensile stress, intrinsic to the film, is not a function of deflection, it results in a linear relation between the load and the deflection. Under these conditions, the intrinsic tensile stress can be added to the membrane stress, created by stretching due to deflection, in equation (6) to give:

$$N_\phi = N_0 + \frac{Ea^2}{6(1-\nu)r^2}, \tag{10}$$

where $N_0$ is the intrinsic tensile stress. When the membrane is not loaded, $r = \infty$, the stress is equal to the intrinsic stress of the film; when it is loaded, the second term on the right accounts for the membrane stresses.

The deflection as a function of load is

$$p = \frac{4th}{a^2}[N_0 + \frac{2E}{3(1-\nu)}(\frac{h}{a})^2], \tag{11}$$

which is also used by Beams [96] in studying the load-deflection behavior of thin gold and silver films. It is obvious that by taking load-deflection data on a circular diaphragms and fitting the data to a polynomial of the above form, the stress and the Young's Modulus can be extracted. In addition, by calculating the stress and the strain from the data using the equation (10) and (4) a stress-strain curve can be plotted to extract the yield strength and the fracture strength of the film. Equation (11) shows that, if the intrinsic stress term is large in comparison with the second term, the load-deflection curve will be dominated by the linear term, especially at small deflections.

It should be kept in mind that this is a first order analysis, depending on the assumptions that the deflected membrane shape is spherical and strain is uniform over the surface of the cap. As Beams [96] has shown, using a more sophisticated theory, the terms containing the intrinsic stress and modulus in the deflection relation

$$p = \frac{4th}{a^2}[N_0 + \frac{(5-\nu)E}{4(1-\nu)}(\frac{h}{a})^2 + \frac{(13-7\nu)E^2}{288(1-\nu)N_0}(\frac{h}{a})^4] \tag{12}$$

are not readily separable. It has also been suggested [99] that the deflection surface may not be spherical, such that the computed stresses are in error by a factor of 2.

The functional form and the parameter dependencies for the load-deflection relation of a square membrane is the same as equation (11) but with different numerical constants, accounting for the change in the geometry. The Ritz method [115] provides a simple approach for determination of the deflection of membranes. The strain energy associated with the stretching of a membrane is given by

$$U = \frac{t}{2}\iint(\sigma_x\epsilon_x + \sigma_y\epsilon_y + \tau_{xy}\gamma_{xy})\,dx\,dy \tag{13}$$

where

$$\epsilon_x = \frac{\partial u}{\partial x} + \frac{1}{2}(\frac{\partial w}{\partial x})^2, \tag{14}$$

$$\epsilon_y = \frac{\partial v}{\partial y} + \frac{1}{2}(\frac{\partial w}{\partial y})^2, \tag{15}$$

$$\tau_{xy} = \frac{\partial v}{\partial x} + \frac{\partial u}{\partial y} + (\frac{\partial w}{\partial x})(\frac{\partial w}{\partial y}), \tag{16}$$

$$\sigma_{ij} = E\epsilon_{ij}, \tag{17}$$

and $v, u$, and $w$ are the $x, y$, and $z$ displacements. A series solution for the deflection form of the membrane which is reasonable and satisfies boundary conditions is selected. The strain energy of deformation and the work input into the system are calculated, and the total potential energy of the system is minimized with respect to the unknown coefficients in the deflection form equations, resulting in a relationship between the load and the deflection. The deflection of a square membrane is found by the Ritz method [114,115], not accounting for the film's intrinsic stress and assuming the deflection forms:

$$w = h\cos(\frac{\pi x}{2a})\cos(\frac{\pi y}{2a}) \tag{18}$$

$$u = C\cos(\frac{\pi y}{2a})\sin(\frac{\pi x}{a}) \tag{19}$$

$$v = C\sin(\frac{\pi y}{a})\cos(\frac{\pi x}{2a}), \tag{20}$$

where $2a$ is the length of a side of the square. These are the first terms from an infinite series solution of similar form terms all satisfying the boundary conditions. The load-deflection relation is

$$p = 1.953Et\frac{h^3}{a^4} \tag{21}$$

for $\nu = 0.25$. It has the same form as equation (9) but with a different numerical constant which is due to the square geometry and the different form of deflection shape assumed (equation (9) was derived for a spherical shape and $\nu$ was left in). Mark Allen [6], co-worker on the mechanical studies of the polyimide membranes, has accounted for the intrinsic tensile stress in the polyimide film by finding the elastic strain energy contribution due to this component and adding that contribution to the total potential energy of the system. The resulting load-deflection relationship is

$$p = \frac{3th}{a^2}[N_0 + 0.6E(\frac{h}{a})^2] \tag{22}$$

for $\nu = 0.25$. As expected, the functional form is exactly the same as equation (11). However, due to the square geometry and the different deformation shape assumed, the numerical constants are different.

In this work, equation (22) is used to fit the data from load-deflection studies. The coefficient of the linear term is used for extraction of the stress while the coefficient of the cubic term is used for extraction of the Young's Modulus. The accuracy of the extracted parameters depends on the accuracy with which the assumed deflection shape matches the actual shape. As more terms are included, the accuracy of the solution increases, so does the complexity of the formulation. The terms containing $N_0$ and E may not be readily separable in that case.

## 4.2 Mechanics of Blister Test

Hinkley [5] has demonstrated the use of blister test for studying the adhesion of polymer films to the substrate by pressurizing a circular polymer membrane until the interface adhesion fails and the film peels away from the substrate. This approach

can be used to measure the work of adhesion of polyimide to silicon dioxide/silicon substrates by using the same square membranes which are used for study of the mechanical properties.

The mechanics of this problem has been analyzed for circular diaphragms assuming linear load-deflection behavior, small deflections, and no residual stress in the membrane film [4]. After peel is nucleated using a square diaphragm, the base of the blister becomes circular since there is no preferred peel direction due to the symmetry of the problem. After the nucleation, the same analysis as for circular diaphragms applies. Allen [6] has extended the same concepts to include nonlinear load-deflection behavior for large deflections of membranes with residual stress. In general the critical pressure, the pressure at which peel initiates, increases as the work of adhesion of the interface is increased and decreases as the blister radius (area) is increased.

The physical behavior is as follows. Initially, the membrane is deflected under the applied pressure. As the pressure increases, the membrane undergoes increasing deflection. Ultimately, the critical pressure is reached (which would initially be different for a square membrane) and peel initiates (as soon as peel nucleates, the blister base becomes circular). Peel initiates at this point because the total potential energy of the system is minimized by dissipating some of the input energy in creating fracture surface. If the pressure is held constant at the initial critical pressure, the film peels to the edge of the sample instantaneously. As the film peels, the blister radius increases reducing the critical pressure (pressure needed to start peel at that blister radius). Since the pressure is held at the critical pressure that was necessary to nucleate peel at the start, the peel never stops. If the pressure was to be reduced below the critical pressure for the radius to which the blister has grown, the peel would stop.

Hinkley [5], conducted the peel experiment using a constant pressure peel method which presented the above stability problem. To avoid the stability problem, pressure is increased by injection of a limited quantity of air into a sealed cavity under the membrane. Once sufficient quantity of air is injected to raise the pressure in the cavity to the critical pressure, the film peels which in turn increases the volume of the cavity and reduces the pressure. If the increase in the volume at a particular blister radius is large enough to reduce the pressure below the critical pressure at that radius, the blister growth stops. The process can be repeated by a new injec-

tion which will initiate peel and so on. The controlled-injection peel method has been demonstrated by Dannenberg [112].

The cavity volume under the membrane called "dead volume", including the etched cavity in the substrate and other necessary channels for air injection, should be comparable to the volume generated when the blister grows. If the dead volume is very large, the change in the volume generated by blister growth due to peel will not be sufficient to reduce the pressure below the critical pressure at that peel radius, and the film will peel a long way even if it does not peel to the edge of the sample instantaneously.

In this study, the work of adhesion for each incremental peel (as described above) can be found by integrating the area under the blister's pressure-volume curve and then subtracting the work that went into stretching of the blister. If the experiment is performed twice, once while the film is peeling and once after the film has peeled, the net work done to peel the film, $W_{peel}$, is found by:

$$W_{peel} = W_{initial} - W_{final}, \tag{23}$$

where $W_{initial}$ is the work done to peel and stretch and $W_{final}$ is the work done to stretch. The average work of adhesion, $\gamma_a$, over the peeled area is

$$\gamma_a = \frac{W_{peel}}{A}, \tag{24}$$

where A is the peel area. The input work for each part of the experiment can be calculated by integrating the area under the blister pressure-volume curve. In the blister test of Dannenberg [112], the pressure-volume behavior of the blister was measured using an incompressible pressurizing fluid (mercury). This allows the analytical simplification that the blister volume is equal to the amount of mercury injected such that

$$W_{peel} = \int_{V_{b,f}}^{V_{b,i}} (P_1 - P_2)\, dV_b = \int_{V_{s,f}}^{V_{s,i}} (P_1 - P_2)\, dV_s, \tag{25}$$

where $V_{b,i}$ and $V_{b,f}$ are the initial and final volumes of the bubble, $V_{s,i}$ and $V_{s,f}$ are the initial and final volumes of the syringe (or the mercury supply chamber) and $P_1$ and $P_2$ are the pressures before and after peel, respectively. In this study, it was desired to use air as the pressurizing fluid; since air is compressible, it is necessary to relate the total volume of air injected by the syringe to the total blister volume. Allen [6] has done a careful analysis in which he accounts for the compressibility factor and derives an expression for $W_{peel}$ given by:

$$W_{peel} = \int_{V_{s,f}}^{V_{s,i}} (P_1 - P_2)\, dV_s - P_{1,0} V_0 \ln(\frac{P_{1,f}}{P_{1,i}}) + P_{2,0} V_0 \ln(\frac{P_{2,f}}{P_{2,i}}), \tag{26}$$

where zero subscripts specify the system parameters before peel and the subscripts $i$ and $f$ refer to the initial and final pressure after each injection. Using this approach, the average work of adhesion over an area can be determined by measuring the pressure and recording the volume of the injection syringe before and after each injection.

## 4.3 Experimental Instrumentation

In order to apply differential pressure for load-deflection and adhesion measurements, the trapezoidal cavity in the wafer (consisting of the etched away part of the silicon) must be sealed and some provision must be made for applying and measuring the pressure. The designed testing apparatus is shown in figure 34. The sample is placed on a 2.75 inch diameter aluminum vacuum plate and the periphery of the cavity is sealed with vacuum grease. The vacuum plate has a vertical hole 0.05 inch in diameter through its center that locates under the membrane. The vacuum plate is placed on a 3x3x0.25 inch aluminum plate, which in turn has a vertical hole through its center that locates under the vertical hole of the vacuum plate and connects the trapezoidal cavity to the pressure transducer. The top and the bottom of this hole are fitted with rubber o-rings to provide a seal when the apparatus is clamped. Another hole, perpendicular to the vertical hole was drilled just large enough to allow the introduction of a microliter syringe needle which was subsequently sealed into the plate using RTV adhesive sealant. The dead volume contribution from these connecting holes is about 100 microliters. A 3x3x0.4 inch aluminum base plate, incorporating the pressure transducer, is placed under the middle plate, automatically aligned by alignment pins.

For load-deflection measurements, wafer lifting from the vacuum chuck presented difficulties. A cushion of 1/16 inch dental gum with a hole large enough to uncover the membrane was laid on the wafer. An upper support of 1/16 inch 304 stainless steel, 2.75 inches in diameter, was placed over the cushion. Finally, a 3x3x0.125 inch clamping plate of 1/16 inch 304 stainless steel with a center hole 2.2 inches in diameter was placed over the upper support. The entire assembly was then clamped, using four 7/16 inch bolts running through the four corners of the three

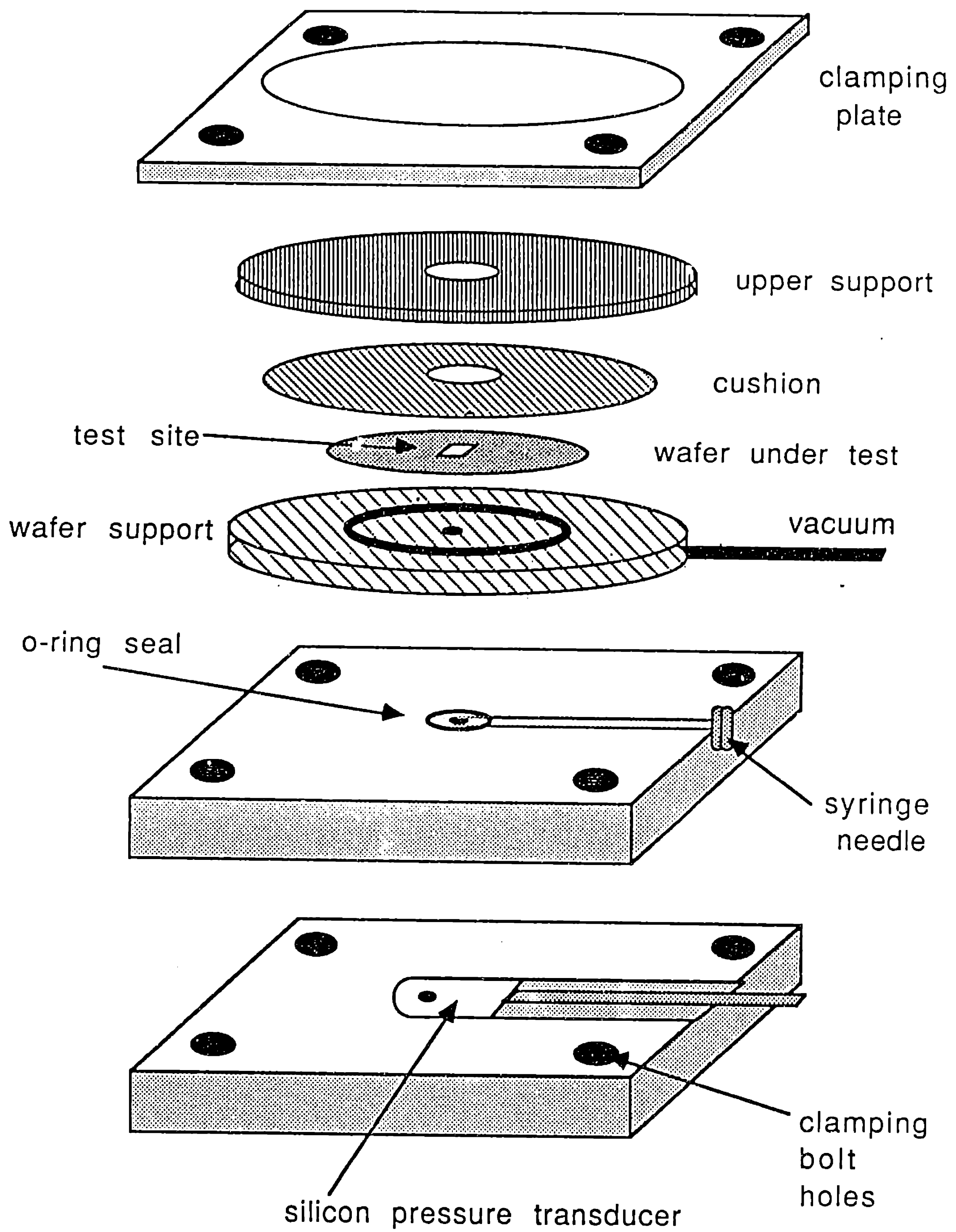


Figure 34: The membrane testing assembly

plates until an air-tight seal was achieved.

Using this testing assembly, it was possible to clamp the wafer in an air-tight fashion, apply differential pressure by injection of a quantity of air, measure the pressure, and remove the sample nondestructively. At the same time, the membrane site was exposed such that the deflection could be monitored by an optical microscope.

## 4.4 Calibration of the Pressure Transducers

The pressure measurements were conducted using differential pressure transducers with voltage output made by Kulite Semiconductor [118] and Honeywell Microswitch [119]. The two Kulite trnasducers are specified for the pressure ranges 0-1 psi and 0-5 psi. These were used for the adhesion measurement because their dead volume is only a few microliters. The Honeywell transducer is specified for the pressure range of 0-15 psi and was used for the load-deflection studies because of its larger range of operation. Its large dead volume would not effect the load-deflection studies.

The transducers were calibrated using a standard manometer with the reference side of the manometer open to the atmosphere. The 0-1 psi pressure transducer was calibrated using a water manometer while the two others were calibrated using a mercury manometer. The calibration was done at room temperature and was not corrected.

The Kulite transducers were calibrated and used with 10V excitation while the Honeywell transducer was calibrated and used with 8V excitation. The output voltages were measured using a Keithely digital multimeter. The calibration curves for the three pressure transducers are shown in figure 35.

## 4.5 Load-deflection Measurement Methodology

The sample is mounted in the test apparatus described in section 4.3. A small volume of air is initially injected to raise the pressure, test for leaks, and to insure that the air flow to the membrane is not blocked. The entire test apparatus is placed on a microscope stage and the center of the deflected membrane is found using the microscope to locate the point on the membrane undergoing maximum deflection. The pressure is then reduced to zero and the microscope is focused on the now

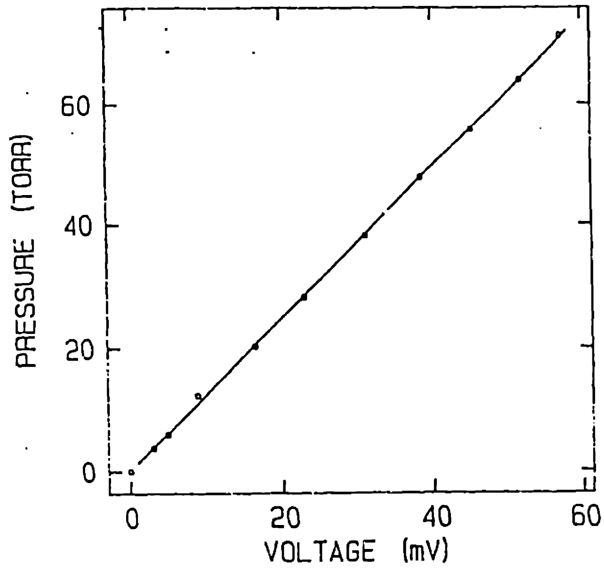


(a)

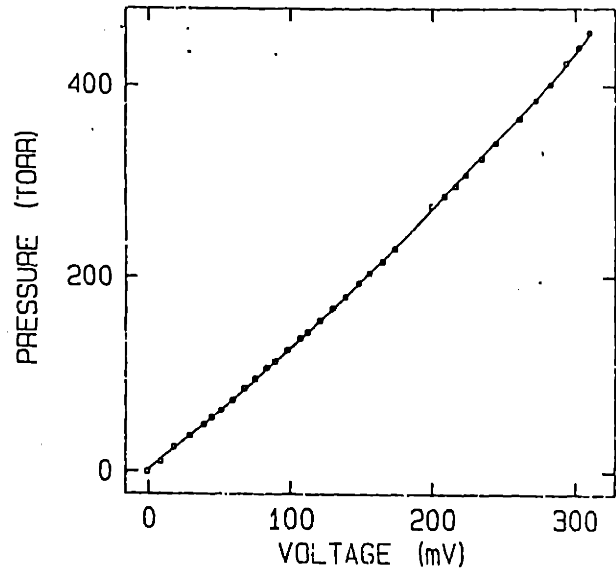


(b)

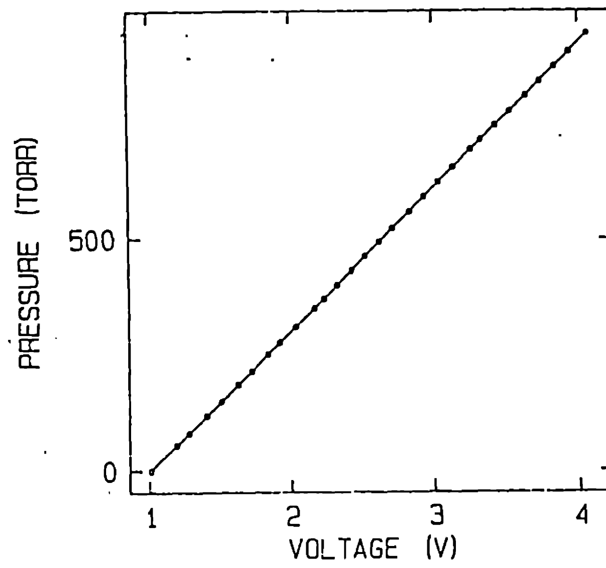


(c)

Figure 35: Calibration of pressure sensors

(a) 1psi Kulite sensor
(b) 5psi Kulite sensor
(c) 15psi Honeywell sensor

flat membrane. Differential pressure is then applied using the microliter syringe. The membrane deflects and the image goes out of focus. The microscope stage is then lowered to bring the image back into focus while the travel of the stage is monitored using a digital indicator accurate to $\pm 1$ micron. The major component of the error in measuring the deflection by this method is determining when the image is exactly in focus. the reoroducibility in the deflection measurements is better than $\pm 4$ microns.

## 4.6 Suspended Membrane Load-Deflection Results

Load-deflection studies are performed on polyimide membranes ranging in size from 2x2 to 10x10 mm and in thickness from 6 to 10 microns. The deflection of the center of the membrane is measured as a function of the applied pressure (using the experimental instrumentation and procedure outlined in sections 4.3-4.5). The load-deflection data is then fit to equation (22), which is repeated here:

$$p = \frac{3th}{a^2}[N_0 + 0.6E(\frac{h}{a})^2], \tag{27}$$

where E is Young's Modulus, $N_o$ is the intrinsic tensile stress in the film, 2a is the length of one side of the membrane, t is the thickness of the film, p is the applied pressure, and $h$ is the deflection in the center. The fitting procedure uses a least squares formulation implemented by a Fortran code. The inputs to the program are the experimentally measured parameters: t, $h$, p, and a. The outputs of the program are the fitted parameters E and $N_o$.

Table II presents the stress and modulus data acquired from polyimide membranes of different size and thickness. This table has been partitioned, grouping samples that were fabricated in the same batch together. The membranes are fabricated using Du Ponts's BTDA-ODA/MPDA cast in multiple coats (prebaked for 14 minutes at 135°C after each coat and cured at 400°C for 45 minutes at the end), using the fabrication process outlined in section 3.5 and appendix F. All the samples in the table were nominally processed the same, but sufficient care was not taken to insure this condition. The higher stress in the 3x3 mm samples is attributed to the process variations during the soft-bake step. The temperature of the soft-bake oven used is extremely difficult to control, which may have resulted in temperature variations during this critical step. The high stress in sample #11 is not understood. The elapsed time between the completion of a sample and performing the

measurements ranged from one hour to ten days. The samples were stored in ambient environment during this period. It is not clear that the storage time period would affect the reproducibility adversely.

| # | SIZE (2a) (mm) | THICKNESS (± 0.5) (μ) | STRESS (MPa) | MODULUS (GPa) |
|---|---|---|---|---|
| 1 | 2 | 10.6 | 29.7 | 0.71 |
| 2 | 2 | 10.5 | 31.4 | - |
| 3 | 3 | 10.6 | 43.8 | 6.9 |
| 4 | 3 | 6.3 | 49.4 | 8.6 |
| 5 | 3 | 10.3 | 45.3 | 3.4 |
| 6 | 4 | 10 | 30.0 | 2.6 |
| 7 | 6 | 10 | 33.2 | - |
| 8 | 6 | 10 | 28.7 | 1.5 |
| 9 | 10 | 8.3 | 35.7 | 2.9 |
| 10 | 8 | 8.4 | 32.7 | 3.0 |
| 11 | 8 | 8.5 | 39.8 | 3.2 |
| 12 | 10 | 7.0 | 30.2 | 3.2 |
| 13 | 10 | 7.5 | 30.2 | 3.2 |
| 14 | 8 | 7.1 | 30.5 | 2.2 |

Table II: Residual stress and modulus data

Figure 36 presents typical load-deflection data for six different size membranes (in order from above: #12, #11, #8, #6, #4, #1). The membrane thicknesses are not the same (thicknesses listed in Table II). Qualitatively, the data behaves as expected. The deflections increase as the membrane size is increased. The deflections increase as the membranes are made thinner (this has resulted in the comparable deflections for the thinner 3x3 mm membrane and the 4x4 mm membrane which are seen nearly as one curve). In the applied pressure range, the load-deflection behavior of the smaller membranes is largely linear and the curvature increases substantially for the large membranes. The data (table II) scales correctly as a function of the membrane size and thickness, demonstrating the merit of equation (22) derived from the previously described model.

Excluding the 3x3 mm samples and one of the 8x8 mm samples (sample #11), the intrinsic tensile stress values are in good agreement. The intrinsic tensile stress is $31.4 \pm 6.0$ (20% deviation from the average) for the particular chemistry polyimide and processing procedure used here. This result is in agreement with stress measurements made using the wafer curvature curvature technique [120].

The extracted modulus values are in good agreement only for the samples with large membranes (8x8 mm and 10x10 mm). The reason is that for smaller size membranes, the load-deflection behavior is dominated by the film's intrinsic tensile stress in the pressure range applied here. The contribution of the developed membrane stresses due to the stretching of the middle plane of the plate are small. The inability to measure the small curvature of the data for such membranes (figure 36) leads to the large scatter in the extracted modulus values. On the other hand, for large membranes, the membrane stresses become comparable to the intrinsic stress at a much lower load. Figure 36 shows the contribution of the membrane stresses in a 10x10 mm membrane, resulting in a significant curvature in the data for the same pressure range. The scatter in the modulus values form these samples is significantly reduced. Using the value from these samples, the modulus is $3.0 \pm 0.9$ GPa (30% deviation from the average).

To demonstrate that no plastic deformation of the film occurred, multiple load-deflection measurements were carried out on the same sample. In the presence of plastic deformation, the later load-deflection measurements would not reproduce the former ones. No plastic deformation was observed in the conducted measurements. Figure 37 shows typical results from two consecutive load-deflection measurements.

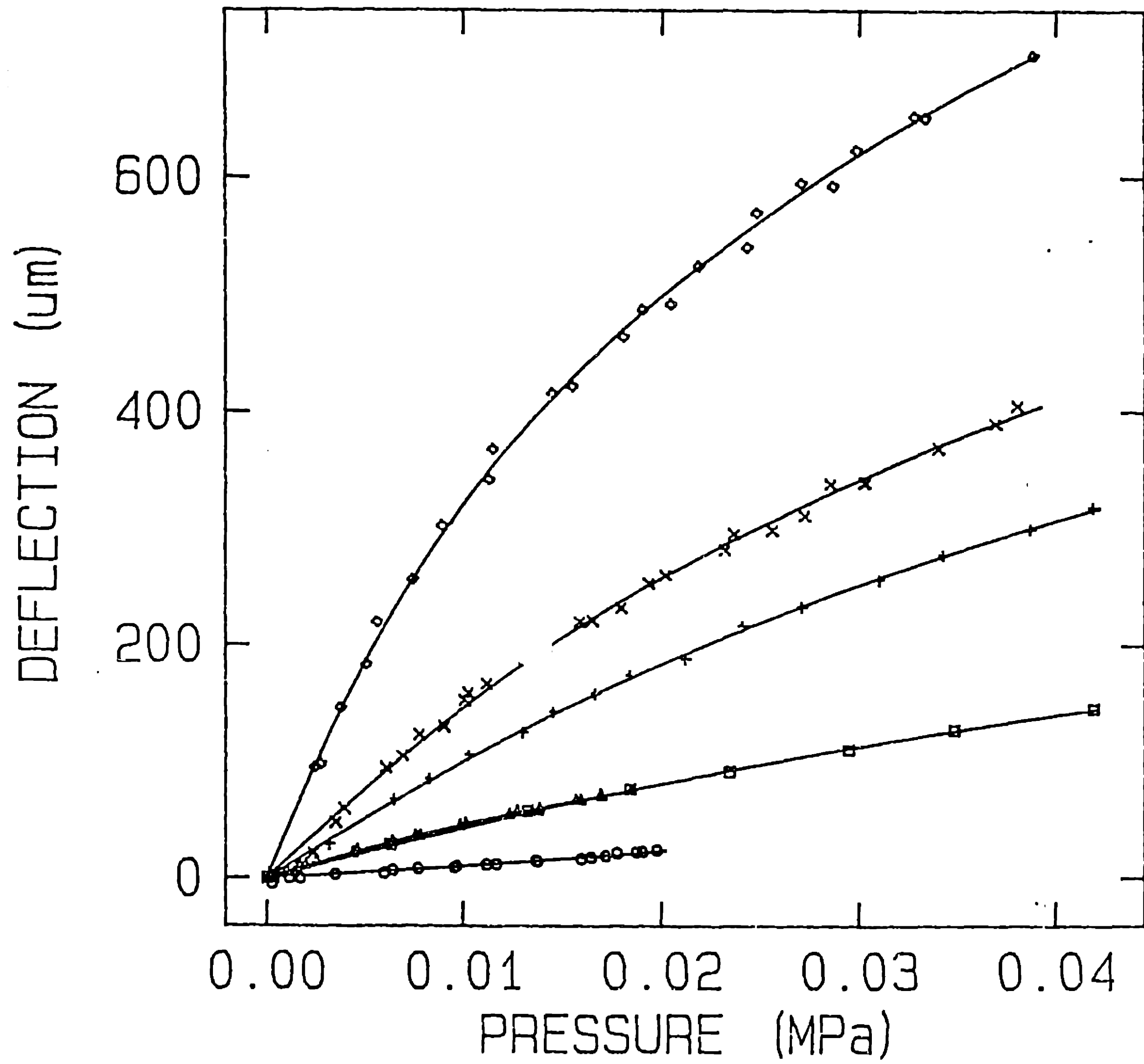


Figure 36: Typical load-deflection data for six different size membranes

The two sets of data are nearly identical. For a 10x10 mm membrane, when the deflection at the center is 600 $\mu$ (the largest deflections measured here), the largest strain in the membrane is less than 2%, meaning that the film is elastic up to this level of strain. Weber and Gupta [117] found that polyimides of comparable chemistry to the one used here are linearly elastic up to about 4% strain. This justifies the assumptions related to the elastic behavior of the film during deformation in the previous derivations.

Since the values of the stress and the modulus are obtained by fitting to equation (22), the integrity of these values is dependent upon the accuracy of the assumptions in deriving this equation. In particular, the deflection shape is taken to be the first term of a series solution of the cosine-cosine form. The accuracy with which this form describes the true deflection effects the extracted values directly. As pointed out previously, if the second term in the series solution is included, the accuracy of the solution improves, and the terms containing the stress and the modulus may not be readily separable. Beams [96] has demonstrated this general idea for a circular membrane in equation (12), repeated here

$$p = \frac{4th}{a^2}[N_0 + \frac{(5-\nu)E}{4(1-\nu)}(\frac{h}{a})^2 + \frac{(13-7\nu)E^2}{288(1-\nu)N_0}(\frac{h}{a})^4] \quad (28)$$

It is instructive to see the significance of the contribution of the added term, containing the stress and the modulus. Since it is complicated to carry out this formalism for a square diaphragm, equation (28)is used with typical values for polyimide membranes to give a first order approximation.

Using $\nu = 0.25$, E$=$ 3.0 GPa, and $N_o = 31.4$ MPa, equation (28) reduces to

$$p = 31.4 + 4750(\frac{h}{a})^2 + 14928(\frac{h}{a})^4, \quad (29)$$

where p is in MPa. For $\frac{h}{a} < 0.1$, the magnitude of the third term is below 2% of the sum of the first two terms. Since the deflections measured here were always smaller than $\frac{a}{10}$, the contribution from the last term is only a few percent. The first order analysis used here should therefore be reasonably accurate.

Overall, it is demonstrated that reproducible and meaningful data regarding the intrinsic stress and the modulus of polyimide films can be obtained by load-deflection studies on suspended membranes of these films. This method can be used to study the intrinsic tensile stress in the film as a function of process parameters when good process control is possible.

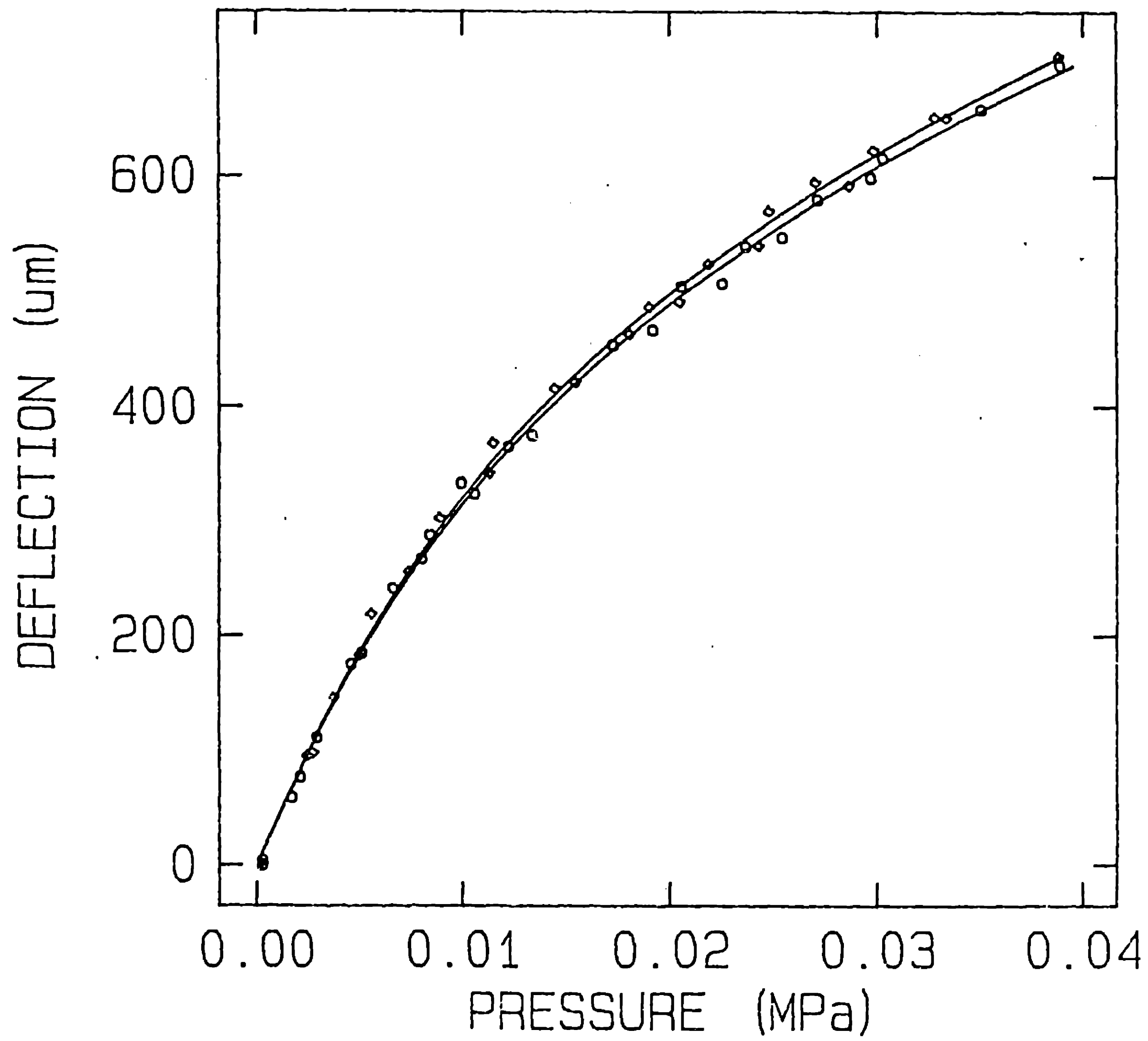


Figure 37: Consecutive load-deflection measurements on sample #12

## 4.7 Adhesion Measurement Methodology

The samples (fabricated as described in section 3.5 and appendix F) are sealed in the test assembly described in section 4.3. Differential pressure is applied until the film peels or bursts. If the film bursts, values for the ultimate tensile strength of polyimide can be extracted; if the film peels, values of work of adhesion can be determined.

It found that blisters could not be nucleated on wafers which had undergone the standard processing described in section 3.5 and appendix F. Methods were used to degrade the interfacial adhesion so that nucleation is achieved. The most successful method involved treatment of the sample with water to hydralize the $SiO_2$ surface, which has been shown to degrade adhesion [121]. Wafers which had previously undergone load-deflection testing were immersed in 90°C water for 21 hours, followed by a cooling down period of various lengths (while still immersed). On samples so treated, it was possible to nucleate peel.

Sharply defined blister radii were created as follows. First, an upper support (see figure 34) was used which had a diameter of 5/8 inches. The differential pressure was then increased until nucleation was achieved and the film peeled to the diameter of the upper support. The pressure at this initial diameter was then recorded. The upper support was remover and a clamping plate with a diameter of 23/16 inches was placed over the wafer. The pressure was raised to the pressure recorded at the initial blister radius, and the syringe volume was recorded. The film was then peeled by injection of air in 10 microliter increments which were measured on the syringe scale. The syringe volume and blister pressure at each injection increment were recorded. This process was recorded until the film had peeled to the diameter of the clamping plate. At this point, pressure was decreased by withdrawing the syringe plunger in 10 microliter decrements until the initial syringe volume was obtained. Again, the pressure and syringe volume at each injection decrement were recorded.

Typical adhesion data showing the blister pressure as a function of cumulative volume of air injection are shown in figure 38. Interpretation of these data and the extraction of the work of adhesion will be discussed in next section.

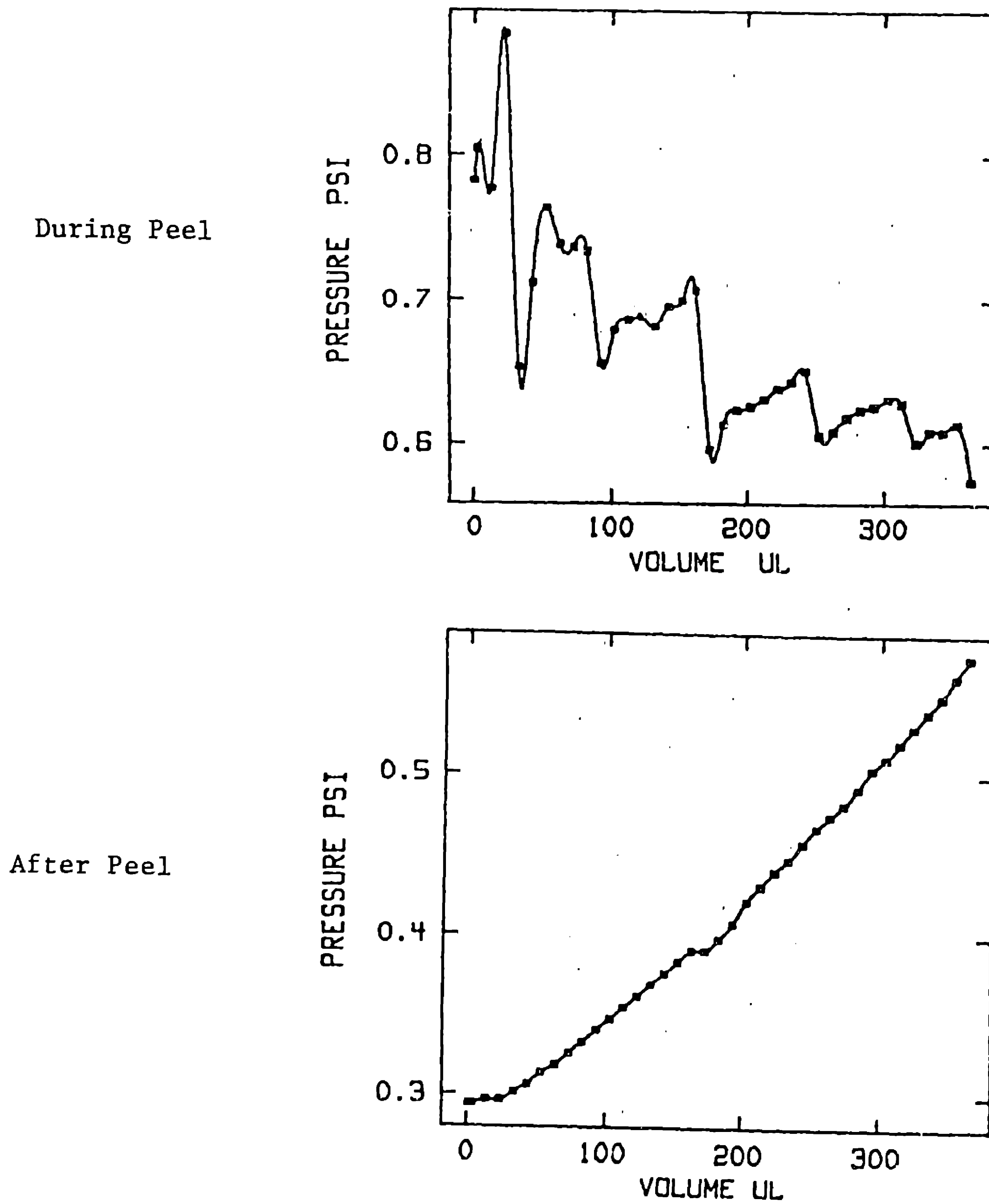


Figure 38: Typical data for blister pressure versus injected air volume

## 4.8 Polyimide-Silicon Dioxide Adhesion Data

As described in the previous section, it was not possible to nucleate peel on wafers which underwent the standard sample fabrication. The polyimide film always burst before adhesion failure was reached. However, it was possible to extract both a lower limit for the work of adhesion as well as the tensile strain at break from the film. These measurements are approximate because the pressure transducers could not be used for measurement at the high pressures necessary to burst the film. Pressure for these measurements was introduced into the test chuck from an in-house pressurized air supply (100 psi max) and measured by the regulator gauge only. The measured ultimate strain is compared with the values form more accurate studies described in the next chapter.

Measurements were conducted on 6x6 millimeter test sites. The pressure at which the film failed is approximately 40 psi. Using equation (22), the deflection at the center of the square membrane at this pressure is 675 microns. The average tensile strain of the film under the above conditions is 4% calculated by integrating the arc-length of the deflection shape (equation (18)). The lower bond for the work of adhesion is calculated by Allen [6] to be 360 $J/m^2$.

For two wafers which had undergone degradative processing as described in the previous section, blisters were nucleated and the work needed to peel and to stretch the film was measured as described in section 4.2. Figure 39 shows the data for the first wafer which received 6 hours of wet cool-down before testing. The circles represent pressure during peel and the diamonds represent pressure after peel. As can be seen, adhesive failure in this case was of the stick-slip type, an effect which has been observed previously for other polymers. Using the analysis of section 4.2, the work of adhesion is calculated to be 0.69 $J/m^2$, substantially below the lower bound calculated above. This degradative effect of water on polyimide/oxide adhesion without adhesion promoters has also been observed by Rothman [121] using the peel test.

Figure 40 shows data taken on the second wafer which received one hour of wet cool-down before testing. Adhesion on this wafer was very nonuniform. As the blister grew, certain points on the film were held down by what appeared to be particles in the film. Adhesive failure from these particles was not realized until the blister had grown to almost surround the defect. These defects also caused the

film to have a much higher average work of adhesion than the film on the previous wafer. The calculated value for the work of adhesion of this sample is 2.0 $J/m^2$.

An interesting effect was observed when these films were allowed to settle flat against the substrates after peel. A small degree of re-adherence of the film appeared to take place; a non-zero amount of work was necessary to re-peel the film. This effect is shown in figure 41. The apparent work of adhesion is 0.49 $J/m^2$.

Unfortunately, there was not enough time for additional adhesion studies. At this point, not enough samples have been processed to comment on the reproducibility of the test or the accuracy of the measured values here. It has merely been demonstrated that the test can be performed quantitatively and controllably. It is evident that the test could not be performed when samples had undergone standard fabrication since the film burst before the adhesion failed. This problem may be avoided by reinforcing the film such that it does not burst easily or nucleating the peel by different methods.

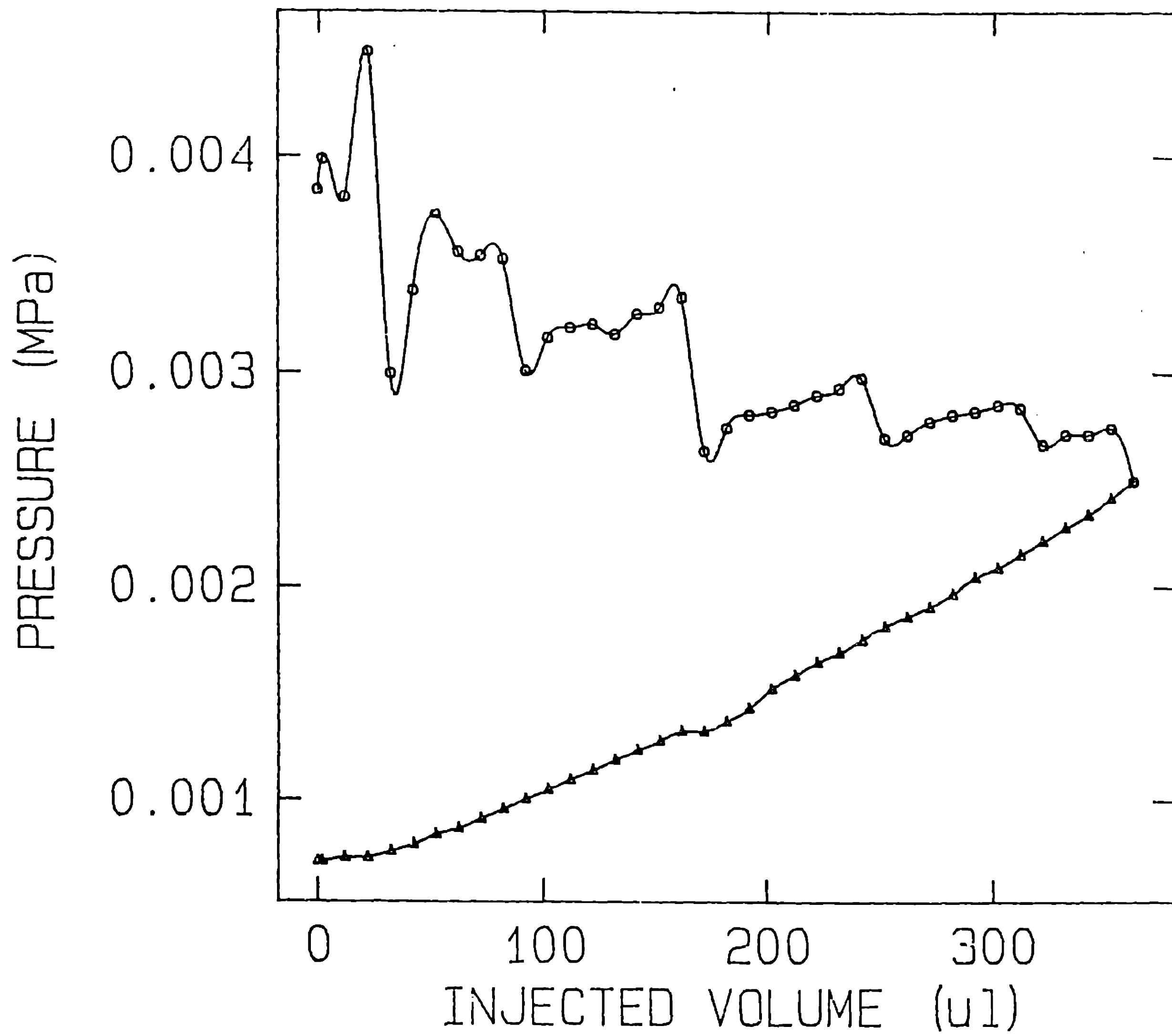


Figure 39: Peel data for the first sample

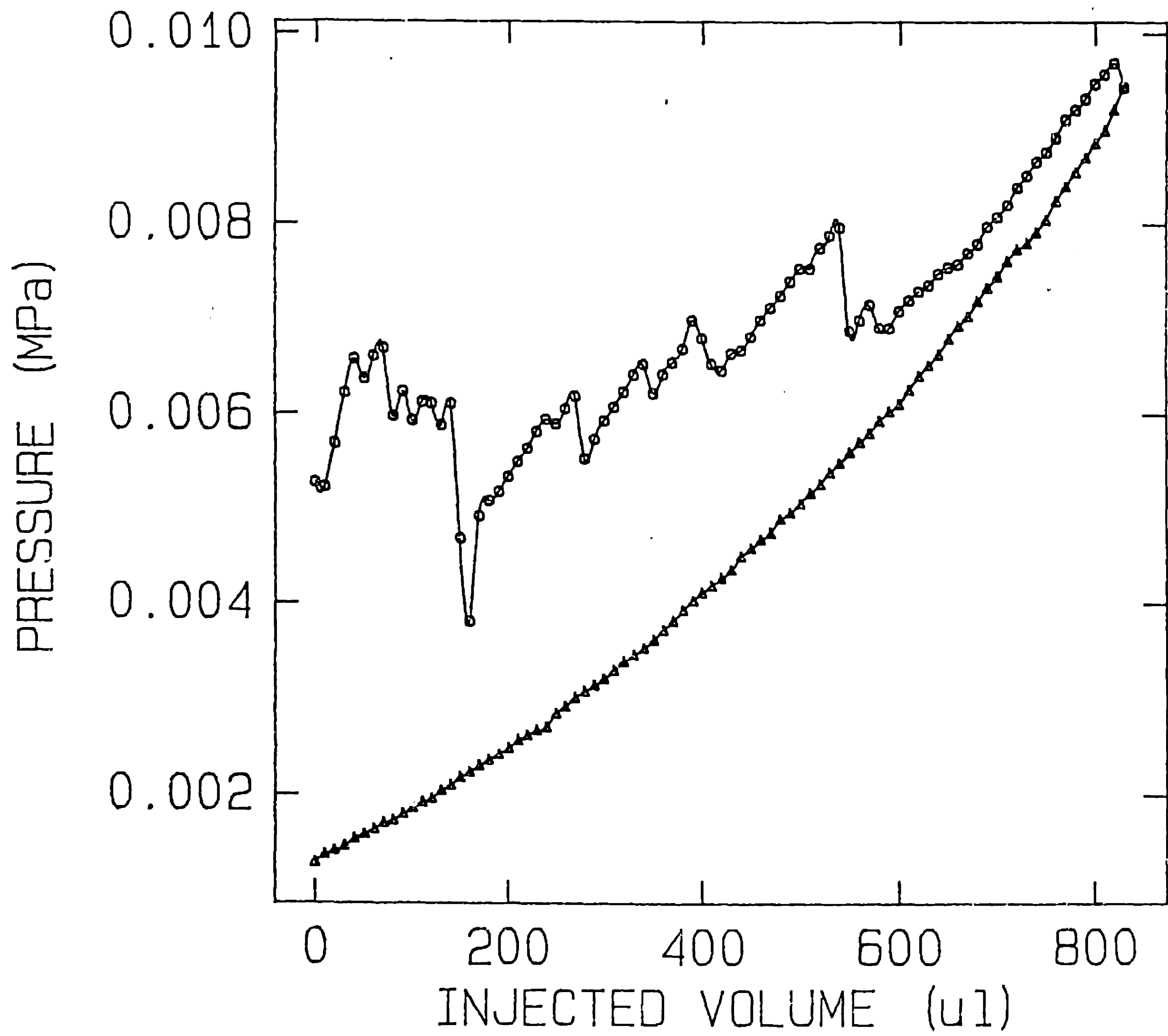


Figure 40: Peel data for the second sample

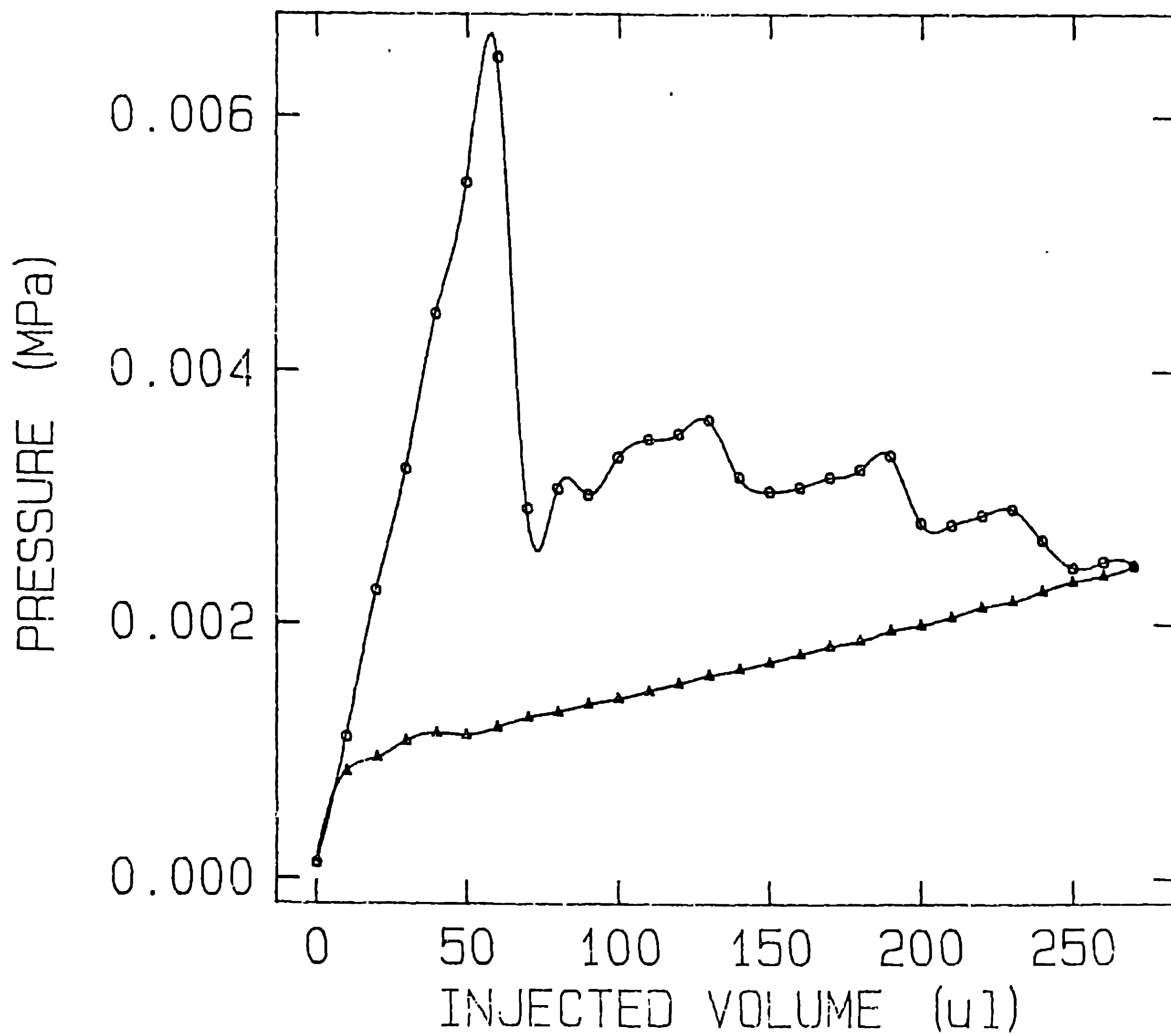


Figure 41: Apparent re-adherence after peel

# 5 Released Structures

This chapter introduces mechanical microstructures for studying thin films under tensile stress. The process, structures, and the requisite analysis have been developed to determine the ratio of residual stress to Young's Modulus and elongation at break of films, such as polyimide, which are typically under residual tensile stress. In addition, structures can be designed which are sensitive to the Poisson's ratio of the film and the value can be measured.

Guckel [122] has previously reported the use of buckling behavior of fixed-end polysilicon beams to study strain in films with compressive stress. In this work on tensile stress, structures are fabricated on (100) silicon as described in section 3.6 and appendix G. In brief, the structures are fabricated by anisotropically etching thin silicon diaphragms of desired size for initial support, depositing the film of interest (in this case polyimide), patterning the film over the diaphragm, and etching away the diaphragm, which releases the structure and allows relaxation due to residual stress. For this study, BTDA-ODA/MPDA polyimide is spin-coated on a silicon substrate in multiple coats (prebaked at 135°C for 14 minutes after each coat and cured at 400°C for 45 minutes).

The concept is to fabricate a structure with a geometry sensitive to the films residual tensile stress. When the silicon support is removed, and the structure is released (free to deform such that its total potential energy can be reduced), the deformation is a predictable function of the films mechanical properties, including the intrinsic stress, Young's Modulus, and Poisson's ratio. Figure 42 shows a few of the structures that were fabricated in this work before release and after release.

In figure 42.A, the square polyimide plate in the center rotates after release because of the stress-induced shrinkage of the four arms, acting as two pairs of couples. In figure 42.B, the fixed-end polyimide beam deflects due to stress-induced shrinkage of the five arms, creating a uniform load over parts of the beam. In Figure 42.C, the square plate held by four legs deflects due to the stress-induced shrinkage of the long center arm, pulling on the plate. Figure 42.D shows a fixed-end polyimide *beam* with an abrupt width-change at a selected point along the axis of the beam. Upon release of the structure, the width-change boundary is displaced due to force imbalance in the structure. The wide portion shrinks, stretching the thinner members, until force balance is achieved. Figure 42.E shows a *T-shape* fixed

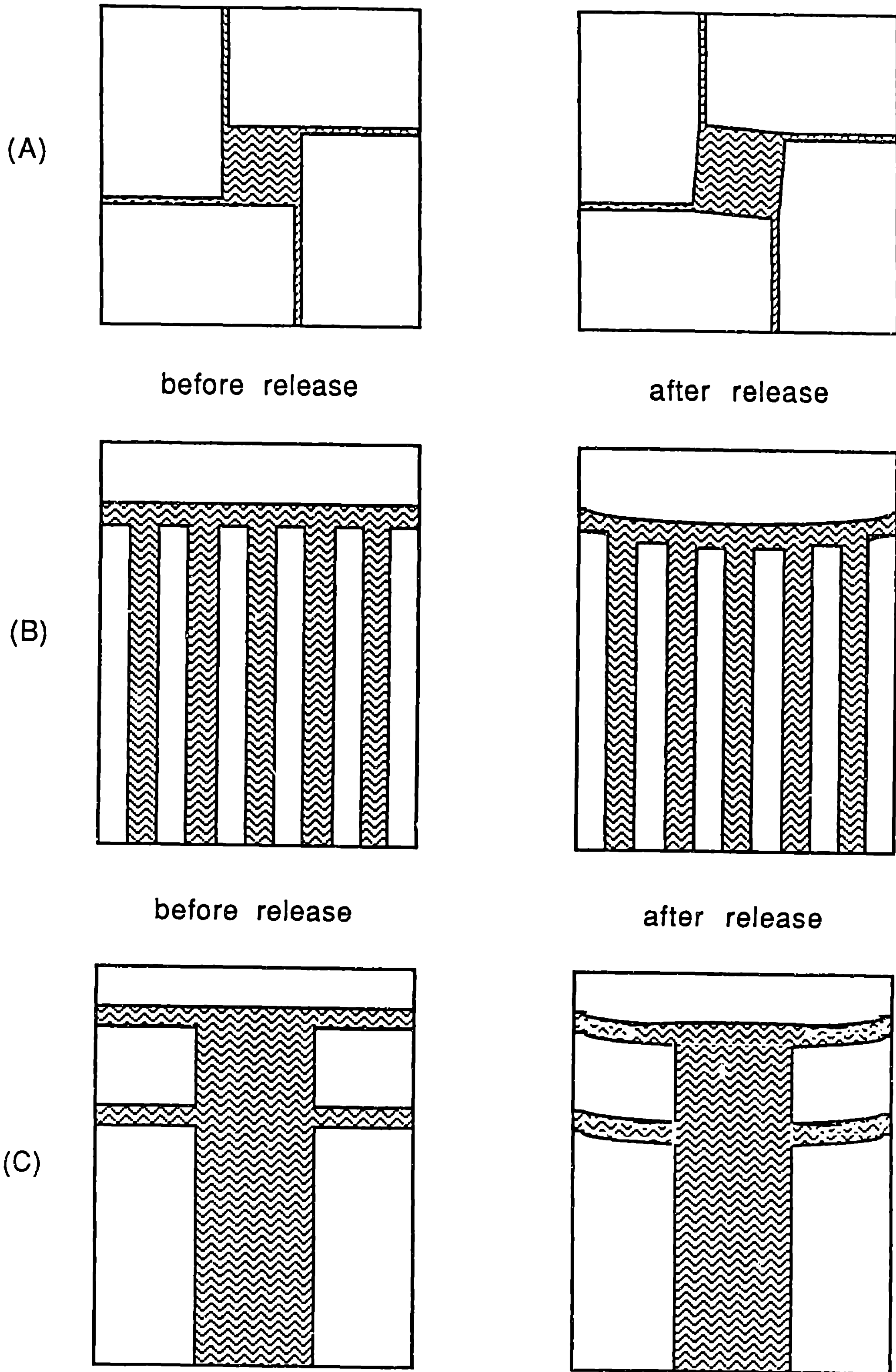


Figure 42: Various structures before and after release

(D)

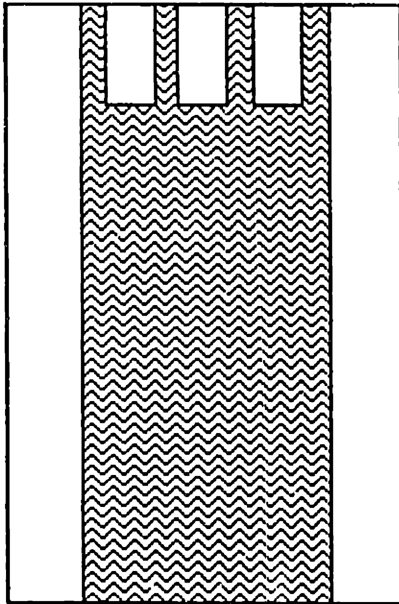

before release

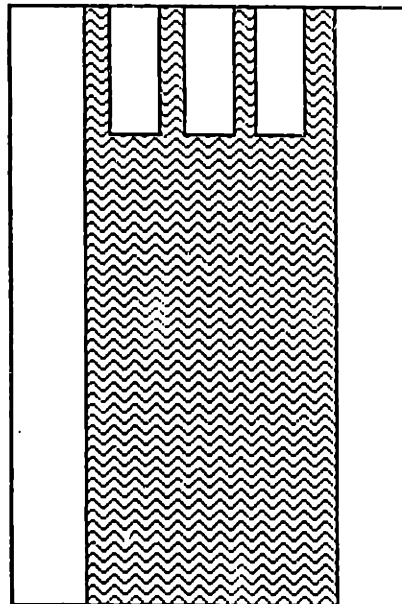

after release

(E)

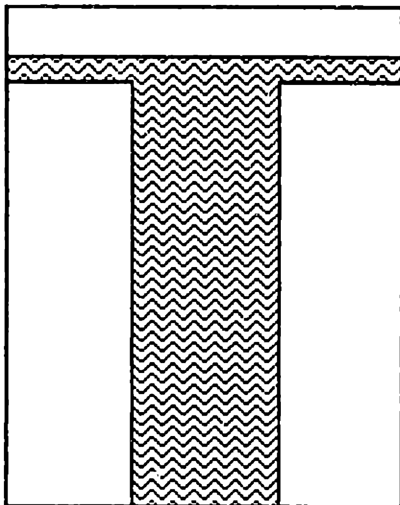

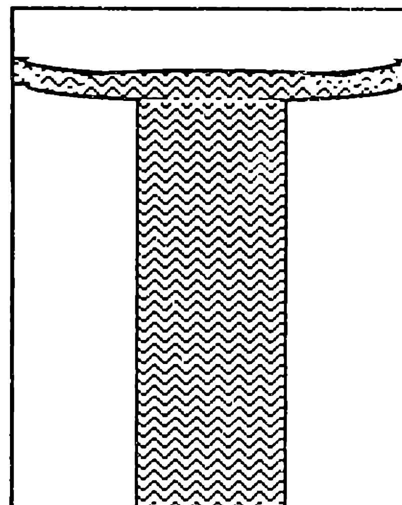

Figure 42: Various structures before and after release

at all three ends. When the structure is released, the cross-bar of the T deflects due to the stress-induced shrinkage of the center leg.

Even though, the first three structures described in figure 42 demonstrate the concept of "released structures" and the role of the residual stress of the film in final deformations, they are not the optimum structures for actual measurements. Figure 43 and 44 are SEM photographs of the actual fabricated structure of figure 42.A. In the magnified view, figure 44, the slight warpage of the arms near the square plate is evident which would render a simple torque equilibrium analysis on the plate doubtful. Figure 45 is a SEM photograph of the actual fabricated structure of figure 42.B. The center deflection of the beam, 2 mm in length, is 50 microns. It is difficult to analyze this structure because of the complexity of the type of loading. There are five uniformly loaded regions, each having a different uniform load because of the different degree of shrinkage in each arm. The middle arm is no longer in tension and is buckled. Figure 46 is a SEM photograph of the actual fabricated structure of figure 42.C. Again, due to structural design, the analysis of the forces in this structure is far more complicated than other structures, discussed below, that give measurements of the mechanical properties of interest.

The last two structures in figure 42 are simple and sufficient for studying all the mechanical properties of interest. These structures referred to as beams and T shapes will be discussed in detail in the next few sections. In section 5.3, released polyimide cantilever beams will be discussed. The last section is an overview of this chapter.

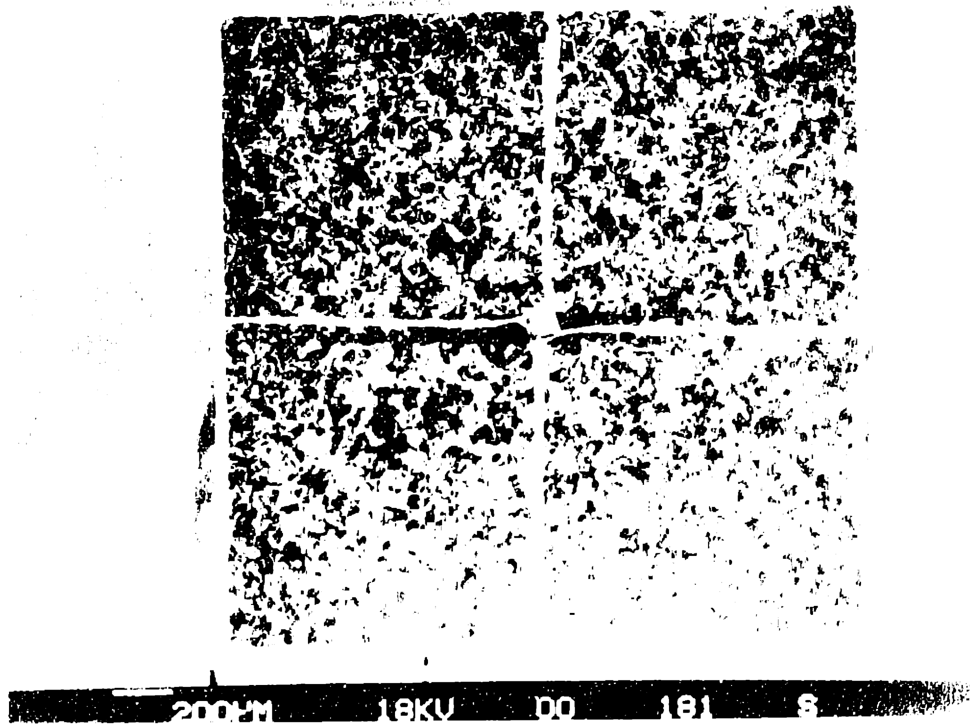


Figure 43: Released 8.0 micron thick couple-loaded polyimide plate

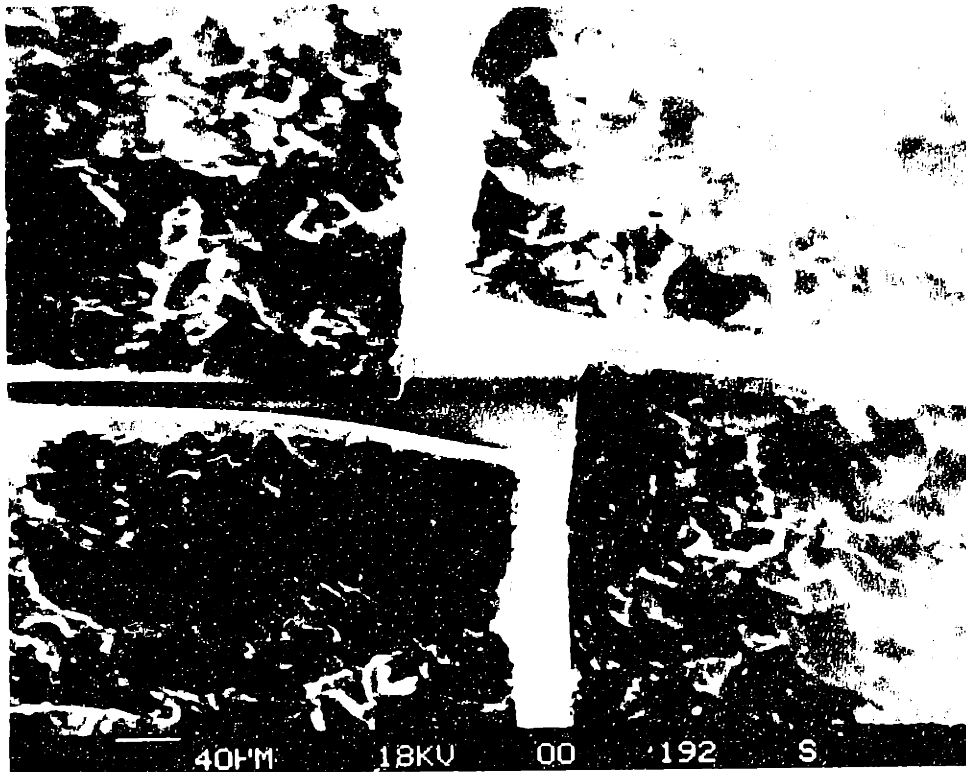


Figure 44: Magnified view of the rotated plate

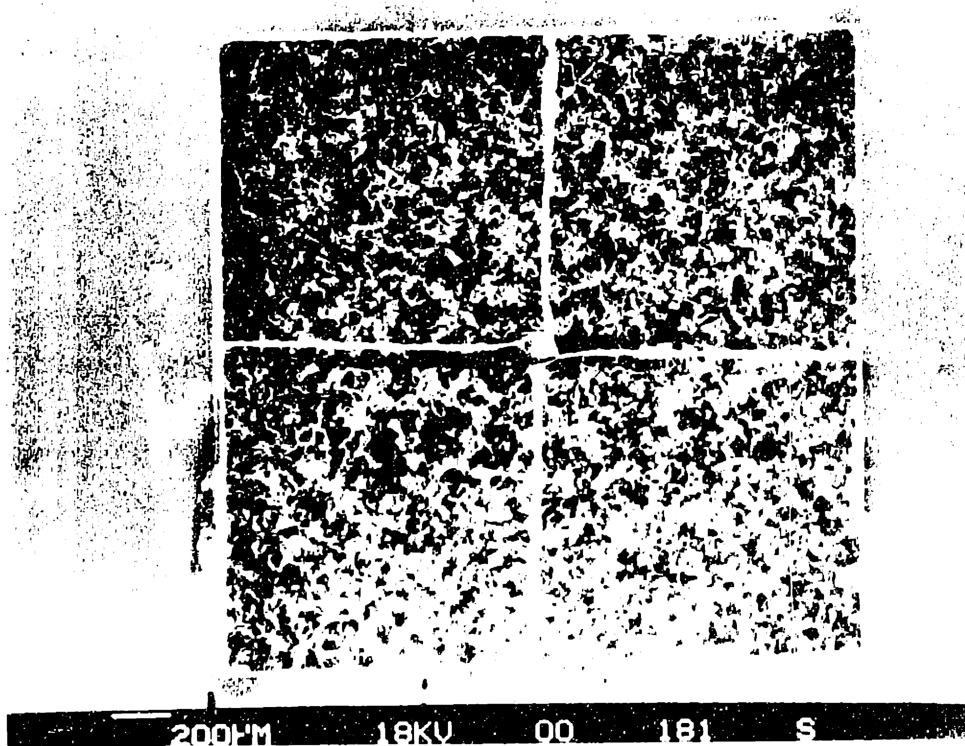


Figure 43: Released 8.0 micron thick couple-loaded polyimide plate

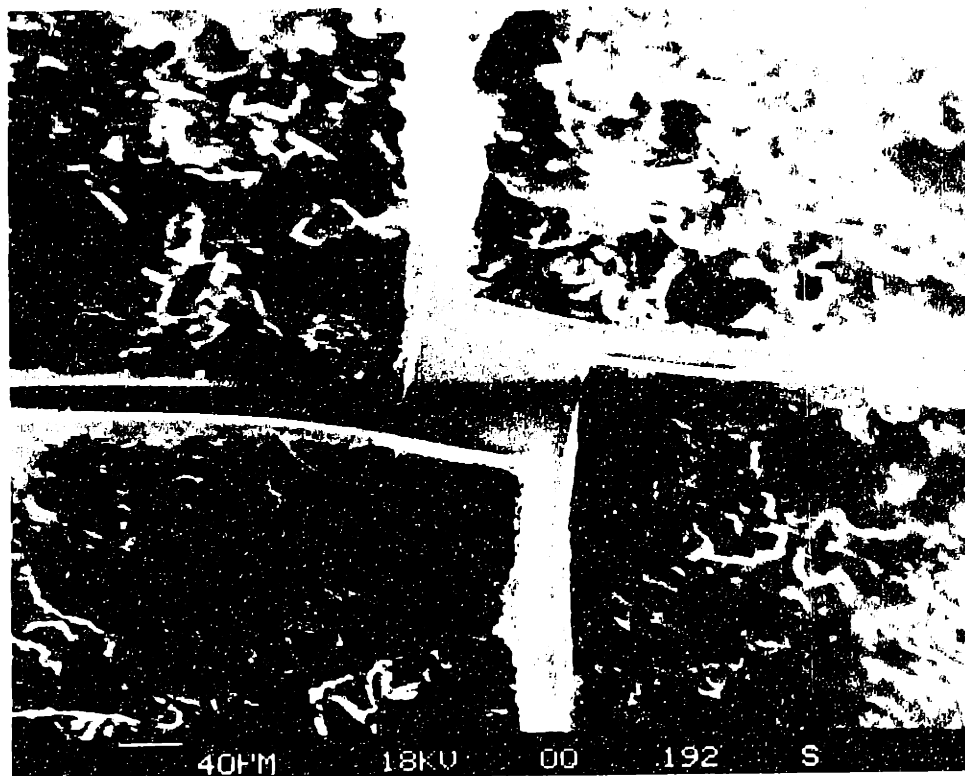


Figure 44: Magnified view of the rotated plate



INTENTIONAL DUPLICATE EXPOSURE

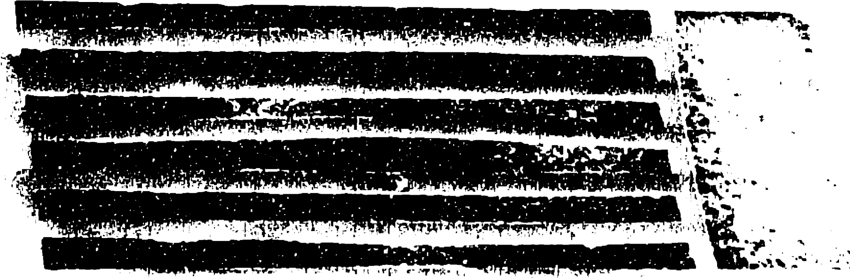

Figure 45: Released 8.0 micron thick transverse loaded polyimide beam

Figure 46: Released 8.0 micron thick supported plate structure

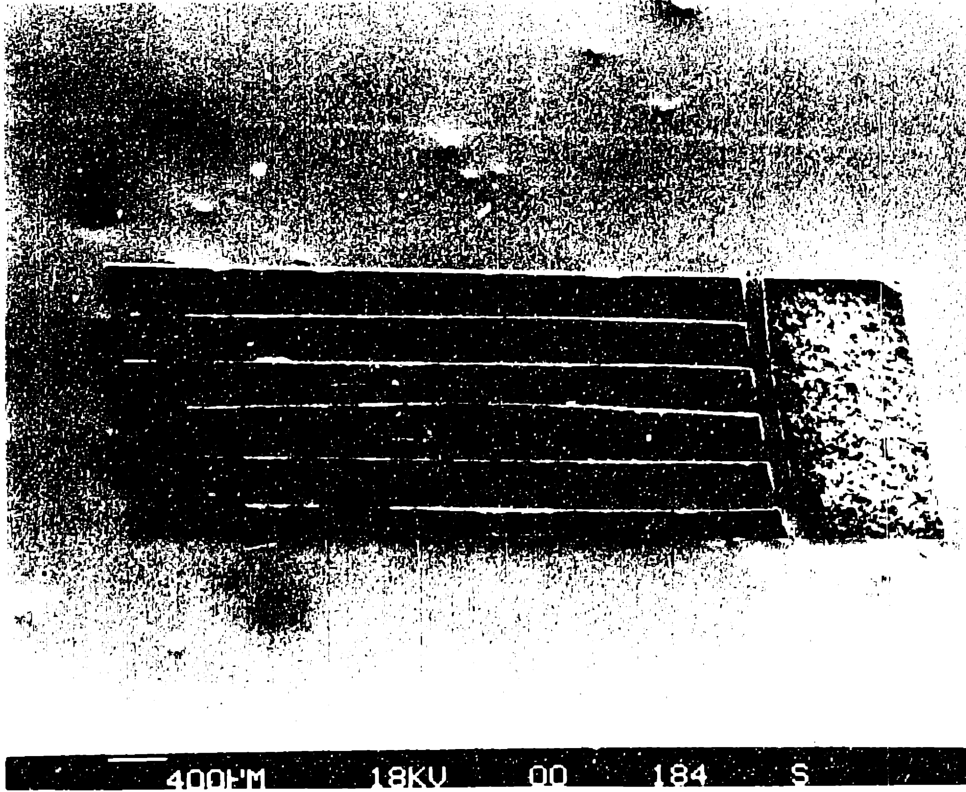


Figure 45: Released 8.0 micron thick transverse loaded polyimide beam

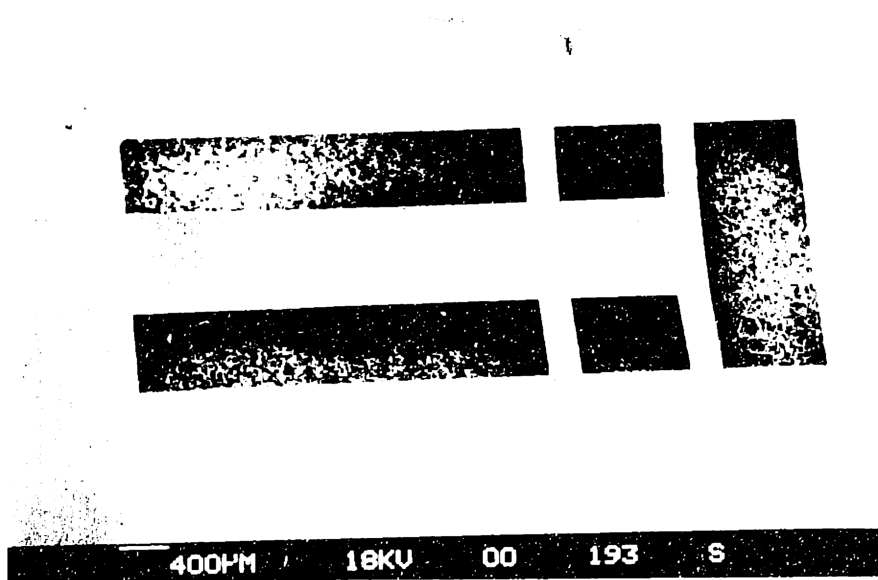


Figure 46: Released 8.0 micron thick supported plate structure



INTENTIONAL DUPLICATE EXPOSURE

## 5.1 T-shape Polyimide Structures

These structure are particularly useful in measuring the ratio of residual stress to modulus. Large deflections are observed without creating large strains in the film. This guarantees that the film is in its linearly elastic domain. If the dimensions of the structure are selected appropriately, the Poisson's ratio for the film can be extracted.

In the discussion to follow, a simple analysis of the structure is performed by making appropriate assumptions, which are verified later. Figure 47 describes the parameters. This structure is modeled as a fixed-end polyimide beam, uniformly loaded in the center region by the center leg. The stress-induced shrinkage of this center leg creates the uniform load on the beam. To analyze this indeterminate structure, the force per unit length on the boundary, q, is found in terms of the center deflection, $\delta$, when the structure is released.

The dimensions of the structure can be appropriately selected such that the deflections of the polyimide beam, $\delta$, is always less than 30% of the beam width, $h$. In this case, the beam deflections can be found by small deflection theory and the membrane stresses created as a result of the stretching of middle plane of the beam can be neglected [116]. In this derivation, the effect of the residual tensile stress in the beam is neglected. It is shown later in this section that both these assumptions are reasonable.

The center deflection of a fixed-end beam under uniform load over a region in the center can be found by superposition of the deflections due to bending and shear as:

$$\delta = \delta_b + \delta_s, \tag{30}$$

where $\delta$ is the total deflection and $\delta_b$ and $\delta_s$ are the contributions from bending and shear, respectively. The deflection at the center due to bending, $\delta_b$, is given [123] by:

$$\delta_b = \frac{qW}{192EI}(L^3 - W^2L + \frac{W^3}{2}), \tag{31}$$

where

$$I = \frac{bh^3}{12}, \tag{32}$$

L is the length of the beam, b is the film thickness, and E is Young's Modulus.

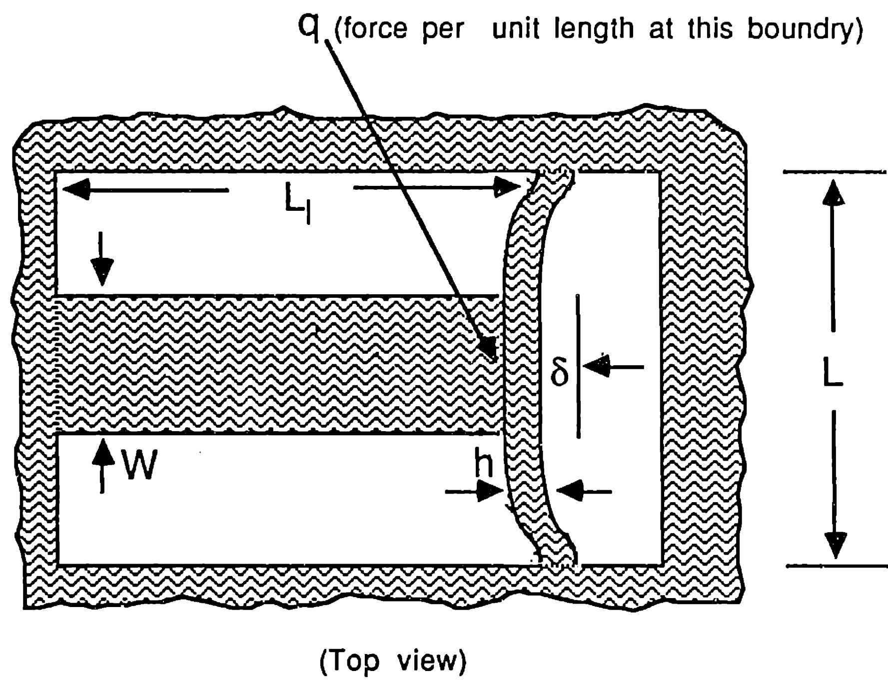


Figure 47: Parameter description for the T structure

The component of the deflection due to shear, $\delta_s$, is given by [124]:

$$\delta_s = \frac{\alpha_s q W}{4GA}(L - \frac{W}{2}), \tag{33}$$

where

$$A = bh, \tag{34}$$

$\alpha_s$ is the shear coefficient (which is equal to 1.5 for a beam with rectangular cross-section [124]), and G is the modulus of elasticity in shear. The total deflection is

$$\delta = \delta_b + \delta_s = q[\frac{W}{192EI}(L^3 - W^2 L + \frac{W^3}{2}) + \frac{\alpha_s W}{4GA}(L - \frac{W}{2})]. \tag{35}$$

Note that shear forces aid deflection.

However, $q$, is the load that is generated by stress-induced shrinkage of the center leg and is given as:

$$q = bE(\frac{N_0}{E} - \frac{\delta}{L_l}), \tag{36}$$

where $N_0$ is the residual tensile stress, $L_l$ is the length of the center leg. In truth, this parameter is

$$L_{l0} = \frac{L_l}{1 + \frac{N_0}{E}}, \tag{37}$$

where $L_{l0}$ is the length of the stress free leg. However, this correction is of second order and is neglected here. In finding q, the center leg stress-induced shrinkage is modeled as uniform across the width, W. In reality, due to the curvature in the beam, this is not the case. However, the length of the center leg is very large compared to the variation in shrinkage across the width and justifies the assumption. By substituting equation (36) into equation (35), the ratio of the stress to the modulus is related to the deflection, $\delta$, the dimensional parameters, and Poisson's ratio as:

$$\delta = (\frac{N_0}{E} - \frac{\delta}{L_l})[\frac{W}{16h^3}(L^3 - W^2 L + \frac{W^3}{2}) + \frac{3W(1-\nu)}{4h}(L - \frac{W}{2})]. \tag{38}$$

Note that the first term in the bracket in equation (38) is the contribution due to bending moment while the second term is the contribution due to shear. The bending term is approximately proportional to cubic ratio of the beam length to the beam width while the shear term is proportional to the first power of the same ratio.

If the fixed-end beam is made slender (large ratio of the beam length, L to the beam width, $h$) the contribution of the shear component is negligible. This contribution is large for stocky beams. For a ratio of length to width of the beam larger than 10, the shear component is less than 10%. In this case, the shear contribution is neglected to simplify equation (38) to:

$$\frac{N_0}{E} = \delta\left[\frac{1}{L_l} + \frac{16}{W\left(\frac{L^3}{h^3} - \frac{W^2L}{h^3} + \frac{W^3}{2h^3}\right)}\right]. \tag{39}$$

By fabricating a structure of appropriate dimensions over a silicon diaphragm and then removing the diaphragm to release the structure, the deflection $\delta$ can be measured. Using equation (39), the ratio of the stress to the modulus can be calculated. In addition, if several beams with small ratios of length to width are fabricated on the same sample, equation (38) can be used to fit the data and extract the values of $\frac{N_0}{E}$ and $\nu$ that best fit.

Two wafers were processed with BTDA-MDA/ODA polyimide of thicknesses 5.5 and 8.0 microns. Each wafer had several T structures with either slender or stocky beams. Figure 48 shows a SEM photograph of a typical T structure. Figure 49 shows a magnified view of the beam section, demonstrating the deflection (the white line is put in as a reference). The deflections are measured with $\pm 3$ microns accuracy using an optical microscope. For the slender beam structures (ratio of the length to width of the beam above 10), equation (39) was used to find the stress to modulus ratio. All the fabricated structures have a beam length, L, of 2048 microns. Table III presents the data, including the critical dimensions, for the wafer with 5.5 micron thick film. The ratio of the stress to the modulus is $0.011 \pm 0.002$. It is evident from equation (39) that the error in measuring $\delta$ creates the uncertainty in the calculated stress to modulus ratio. In this work, the error in measuring the deflection, $\delta$, is at least 10% (increasing for smaller deflections). This large measurement error translates into the error on the calculated stress to modulus ratio. The reason for the large measurement error is that measurements had to be taken at low magnification to be able to see the entire fixed-end beam portion in the field of view of the microscope. At higher magnification where the accuracy of the measurement increases, the entire beam is not in the field of view to provide a reference for measuring the deflection.

Table IV presents data on five stocky beams (length to width ratio below 10) made on the wafer with 5.5 micron thick film. If the data is fit to equation (38), the

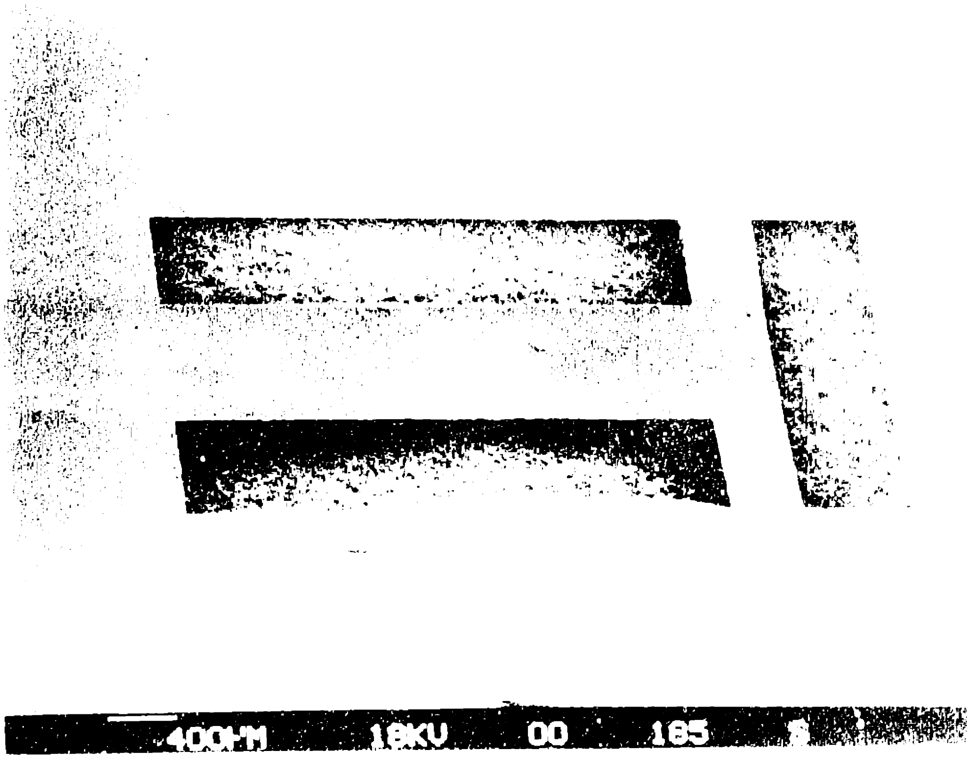


Figure 18 [illegible]

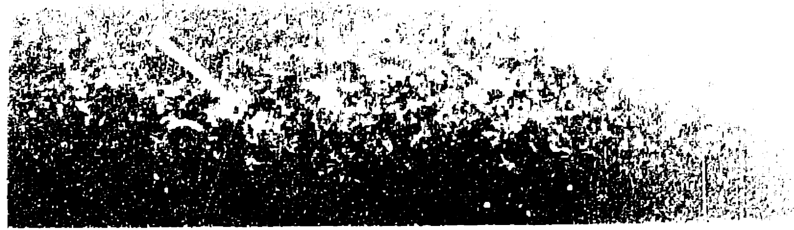

Figure 19. Magnified [illegible]

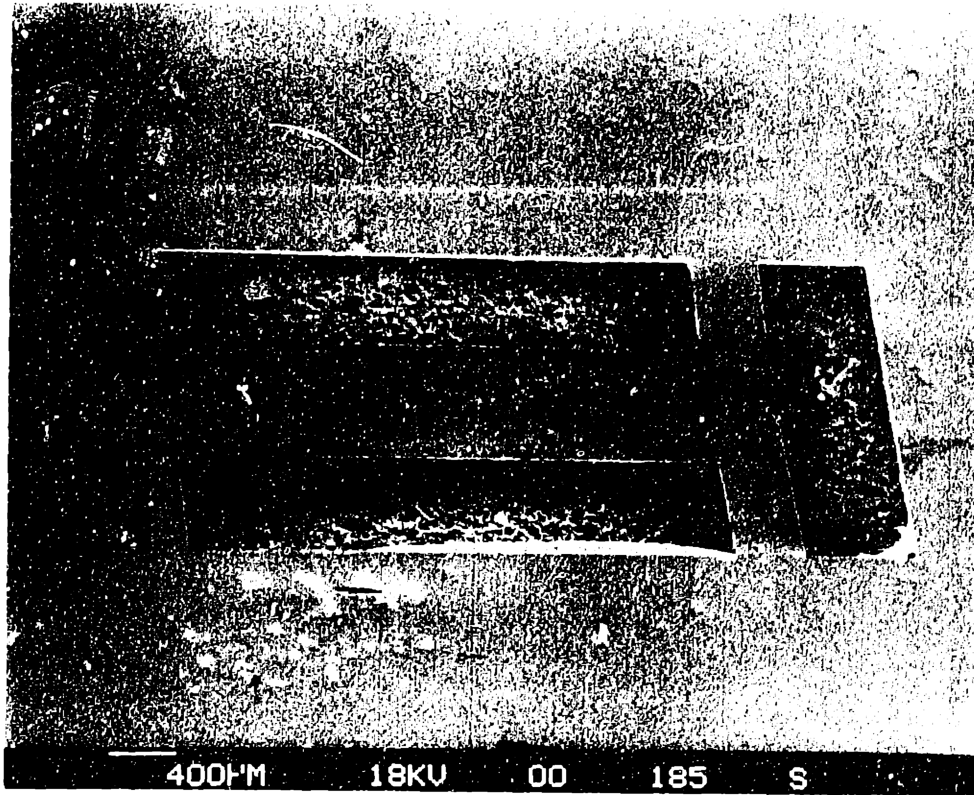


Figure 48: SEM of a released 5.5 micron thick T structure

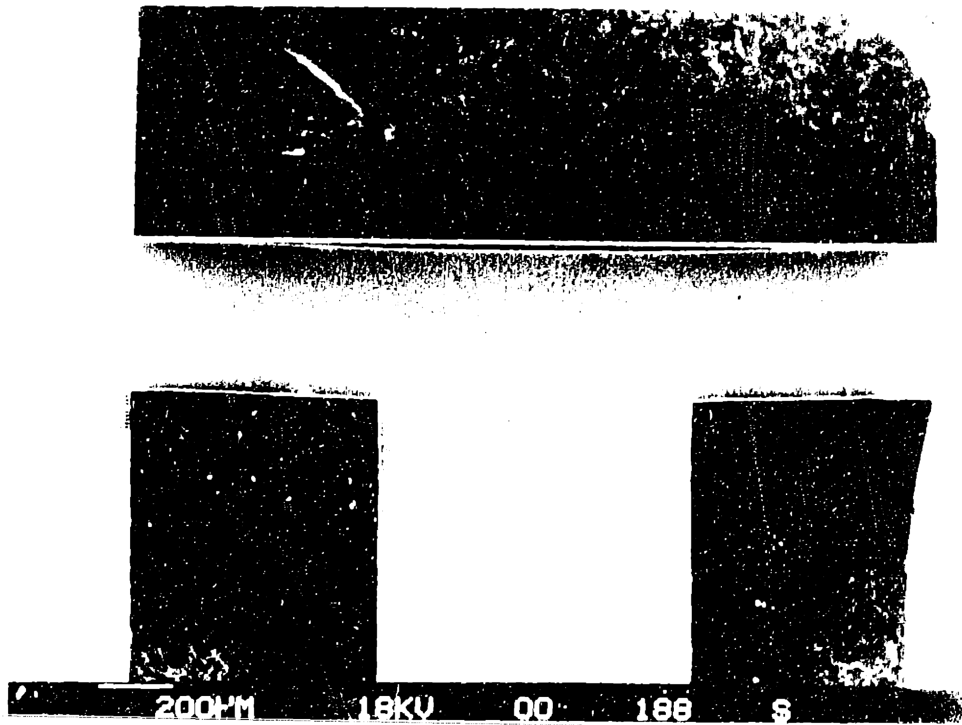


Figure 49: Magnified view of the cross-bar region



INTENTIONAL DUPLICATE EXPOSURE

| # | W (μ) | h (μ) | $L_l$ (μ) | δ (μ) | $\frac{N_o}{E}$ |
|---|---|---|---|---|---|
| 1 | 800 | 133 | 3027 | 35.0 | 0.0118 |
| 2 | 800 | 133 | 4027 | 42.5 | 0.0108 |
| 3 | 800 | 133 | 4027 | 40.5 | 0.0102 |
| 4 | 800 | 166 | 4027 | 37.0 | 0.0097 |
| 5 | 500 | 166 | 3027 | 30.0 | 0.0104 |
| 6 | 500 | 166 | 3027 | 33.0 | 0.0116 |
| 7 | 500 | 209 | 3027 | 30.0 | 0.0110 |

Table III: Data on slender-beam T structures

| # | W (μ) | h (μ) | $L_l$ (μ) | δ (μ) | ν | $\frac{N_o}{E}$ |
|---|---|---|---|---|---|---|
| 1 | 800 | 237 | 3027 | 32.0 | 0.1 | 0.0118 |
| 2 | 800 | 385 | 3027 | 26.0 | 0.2 | 0.0118 |
| 3 | 800 | 385 | 3027 | 27.0 | 0.3 | 0.0119 |
| 4 | 500 | 295 | 3027 | 28.0 | 0.4 | 0.0120 |
| 5 | 500 | 490 | 3027 | 21.0 | 0.5 | 0.0121 |

Table IV: Data on stocky-beam T stuructures

extracted value for the stress to modulus ratio is 0.013, in agreement with the result above. However, the extracted value for Poisson's ratio, $\nu = -0.72$, has no physical meaning. This is also due to the large uncertainty in measuring the deflection, $\delta$. To show this point, consider the last sample in table IV. Assume that the true value for the stress to modulus and the Poisson's ratio are

$$\frac{N_0}{E} = 0.01 \tag{40}$$

and

$$\nu = 0.25. \tag{41}$$

For the dimensions particular to this structure, the true deflection, $\delta$, would be 15.5 microns. With an uncertainty of $\pm 3$ microns in measurements, the measured deflection would range from 12.5 to 18.5 microns. Assuming that the stress to modulus ratio was known to be 0.01, the calculated Poisson's ratio would then range from +1.0 to -0.9. However, under the same conditions, if the measurement uncertainty could be reduced to $\pm 0.5$ microns, the calculated Poisson's ratio would only range from 0.4 to 0.1.

To further demonstrate that the inability to extract $\nu$ from the data presented here is caused by the large measurement error, the last two columns of table IV show the extracted values of stress to modulus ratio for the structures of this table when a value for $\nu$ is assumed. The stress to modulus values are found by finding the best fit value through a least squares procedure. It is evident that the extracted stress to modulus ratio is in good agreement with the result found above for the slender beams, independent of the value chosen for $\nu$.

Note that as the length to width ratio for the beam is decreased to enhance the shear contributions, the percent uncertainty in the deflection measurements increase since the deflections decrease. One way to improve the deflection measurement is to put a straight strip of the polyimide close to the front of the beam as shown in figure 50. This allows for going to high optical magnification since it is no longer necessary to have the whole beam in the field of view. However, it is unlikely that measurements with better than $\pm 1$ micron accuracy can be performed using an optical set up. A potential method is the use of diffractometry through the slit created by the strip and the deflected beam. This would improve the accuracy in measuring the deflection to fractions of a micron.

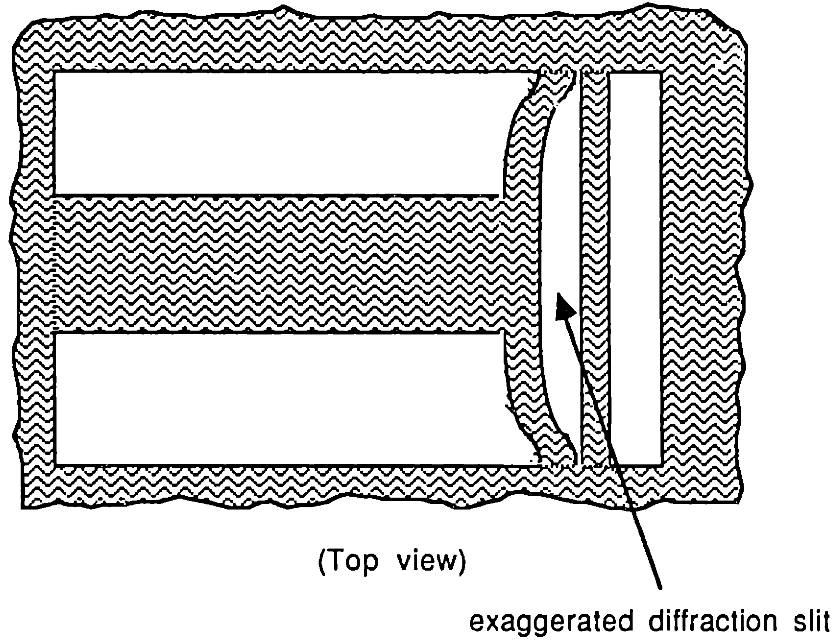


Figure 50: Improved structure for more accurate deflection measurement

Another approach may be the use of other structures that are more sensitive to shear forces. An extension of the idea of stocky beams in the T structures was fabricated and is shown in figure 51. The wide middle-plate is loaded due to the stress-induced shrinkage of the two thinner arms. The structure as fabricated here, is not very stable (out of plane warpage occurs at the free edges). The edges can be held by smaller arms to avoid this problem. No data was taken on these samples during this initial course of work.

In the derivation of equation (38), the effect of the residual tensile stress in the beam is neglected. In addition, the contribution of the membrane stresses due to the stretching of the middle plane of the beam in stiffening the beam is neglected as long as the deflections are below 30% of the beam width. To show the validity of these assumptions, these effects have to be incorporated in the formalism of finding the deflection. For a uniformly loaded beam as considered here, an accurate formalism of this sort is complicated. Since these effects are not significant for stocky beams where deflections are small, the discussion from this point on focuses on deflections due to bending. The deflection shape of such a beam in the region of loading is of the form

$$w(x) = Ax^2 + Bx^3 + C(x - d)^4, \tag{42}$$

where

$$d = \frac{L - W}{2}, \tag{43}$$

A, B, and C are constants, $x$ is the coordinate along the beam, $w$ is the deflection, and the origin is on the left side of the beam. Even an energy method approach for analyzing the problem is complicated by this form of solution. The beam deflection analysis, using the energy method [116] is simplified assuming a deflection shape for the left half of the beam as:

$$w(x) = w_0(3lx^2 - 2x^3), \tag{44}$$

where $l$ is half length of the beam and the deflection at the center of the beam is $\delta = w_0 l^3$. This deflection form satisfys the boundary conditions and is of the correct form for the portion of the beam that is not loaded. As a side point, this is the exact deflection form for the same beam loaded at the center by a concentrated load.

The elastic strain energy in the beam is [116]

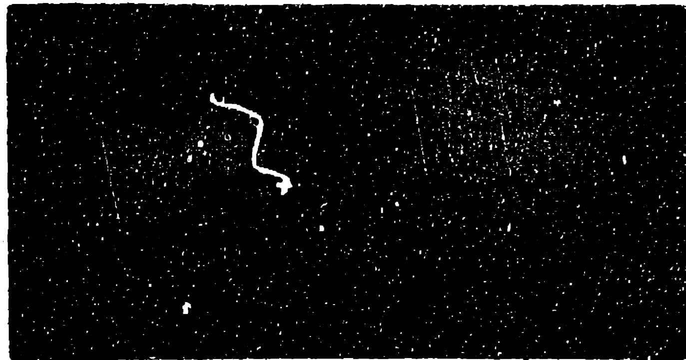

Figure 51: A shear sensitive structure for measurements of Poisson's ratio

$$U = \frac{l}{EA}F_x^2 + \frac{EI}{2}\int_0^L (\frac{\partial^2 w}{\partial x^2})^2 dx, \tag{45}$$

where

$$F_x = EA\varepsilon_x, \tag{46}$$

A=bh is the cross-sectional area of the beam, b is the thickness of the film, and $\varepsilon_x$ is the strain in the $x$ direction. The strain in the $x$ direction has two components: the initial strain due to the tensile residual stress of the film and the tensile strain created from the stretching of the middle plane of the beam due to bending. The first component is just the ratio of the residual stress to the modulus. The second component is calculated as:

$$\varepsilon = \frac{1}{L}\int_0^L (ds - dx) = \frac{1}{L}\int_0^L [[1 + (\frac{dw}{dx})^2]^{\frac{1}{2}} - 1]\, dx. \tag{47}$$

Assuming that

$$1 >> (\frac{dw}{dy})^2, \tag{48}$$

equation (47) can be simplified to

$$\varepsilon = \frac{1}{L}\int_0^L \frac{1}{2}(\frac{dw}{dx})^2 dx. \tag{49}$$

This equation can be integrated by taking the derivative of equation (44) and performing the integration. The resulting strain is

$$\varepsilon = \frac{3}{5}w_0^2 l^4. \tag{50}$$

Adding the two components of the strain, the total strain in the $x$ direction is

$$\varepsilon_x = \frac{N_0}{E} + \frac{3}{5}w_0^2 l^4. \tag{51}$$

The total strain energy of the bar is then find to be

$$U = lbhE[\frac{9}{25}w_0^4 l^8 + (\frac{N_0}{E})^2 + \frac{6}{5}w_0^2 l^4 \frac{N_0}{E}] + bh^3 E w_0^2 l^3. \tag{52}$$

The work, $W_0$, done in deflecting the beam can be found as:

$$W_0 = 2bE(\frac{N_0}{E} - \frac{\delta}{L_l})\int_d^l w_0(3lx^2 - 2x^3)dx. \tag{53}$$

Since at equilibrium the potential energy of the system is minimized, the deflection $\delta = w_0 l^3$ can be found by imposing the condition

$$\frac{dU}{dw_0} = \frac{dW_0}{dw_0}. \tag{54}$$

The resulting relationship for the deflection as a function of the stress to modulus ratio is

$$h[\frac{36}{25}\delta^3 + (\frac{12}{5}\frac{N_0}{E}l^2 + 2h^2)\delta] = (\frac{N_0}{E} - \frac{\delta}{L_l})(l^4 - 2ld^3 + d^4). \tag{55}$$

The first term on the left accounts for the contribution of membrane stress due to the stretching of the middle plane of the beam. The magnitude of this term is less than 5% of the magnitude of the sum of the other two terms for deflections as large as 30% of the beam width, $h$. Therefore for the structures fabricated in this work, this term can be neglected. By neglecting this term, equation (55) can be simplified to:

$$(2h^3 + \frac{l^4 - 2ld^3 + d^4}{L_l})\delta = \frac{N_0}{E}(l^4 - 2ld^3 + d^4 - \frac{12}{5}l^2h\delta), \tag{56}$$

where the last term on the right represents the contribution of the residual tensile stress to stiffening of the beam. This term can be neglected as compared to the first term on the right since $l^2 >> h\delta$.

In summary, structures for studying the stress to modulus ratio and the Poisson's ratio have been introduced. A simple analysis has been carried out to extract the values of interest from the experimental data. It is shown that for extraction of Poisson's ratio, the deflection measurements have to be accurate to fractions of a micron. Laser diffractometry is suggested for such accurate measurements. The values of the stress to modulus ratio are in good agreement with the measurements in the previous chapter by load-deflection studies on polyimide diaphragms.

## 5.2 Fixed-end Polyimide Beams

These structures are particularly useful in studying the ratio of the intrinsic stress in the film to the modulus, the yields strain, and the ultimate strain at break. The analysis is simple and demonstrates how the the above parameters can be measured. Figure 52 describes the parameters. Since the whole structure is made of the same material with uniform thickness, b, the depth dimension is incorporated here by introducing forces per unit length. This automatically assumes that the stresses are uniform across the thickness of the film (will be discussed in the next section).

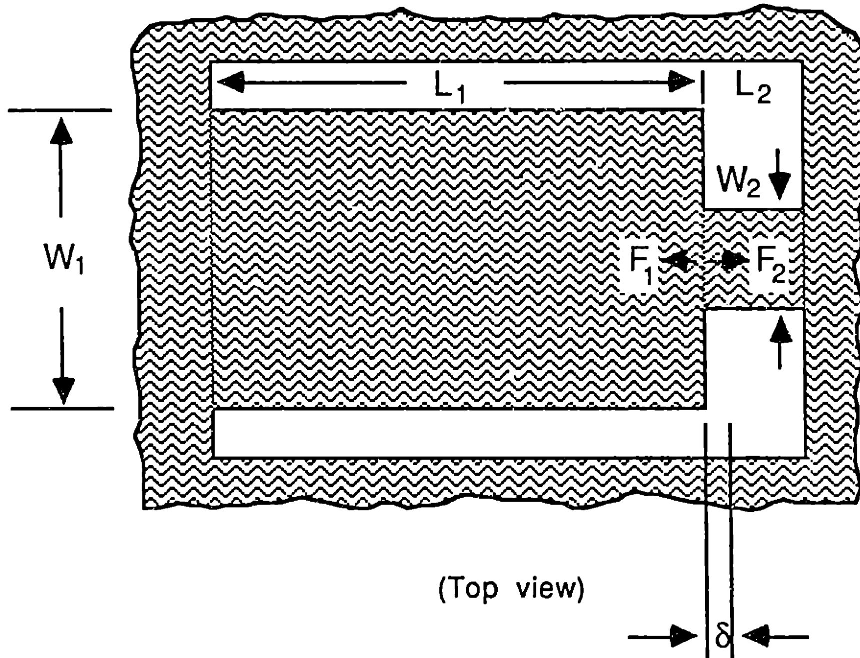


Figure 52: Parameter description for the fixed-end beam

All the parameters of the wide member are denoted with subscript 1 while the parameters of the thin members are denoted with subscript 2.

This indeterminate structure is analyzed by assuming a displacement, $\delta$, after the structure is released. Then, the force, $F_1$, acting on the boundary by the stress-induced shrinkage of the wide member is

$$F_1 = EW_1(\frac{N_0}{E} - \frac{\delta}{L_1}), \tag{57}$$

where E is the Young's modulus, $N_0$ is the residual stress in the film, $L_1$ is the initial length of the wide member, and $W_1$ is the width of the wide member. The force, $F_2$, acting on the boundary because of the stretching of thin members due to the shrinkage of the wide member is

$$F_2 = EW_2(\frac{N_0}{E} + \frac{\delta}{L_2}), \tag{58}$$

where $L_2$ and $W_2$ are the length and width of the thin member. At equilibrium the two forces are equal. Setting equations (57) and (58) equal, the result is

$$\frac{N_0}{E} = \delta(\frac{\frac{W_1}{L_1} + \frac{W_2}{L_2}}{W_1 - W_2}). \tag{59}$$

For actual fabrication, the thin member is split into two or four thinner members placed at equal distances across the width of the boundary (figure 42.d ). This avoids the out of plane curling of the edges, that otherwise would be unsupported, and greatly improves the stability of the structure. However, the above analysis still applies as long as $W_2$ is taken to be the total width of the thinner members.

In the above analysis, $L_1$ and $L_2$ are the lengths of the members before releasing the structure. In truth, these should be the length of the members, $L_{01}$ and $L_{02}$, when the members are stress-free. For example, the relationship between $L_1$ and $L_{01}$ is

$$L_{01} = \frac{L_1}{1 + \frac{N_0}{E}}. \tag{60}$$

However, this correction is of second order and is neglected here.

Equation (59) shows that by measuring the displacement, $\delta$, after the structure is released, the ratio of the stress to modulus can be determined. It is also clear that the strain in the thin arms, $\varepsilon_2$ is

$$\varepsilon_2 = \frac{N_0}{E} + \frac{\delta}{L_{02}} = \frac{N_0}{E}(1 + \frac{\delta}{L_2}) + \frac{\delta}{L_2}. \tag{61}$$

By appropriate selection of dimensions, the $\varepsilon_2$ can range from nearly zero to the ultimate strain at break. In this way, the beams can function like a tensile testing machine. The modulus can be studied as a function of strain since the residual stress is constant, to find the yield strain for the film. Coupled with the stress measurements from the load-deflection studies on polyimide membranes, the stress-strain curve can be determined.

Two wafers were processed, with polyimide film thickness of 5.5 microns for the first sample and 8.5 microns for the second. Beams with various dimensions were fabricated on each sample. On the wafer with the thinner film, when the strain, $\varepsilon_2$, exceeded 4.5%, the members completely failed (the approximate ultimate strain was measured to be 4% when the polyimide membranes failed in the previous chapter). The induced strain range was limited to above 3.5% in these structures due to the selected beam dimensions. Table V shows the data on six beams that were fabricated on the wafer with 5.5 micron polyimide film. The deflections were measured with $\pm 3$ microns accuracy. The stress to modulus ratio for this samples is $0.0145 \pm 0.002$, some what higher than expected. There are two explanations: first, the stress in the polyimide film of this wafer is higher than normally observed (i.e. the three 3x3 mm samples of table II had unusually high stress). Second, the film could have yielded since the strains are high, on the order of 4%. On the wafer with the thicker polyimide film, although the film cracked above 4.5% strain, it did not break until 8% strain was reached. Ratio of the stress to modulus calculated from measurements on this sample are also in agreement with the above results for strains close to 4.5%. The ratio increases for higher strains, which is attributed to the cracking of the film, acting like the film is yielding. In a thin film, cracks are fatal while in the thicker film the cracks provide partial relaxation of the stress in the member. Even though, there is not enough data for a firm conclusion, it may be assumed that the film is yielding at strains close to 4%. To confirm this, the stress to modulus ratio has to be determined for this film at lower strains. This can be done by either adjusting the dimensions of the structures or putting T structures on the sample.

Figure 53 shows a SEM photograph of a typical fabricated beam on the 5.5 micron thick polyimide sample. The dimensions are 1500 microns long by 690 microns wide, changing to 80 microns wide (20 microns for each member) for a length of 505 microns. Figure 54 is the magnified view of the boundary in the figure

| $L_1$ (μ) | $L_2$ (μ) | $W_1$ (μ) | $W_2$ (μ) | δ (μ) | $\frac{N_o}{E}$ |
|---|---|---|---|---|---|
| 1535 | 505 | 690 | 2x45 | 13.0 | 0.0136 |
| 1535 | 505 | 690 | 2x45 | 13.0 | 0.0136 |
| 1535 | 505 | 690 | 4x20 | 14.0 | 0.0140 |
| 2510 | 505 | 690 | 2x95 | 11.5 | 0.0151 |
| 2510 | 505 | 690 | 2x95 | 12.0 | 0.0156 |
| 2510 | 505 | 690 | 4x45 | 12.0 | 0.0149 |

Table V: Data on fixed-end beam structures

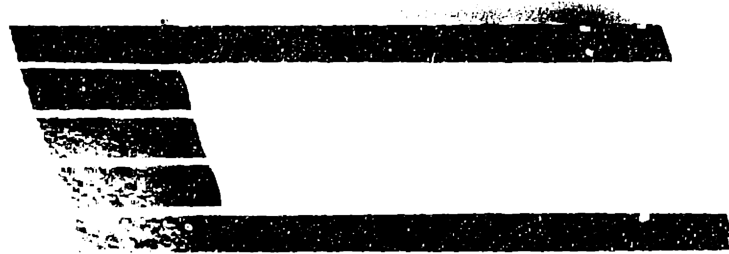


Figure 50: A [illegible] fixed end beam

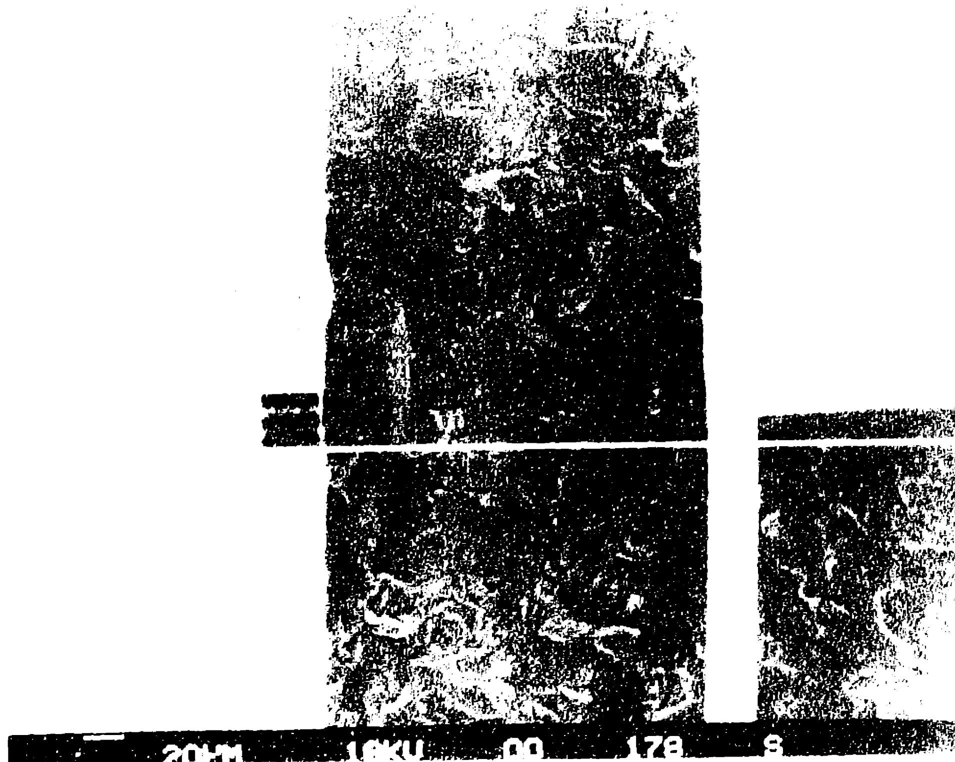


Figure 51: A [illegible] placed width change boundary

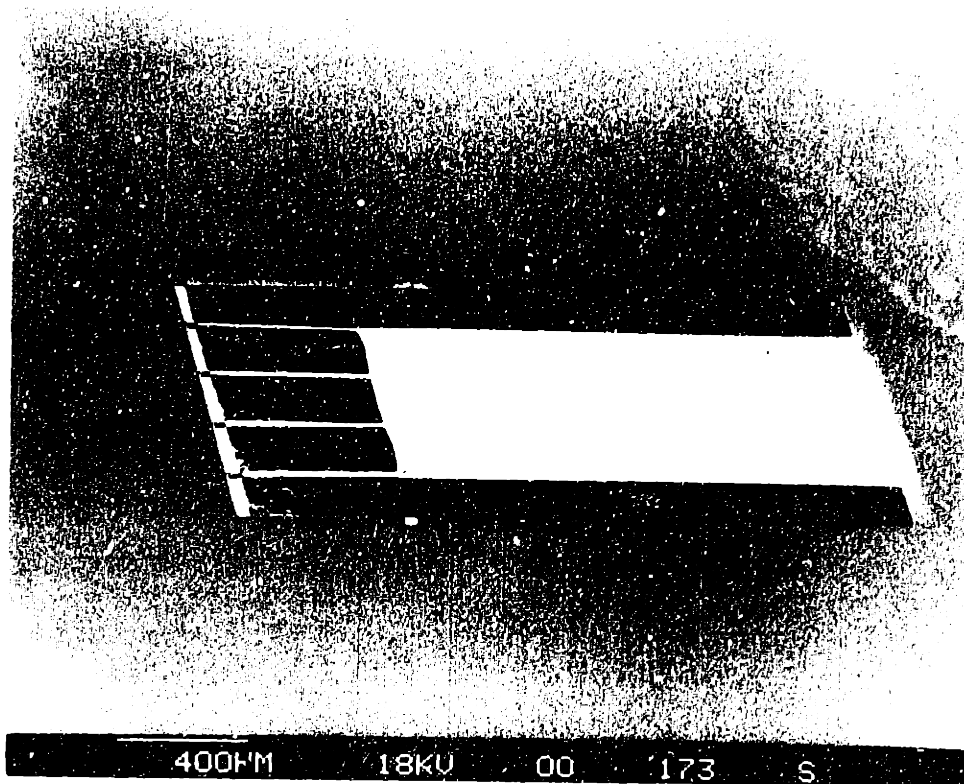


Figure 53: A typical released fixed-end beam

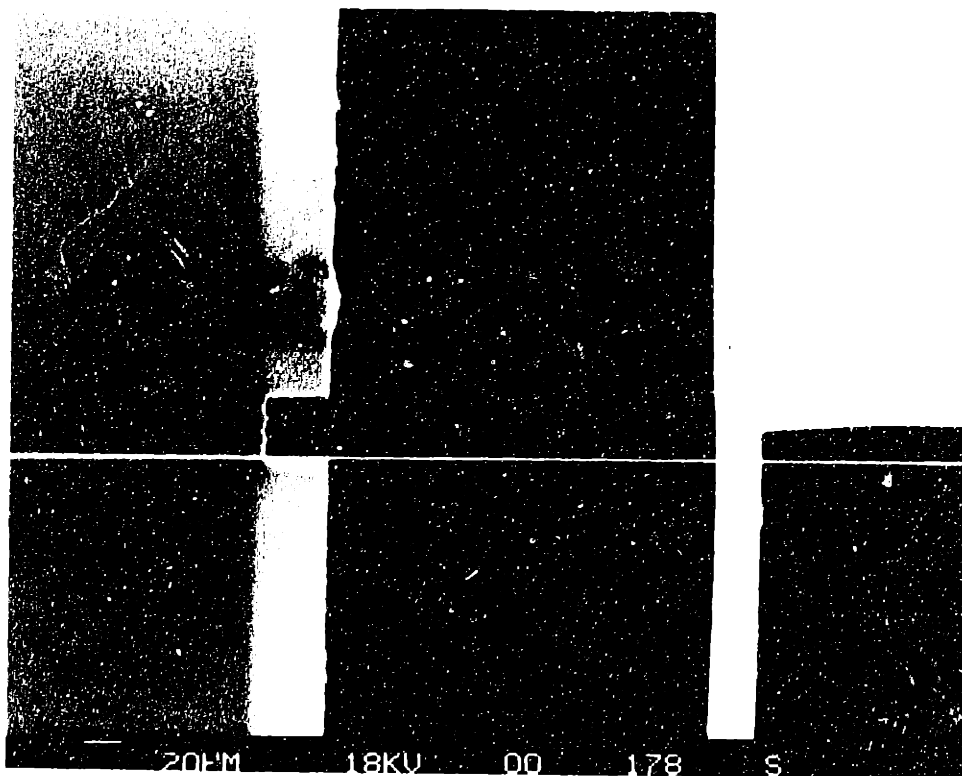


Figure 54: A magnified view of the displaced width-change boundary



INTENTIONAL DUPLICATE EXPOSURE

53. The white line marks where the width-change boundary was located before the structure was released. The displacement in this case is 14 microns Figure 55 shows two beams side by side, demonstrating the film failure in one structure when the strains in the members exceeded 4.5%. The dimensions for intact beam are 2500 microns long by 690 microns wide, changing to 180 microns wide (45 microns for each member) for a length of 500 microns. The failed structure is identical except the thin members are each 20 microns wide (adding up to a total of 80 microns). Note that the failure has not occurred in the edges were there are stress concentrations, in which case it would not be possible to observe the ultimate strain of the material.

In summary, beam dimensions were chosen to study a variety of polyimide chemistries with BTDA-ODA/MPDA being the first to try. This polyimide develops failure signs at strains above 4.5% and fails at above 8% strain (for 8.5 micron thick film). The ultimate strains for BTDA-ODA/MPDA polyimide were thought to be above 10% from findings of Weber and Gupta [117] by tensile studies on a similar chemistry polyimide. The fixed-end beam structures are appropriate for studying the stress to modulus ratio at high strains. The yield strain and the ultimate strain of thin films under tension have been introduced. These structure can be used in situ with accurate control on the dimensions and axial loading of the beam. The film can be viewed in situ as strained with optical and scanning electron microscope, revealing failure signs such as cracking.

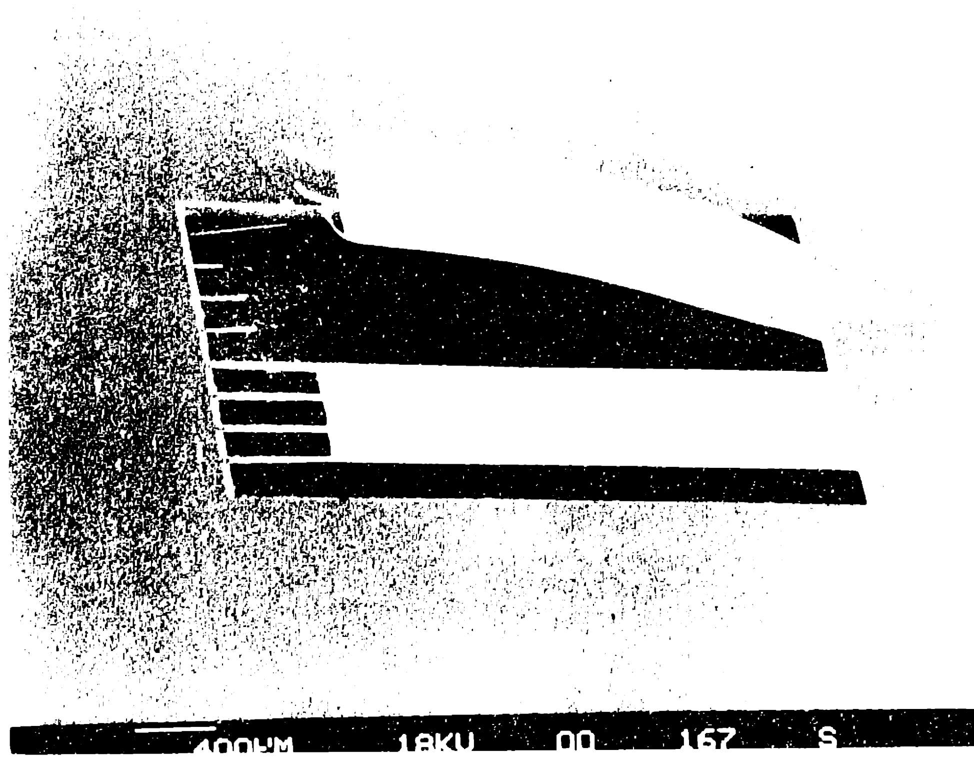


Figure 55: Breaking the film by exceeding its ultimate strain

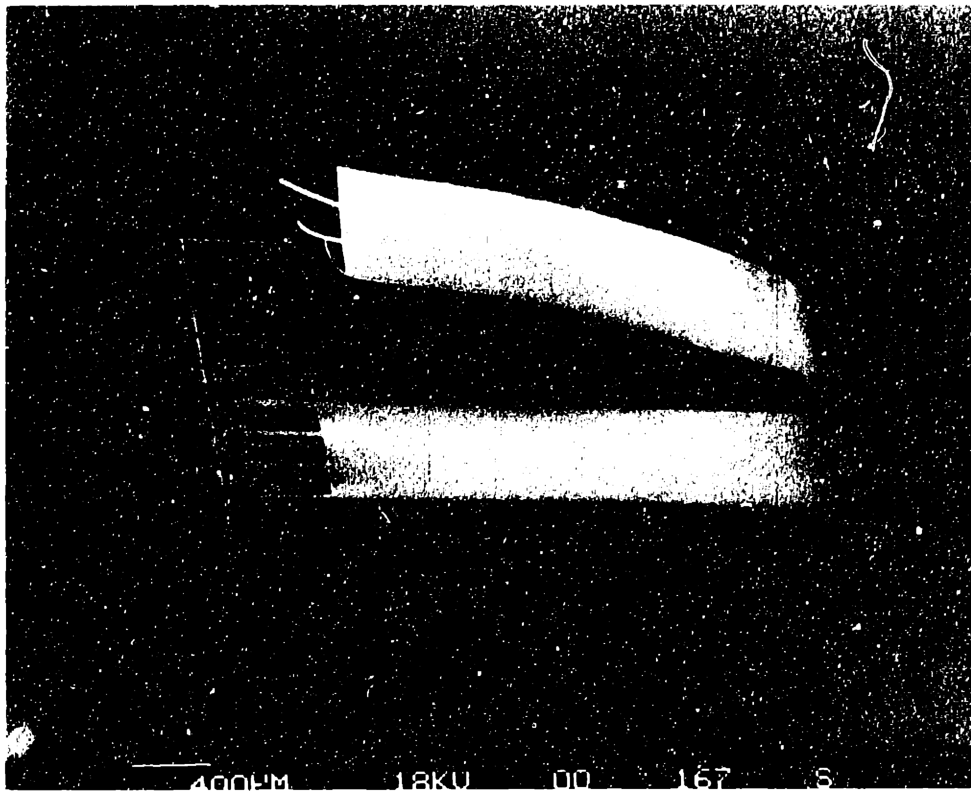


Figure 55: Breaking the film by exceeding its ultimate strain



INTENTIONAL DUPLICATE EXPOSURE

## 5.3 Short Polyimide Cantilever Beams

A series of 200 microns wide polyimide cantilever beams were fabricated ranging in length from 145 to 1200 microns at four locations on each of the two wafers with the T structures of section 5.1 (5.5 and 8.0 microns thick polyimide films). The lengths of these cantilever beams were measured before and after the silicon diaphragms were removed to release the structures. The reduction in the length of the beams divided by the length of the beam after release is equal to the stress to modulus ratio. The cantilever beams longer than 650 microns were bent slightly and were not used in the measurements. The bending of the longer cantilever beams was not well behaved and was not considered for measuring stress non-uniformity through the thickness of the film. Table VI presents the data for five different size cantilever beams from the sample with the 5.5 micron thick polyimide film. The value for the stress to modulus was found to be $0.01 \pm 0.001$, in good agreement with the value found for the same film using T structures of section 5.1. Uncertainty in the measurements is smaller because the length of the beams are short and can be measured more precisely. Figure 56 shows an optical photograph of a series of the polyimide cantilever beams fabricated on a 7.0 micron polyimide film. Note that the shorter beams are flat, meaning that the stress variation through the thickness of the film is not large. The slight reflection from the cantilevers may be due to aluminum residue.

| Nominal length ($\mu$) | $\frac{N_o}{E}$ |
|---|---|
| 145 | 0.0106 |
| 270 | 0.0104 |
| 390 | 0.0113 |
| 520 | 0.0097 |
| 640 | 0.0106 |

Table VI: Data for the polyimide cantilever beams

Figure 56: Seven micron thick polyimide cantilever beams

## 5.4 Overall View of the Released Structures

In this chapter, structures for studying the mechanical properties of thin films under tensile stress have been introduced. Mechanical properties of BTDA-ODA/MPDA polyimide was studied, and the measured stress to modulus values are shown to be in agreement with measurements done by membrane load-deflection studies. By fabricating the different types of the released structures on the same sample, measurement on all the mechanical properties of the film can be performed. As was described in the previous chapter, a small suspended polyimide structure can be incorporated on the same sample for load-deflection studies. This would provide the value for the residual tensile stress of the film. With this value known, the modulus can be extracted from the measurements on the released structures since the ratio of the stress to modulus is measured. Knowing the residual stress, the fixed-end beam structures can be used to trace out the entire stress-strain curve for the film, indicating the yield and failure strengths.

These structures undergo standard microelectronics fabrication processes and their mechanical properties are the same as when they are used in integrated circuit and solid state sensor fabrication. As shown in figure 31, many structures can be fabricated across the total area of the wafer, studying the mechanical properties of the film locally. This of great value and is seldom possible using other techniques. Since the structures are the measurement devices, the wafer can be exposed to many conditions to study various effects on the film's mechanical properties. One simply keeps track of the deformation changes for these studies. Fatigue and creep in the film can be studied in the same way. The deformations can be studied as a function of the sample (film) temperature to extract the components of the intrinsic stress and the thermal stress, due to the thermal coefficient of expansion mismatch. Finally, these structures can be extended to study of mechanical properties for multilayer films.

In all cases, displacements or deflections have to be measured. It is demonstrated that the uncertainty in these measurements directly effects the uncertainty in the calculated values. However, for all parameters of interest but one, even crude optical measurements cause uncertainties of less than 20% in the extracted parameters. For accurate measurements of Poisson's ratio using the T structures, better accuracy than $\pm 0.5$ is necessary. This accuracy can be attained by laser diffractometry as

previously explained.

Note that in all cases the deformations are not dependent on the film thickness directly, meaning that to identical structure made on different thickness polyimide films should have identical deformations as long as the stresses in both films are the same. The film thickness drops out of the final equations describing the deformations because the loaded and the loading members have the same thickness. In addition, since the entire structure is made of one material, the measured parameter is the stress to modulus ratio. If either the loading or the loaded member would be made of a material of known properties, both the residual stress and the modulus could be extracted for the material of interest.

# 6 Conclusion

The outcome of this study has been the development of a series of structures that can be fabricated in a thin film (with residual tensile stress) on silicon to characterize the mechanical properties of this film *in situ*. Load-deflection studies on small suspended membranes of the film measures the residual stress while the released structures measure the other parameters of interest. The released structures demonstrate the ability to use the films residual stress as a loading arrangement to put the material under desired loads. It has been shown that the blister test for adhesion studies can be conducted controllably and is valuable in extracting quantitative values for the work of adhesion of the interfaces in microelectronics. BTDA-ODA/MPDA polyimide has been used as the case study in all the above developments.

Fabrication technologies have been documented for preparation of the required test samples. Silicon micromachining constitutes the core of these technologies. Because of the many undesirable characteristics of the commonly used anisotropic etchants of silicon, KOH and EDP, a less thoroughly studied anisotropic etchant was used in this work. This etchant is a 50-50 mixture of hydrazine-water solution. The etching characteristics of this solution was studied in detail. The etching reactor design, the operational procedure, and the safety issues are reviewed.

# Appendices

## A Boron Spreading Resistance Data

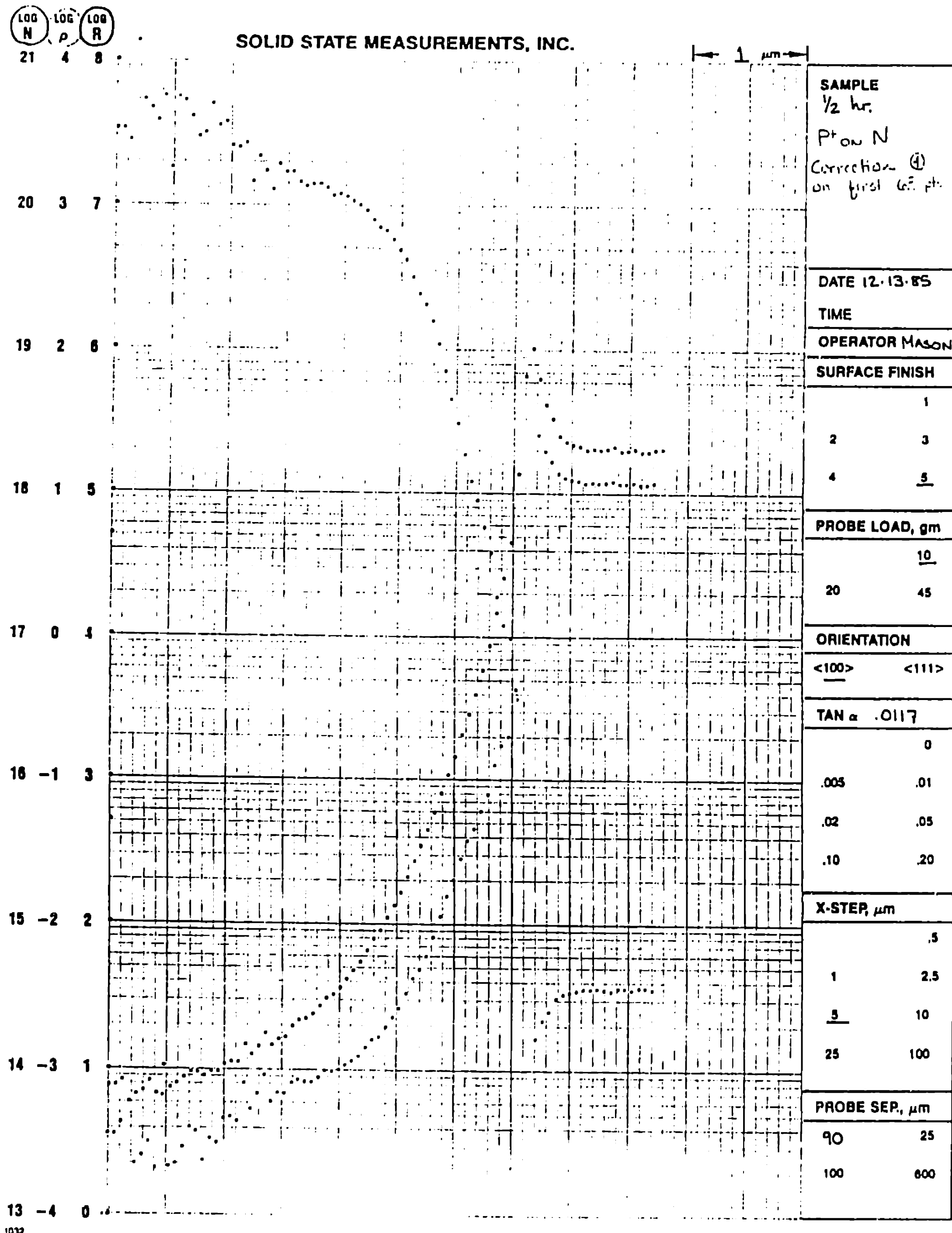

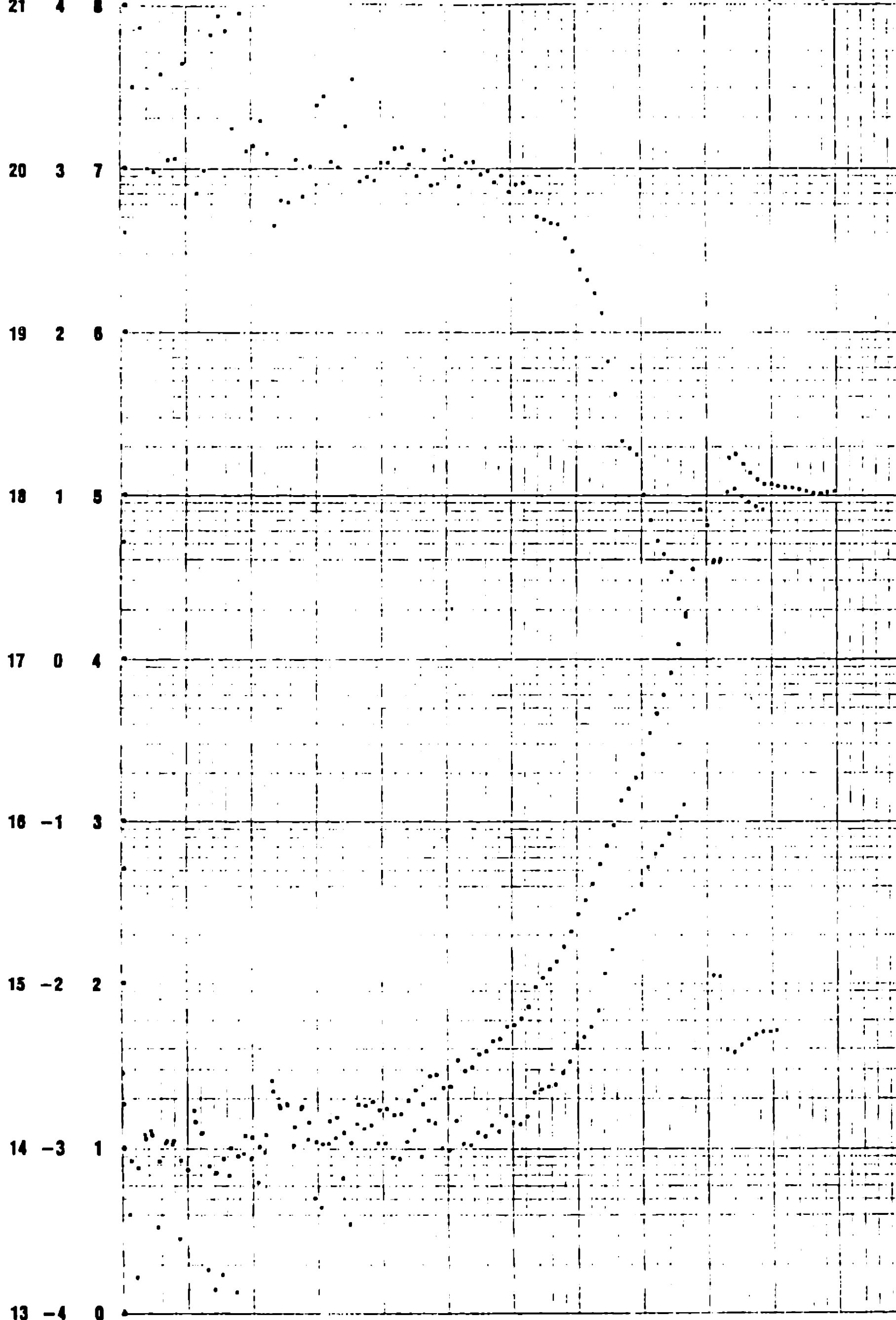
LOG N
LOG ρ
LOG R
SOLID STATE MEASUREMENTS, INC.
1 μm
SAMPLE
MEHRAN
3/4 HR.
DATE 12.13.85
TIME
OPERATOR MASON
SURFACE FINISH
PROBE LOAD, gm
ORIENTATION
<100>
<111>
TAN α .0217
X-STEP, μm
PROBE SEP., μm
90
GP-113

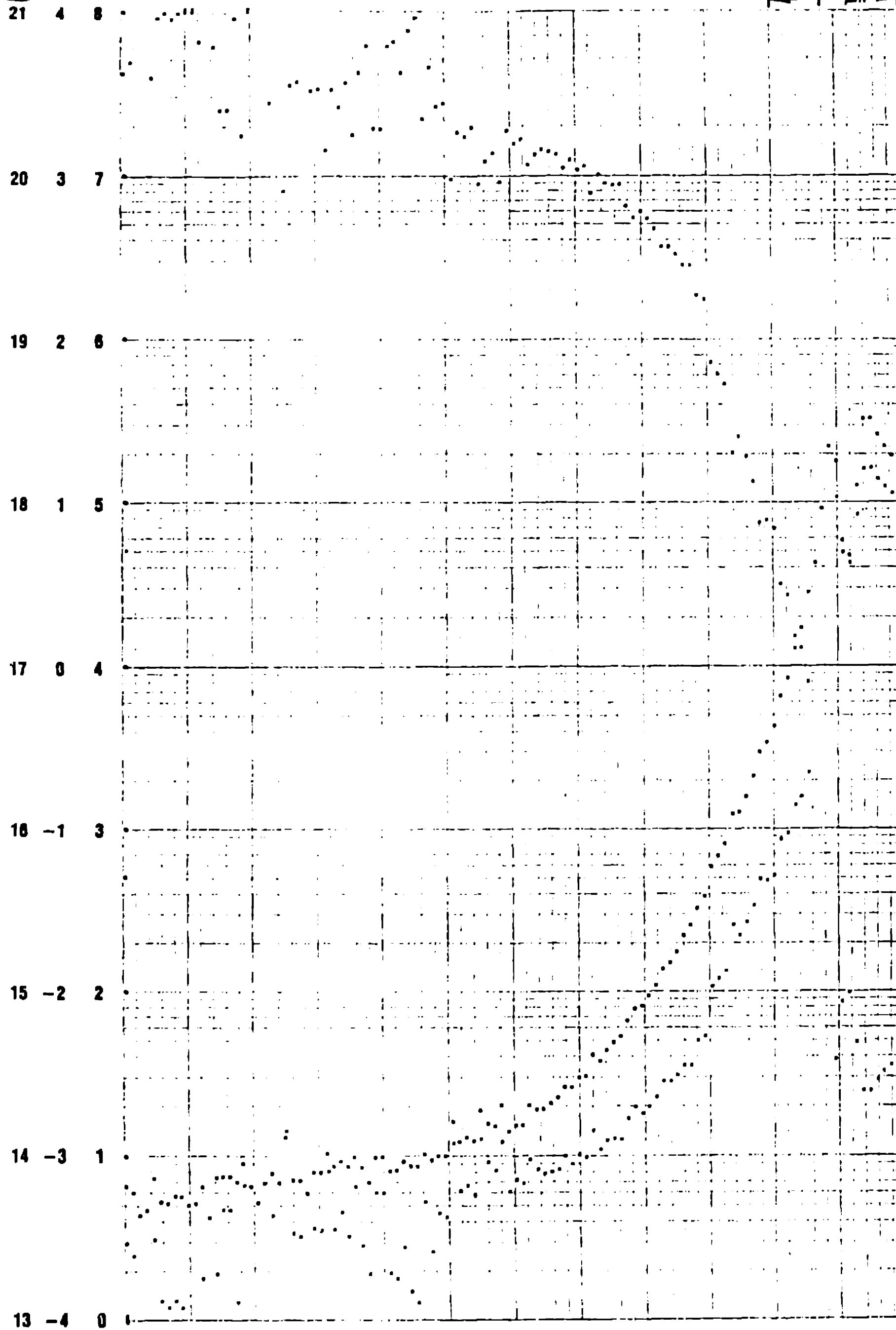
LOG N
LOG ρ
LOG R
SOLID STATE MEASUREMENTS, INC.
1 μm
21 4 8
20 3 7
19 2 6
18 1 5
17 0 4
16 −1 3
15 −2 2
14 −3 1
13 −4 0
1032
SAMPLE
MEHRAN
1 HR.
DATE 12·16·85
TIME
OPERATOR MASON
SURFACE FINISH
1
2 3
4 5
PROBE LOAD, gm
10
20 45
ORIENTATION
<100> <111>
TAN α .0213
0
.005 .01
.02 .05
.10 .20
X-STEP, μm
.5
1 2.5
5 10
25 100
PROBE SEP., μm
90 25
100 600
GP-113

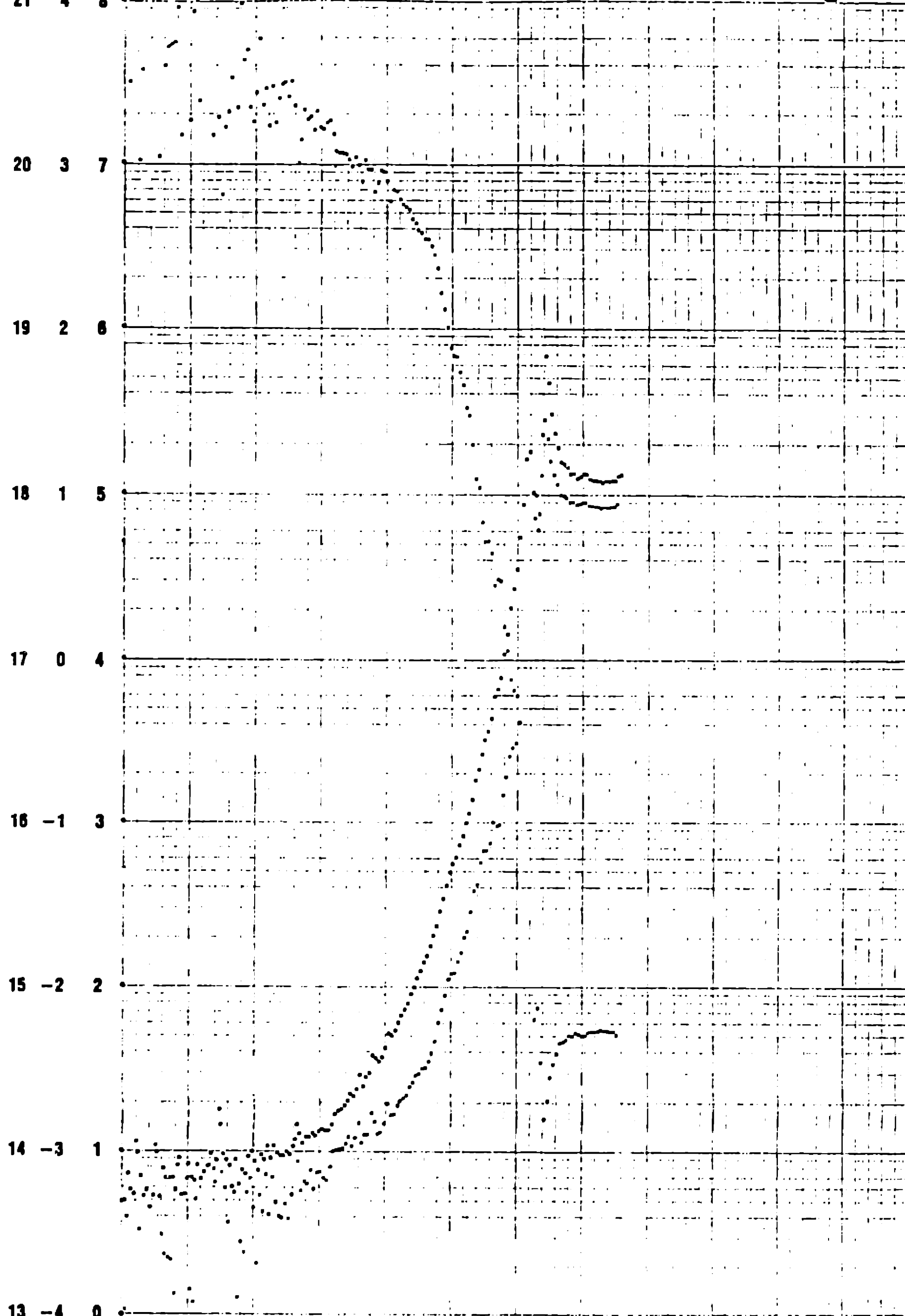
LOG N
LOG ρ
LOG R
SOLID STATE MEASUREMENTS, INC.
2 μm
SAMPLE
MEHEAN
1½ HR
DATE 12-16-85
TIME
OPERATOR MASON
SURFACE FINISH
PROBE LOAD, gm
ORIENTATION
<100>
<111>
TAN α .0192
X-STEP, μm
PROBE SEP., μm
90
GP-113

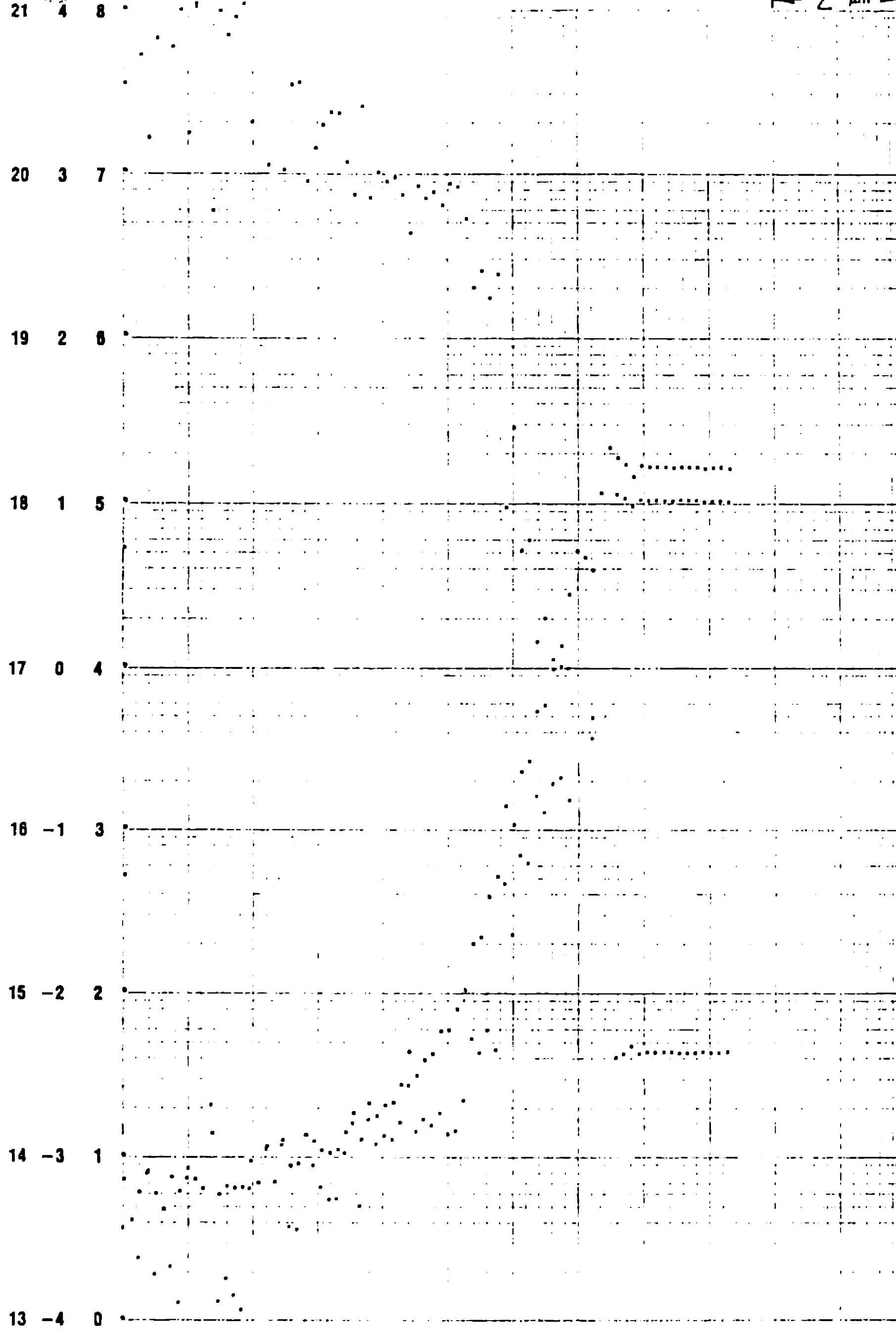
SOLID STATE MEASUREMENTS, INC.
LOG N
LOG ρ
LOG R
2 μm
SAMPLE
MEHRAN
2 HR
DATE 12·16·85
TIME
OPERATOR MASON
SURFACE FINISH
PROBE LOAD, gm
ORIENTATION
TAN α .0485
X-STEP, μm
PROBE SEP., μm
90
1032
GP-113

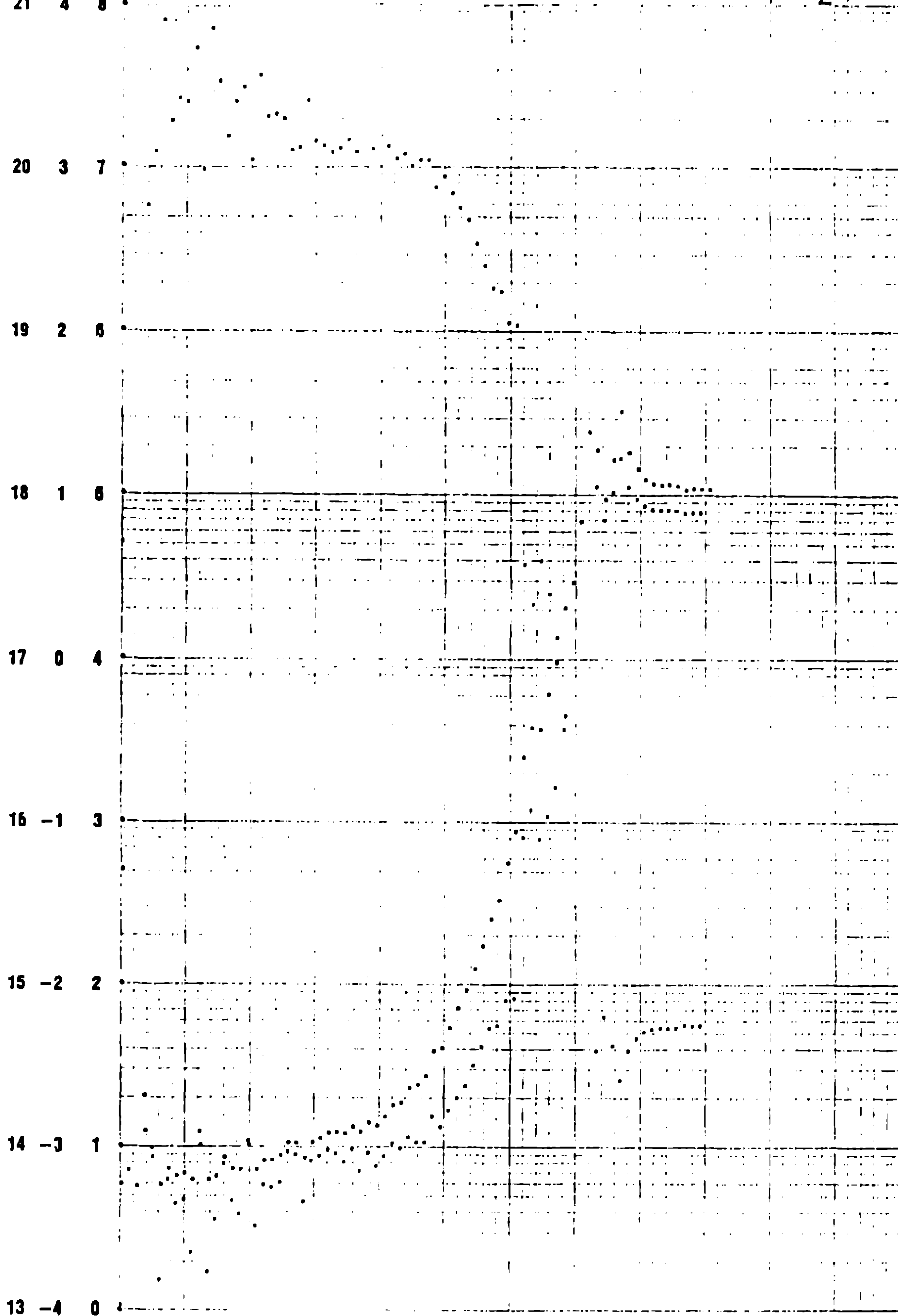
LOG N
LOG ρ
LOG R
SOLID STATE MEASUREMENTS, INC.
2 μm
SAMPLE
DATE 12·16·85
TIME
OPERATOR MASON
SURFACE FINISH
PROBE LOAD, gm
ORIENTATION
<100>
<111>
TAN α .0493
X-STEP, μm
PROBE SEP., μm
90

# B Etching System Parts

Supplier: Lab Glass, Inc.

| PART | CATALOG NUMBER | PRICE |
|---|---|---|
| Reflux Container (1000 ml) | LG-8080-102 | $70.40 |
| Cover (24/20) | LG-8086-100 | $94.20 |
| Cooling Tower | LG-4811-100 | $115.00 |
| Clamp (4 inch) | LC-7316-106 | $68.90 |
| 1000 ml Heater | TM-572-102 | $99.00 |

Supplier: Micro-Glass, Inc.

| | | |
|---|---|---|
| 2 inch Wafer Quartz Boat | 3001024 | $110.00 |
| 3 inch Wafer Quartz Boat | 3002043 | $110.00 |

# C Silicon Diaphragm Fabrication

## I. BORON DEPOSITION

1. Standard RCA clean and spin-dry.
2. Stable nitrogen flow of 0.6 SCFH and oxygen flow of 0.07 SCFH in the furnace.
3. Load wafers into furnace at 900C.
4. Adjust the temperature to 1175C (it takes the furnace 40 minutes to reach this temperature).
5. Deposit boron at 1175C for 2 hours, resulting in an etch-stop layer 4.7 microns thick.
6. Ramp the furnace temperature down to 900C before unloading (it takes 45 minutes to cool down to 900 degrees).
7. Unload wafers at 900C.

This deposition should give sheet resistance less than one ohms/square measured on the six point probe.

## II. OXIDATION

1. Set up the oxidation furnace for 990C.
2. Stabilize oxygen flow of 3.5 SCFH in the furnace.
3. Prepare for wet oxidation with 95C steam.
4. Remove the borosilicate glass on the samples in 10:1 HF.
5. Rinse samples properly by going through the DI cascade and spin-dry.
6. Perform oxidation: 15 minute dry oxidation, 45 minutes wet oxidation, and 15 minutes dry oxidation.

Oxide thickness grown should be close to 3200 angstrums.

## III. PHOTOLITHOGRAPHY

1. Rinse and dry the wafers.
2. Perform dehydration bake at 200C for 30 minutes.
3. Spin negative resist (KTI-732) on the front at 3000 rpm for 30 seconds (this should give a 1.35 micron film thickness).
4. Soft bake at 95C for 20 minutes.
5. Blank expose the wafer for 20 seconds using channel 1 setting of the standard resolution aligner (10 mW/square centimeter intensity at wafer).
6. Spin negative resist (KTI-732) on the back at 5000 rpm for 30 seconds (this should give a 0.85 micron film thickness).
7. Soft bake at 95C for 25 minutes.
8. Align pattern windows to the (110) directed flat of the wafer.
9. Expose for 1.5 seconds using channel 1 setting of the standard resolution aligner (10 mW/square centimeter intensity at wafer).
10. Spray develop with Projection Developer for 30 seconds.
11. Spray rinse with Micro Rinse for 20 seconds and dry.
12. Post bake at 135C for 30 minutes.
13. Transfer the pattern to the oxide using buffered-oxide-etch.
14. Rinse and dry the wafers.
15. Remove the resist in 3:1 sulforic/peroxide solution (2 minutes in a freshly mixed solution is sufficient).
16. Rinse and dry the wafers.

At this point, the oxide on the back should be patterned properly while the oxide on the front is left intact.

## IV. HYDRAZINE ETCH

1. Rinse all etching reactor components with DI water and dry.
2. Give samples a 20 sec 20:1 HF dip and rinse with DI water.
3. Load samples into the reactor.
4. Funnel 700 ml of Hydrazine at room temperature into the reactor (wafers will be immersed in the solution from at this point).
5. Flush reactor with nitrogen initially and then set the flow for 15 cubic inches per min.
6. Bring the solution temperature up to 115C (by setting the variac to 100 for 20 minutes and then to 60 for the duration). It take about 35 minutes to stabilize at that temperature.
7. Etch at 118C until the diaphragms are completed (approximately 4 hours).
8. Remove the reactor from the heating jacket and immerse it into cold water to reduce the temperature below 50C.
9. Open the reactor, remove the samples, and close the reactor.
10. Rinse the samples for at least 5 minutes in flowing DI water and dry with nitrogen gently.
11. Pure the used Hydrazine in a container and store it in a vented area.
12. Rinse the glassware for at least 2 hours in tap water.

At this point, the diaphragms should be etched out and the oxide on the sample shculd be close to 2800 angstrums thick.

# D Micromachining by Under-etching

## I. FIRST OXIDATION

1. Set up the oxidation furnace for 1100C.
2. Stabilize oxygen flow of 3.5 SCFH in the furnace.
3. Prepare for wet oxidation with 95C steam.
4. Standard RCA clean and spin-dry wafers.
5. Perform oxidation: 10 minutes dry oxidation, 50 minutes wet oxidation, and 10 minutes dry oxidation.

At this point, oxide is close to 5000 angstrom thick.

## II. PHOTOLITHOGRAPHY, MASK 1

1. Immediately after oxidation, spin negative resist at 5000 rpm for 30 seconds.
2. Soft bake at 95C for 25 minutes.
3. Align the feature sides to the (110) directed flat of the wafer on a few samples and 5 and 10 degrees off on the others.
4. Expose the pattern for 1.5 seconds using the channel 1 setting of the standard aligner ( 10 mW/square centimeter intensity at wafer).
5. Spray develop with Projection Developer for 30 seconds.
6. Spray rinse with Micro Rinse for 20 seconds and dry.
7. Post bake at 135C for 30 minutes.
8. Transfer the pattern to oxide in buffered-oxide-etch and rinse.
9. Remove the resist in 3:1 sulforic/peroxide (2 minutes is sufficient in a freshly mixed solution) and rinse.

At this point, samples are ready for forming the boron doped regions.

## III. BORON DEPOSITION

1. Same as boron deposition in APPENDIX C but the deposition time at 1175C is 3 hours, resulting in a boron etch-stop 6 microns thick.

## IV. SECOND OXIDATION

1. Same as oxidation in APPENDIX C.

## V. PHOTOLITHOGRAPHY, MASK 2

1. Rinse and dry wafers.
2. Perform dehydration bake at 200C for 30 minutes.
3. Spin positive resist (1370 F) on the back side at 3000 rpm for 30 seconds (this should give a 1.5 microns thick film).
4. Post bake at 135C for 30 minutes.
5. Spin positive resist (1370 F) on the front side at 5000 rpm for 30 seconds (this should give a 1.0 micron thick film).
6. Soft bake at 95C for 25 minutes.
7. Align Mask 2 to the Mask 1 features.
8. Expose 6 seconds using channel 1 setting of the standard resolution aligner (10 mW/square centimeter intensity at the wafer).
9. Develop in 1:1 KTI-213/DI-water solution for 60 seconds and then rinse.
10. Post bake at 135C for 30 minutes.
11. Transfer the pattern to oxide in buffered-oxide-etch and rinse.
12. Remove the resist in 3:1 sulforic/peroxide solution (2 minutes is sufficient in a freshly mixed solution) and rinse.

At this point, the front oxide is patterned, the back oxide is intact, and the samples are ready to be etched in Hydrazine.

## VI. HYDRAZINE ETCH

1. Same as Hydrazine etch in APPENDIX C except the etching temperature is 115C and the length of time for etching is 6 hours.

At this point, the 5 and 10 degrees misaligned structures are under-etched free except the suspended square plates.

# E Fabrication of Silicon Fibers

## I. FIRST OXIDATION

1. Same as first oxidation steps in APPENDIX D.

## II. PHOTOLITHOGRAPHY, MASK 1

1. Immediately after oxidation, spin negative resist (KTI-732) at 5000 rpm for 30 seconds.
2. Soft bake at 95C for 25 minutes.
3. Align the feature sides to the (110) directed flat of the wafer.
4. Expose the pattern for 1.5 seconds using the channel 1 setting of the standard aligner ( 10 mW/square centimeter intensity at wafer).
5. Spray develop with Projection Developer for 30 seconds.
6. Spray rinse with Micro Rinse for 20 seconds and dry.
7. Post bake at 135C for 30 minutes.
8. Transfer the pattern to oxide in buffered-oxide-etch and rinse.
9. Remove the resist in 3:1 sulforic/peroxide (2 minutes is sufficient in a freshly mixed solution) and rinse.

At this point, the oxide on the front is patterned, the oxide on the back is intact, and the sample is ready for boron deposition.

## III. BORON DEPOSITION

1. Same as Boron deposition in APPENDIX C except for duration of 3 hours.

This deposition should give sheet resistance below one ohm per square measured with the six point probe.

## IV. SECOND OXIDATION

1. Same as oxidation step in APPENDIX C.

## V PHOTOLITHOGRAPHY, MASK 2

1. Rinse and dry wafers.
2. Perform dehydration bake at 200C for 30 minutes.
3. Spin negative resist (KTI-732) on the back side at 5000 rpm for 30 seconds (this should give a 0.85 microns thick film).
4. Soft bake at 95C for 25 minutes.
5. Align Mask 2 on the back to the Mask 1 features on the front using the cleaved edges as alignment marks.
6. Expose 1.5 seconds using channel 1 setting of the standard resolution aligner (10 mW/square centimeter intensity at the wafer).
7. Spray develop with Projection Developer for 30 seconds.
8. Spray rinse with Micro Rinse for 20 seconds and dry wafer.
9. Post bake at 135C for 30 minutes.
10. Transfer the pattern to oxide in buffered-oxide-etch and rinse.
11. Remove the resist in 3:1 sulforic/peroxide solution (2 minutes is sufficient in a freshly mixed solution) and rinse.

At this point, the back side windows are opened, the front oxide is removed, and the sample is ready to be etched in Hydrazine. The front oxide is not necessary, since the boron doping on the front will mask etching.

## VI. HYDRAZINE ETCH

1. Same as Hydrazine etch step in APPENDIX C.

At this point, the fibers, supported in a frame, are etched out.

# F Fabrication of Polyimide Membranes

## I. THIN SILICON DIAPHRAGM FABRICATION

1. APPENDIX C

## II. POLYIMIDE COATING

1. Give wafers a 30 seconds 10:1 HF dip.
2. Rinse the wafers by taking them through the cascade rinse.
3. Dry the wafers (if diaphragms are smaller than 9 square millimeter they can be spin-dried).
4. Use the dry box to spin polyimide.
5. Spin-coat the BTDA-ODA/MPDA polyimide using the costum made vacuum spinning chuck at 4000 rpm for 120 seconds (this would result in a film thickness of 2.5 microns).
6. Soft bake at 135C for 14 minutes.

Iterate steps 5 and 6 until desired thickness is achieved (normally four coat to result in 10 microns).

7. Post bake at 436C for 45 minutes in the cure furnace.

At this point, the polyimide/silicon dioxide/silicon diaphragms are ready. By removing the two bottom layers, polyimide diaphragms are fabricated.

## III. PLASMA REMOVAL OF THE SUPPORTING SILICON DIAPHRAGM

1. Set up the LAM REACTIVE ION ETCHER with the parameters:

   | | |
   |---|---|
   | Pressure: | 300 mtorr |
   | RF Power: | 250 watts |
   | Gap : | 1.5 cm |
   | SF6 : | 150 SCCM |
   | HELIUM : | 150 SCCM |

2. Etch for a duration of 10 minutes to remove the 4.7 micron thick silicon diaphragm and the oxide.

At this point, the polyimide diaphragms are ready.

# G Fabrication of Released Structures

I. THIN SILICON DIAPHRAGM FABRICATION

1. APPENDIX C

II. POLYIMIDE COATING

1. Remove the oxide on the wafer in 10:1 HF.
2. Rinse the wafers by taking them through the cascade rinse.
3. Dry the wafers (if diaphragms are smaller than 9 square millimeter they can be spin-dried).
4. Use the dry box to spin polyimide.
5. Spin-coat the 2555 polyimide from Dupont using the costum made vacuum spinning chuck at 4000 rpm for 120 seconds (this would result in a film thickness of 2.5 microns).
6. Soft bake at 135C for 14 minutes.

Iterate steps 5 and 6 until desired thickness is achieved (normally four coat to result in 10 microns).

7. Post bake at 436C for 45 minutes in the cure furnace.

At this point, the polyimide/silicon dioxide/silicon diaphragms are ready.

III. ALUMINUM EVAPORATION

1. Evaporate 2000 angstrums of aluminum on the polyimide either using the filament evaporator or the E-beam evaporator.

## IV. PHOTOLITHOGRAPHY, MASK 2

1. Spin negative resist (KTI-732) on the Al at 5000 rpm for 30 seconds using the special spinning chuck (this should give a 0.85 micron thick film).
2. Soft bake at 95C for 25 minutes.
3. Align Mask 2 to the Mask 1 features such that the structure is located properly on the Al/polyimide/silicon diaphragms.
4. Expose 1.0 seconds using channel 1 setting of the standard resolution aligner (10 mW/square centimeter intensity at the wafer).
5. Spray develop with Projection Developer for 30 seconds.
6. Spray rinse with Micro Rinse for 20 seconds and dry wafer.
7. Post bake at 135C for 30 minutes.

At this point, the pattern transfers are done using plasma environment.

## V. PLASMA PROCESSING FOR PATTERN TRANSFER AND RELEASING STRUCTURES

1. Pattern Aluminum in the LAM REACTIVE ION ETCHER:

Etching:

Pressure: 230 mtorr
RF Power: 300 watts
Gap : 1.5 cm
CCl4 : 130 SCCM
Helium : 130 SCCM
Time : 2 minutes

Passivation:

Pressure: 230 mtorr

RF Power: 300 watts

Gap : 1.5 cm

SF6 : 130 SCCM

02 : 13 SCCM

Time : 1 minute

2. Pattern polyimide and remove resist:

Pressure: 500 mtorr

RF power: 300 watts

Gap : 1.5 cm

02 : 150 SCCM

Helium : 150 SCCM

Time : 1 min/0.7 micron

3. Remove aluminum in Phosphoric-Acidic-Nitric solution.

4. Remove the thin silicon diaphragms from the back in the LAM REACTIVE ION ETCHER:

Pressure: 300 mtorr

RF Power: 250 watts

Gap : 1.5 cm

SF6 : 150 SCCM

HELIUM : 150 SCCM

2. Etch for a duration of 10 minutes to remove the 4.7 micron silicon diaphragms.

# References

[1] K.L. Mittal, "Adhesion measurement of thin films," *Electrocomponent Sci. Technol.*, vol. 3, pp. 21-42, 1976.

[2] P.M. Schaible and R. Glang, "Automated measurement of stress in in thin films," in F. Vranty, ed., *Thin Dielectric Films*, The Electrochemical Society, NY, pp. 577-594, 1969.

[3] R.W. Hoffman, "The mechanical properties of thin condensed films," in G. Haas and R.E. Thun, eds., *Physics of Thin Films*, vol. 3, pp. 219-225, 1966.

[4] G.P. Anderson, S.J. Bennett, and K.L. DeVries, *Analysis and testing of adhesive bonds*, Academic Press, New York, ch. 3, 1977.

[5] J.A. Hinkley, "A blister test for adhesion of polymer films to $SiO_2$" *J. Adhesion*, vol. 16, pp. 115-125, 1983.

[6] M.G. Allen, "Measurement of mechanical properties and adhesion of thin polyimide films," M.I.T., M.S. Thesis, Department of Chemical Engineering, June 1986, unpublished.

[7] D.L. Spears and H.I. Smith, "X-ray lithography: A new high resolution replication process," *Solid State Technol.*, vol. 15, pp. 21-26, July 1972.

[8] D.L. Spears and H.I.Smith, "High resolution pattern replication using soft X-rays," *Electron Lett.*, vol. 8, no. 4, pp. 102-104, Feb. 1972.

[9] D.L. Spears, H.I. Smith, and E. Stern, "X-ray replication scanning electron microscope generated patterns," in *Proc. 5th Int. Conf. Electron and Ion Beams in Science and Technology*, R.Bakish, Ed. Princeton, NJ: The Electrochemical Society, p. 80.

[10] C.J. Schmidt, P.V. Lenzo, and E.G. Spencer, "Preparation of thin windows in silicon masks for X-ray lithography," *J. Appl. Phys.*, vol. 46, no. 9, pp. 4080-4082, Sept. 1975.

[11] P.V. Lenzo and E.G. Spencer, "High-speed low power X-ray lithography, *Appl. Phys. Lett.*, vol. 24, no. 6, pp. 289-291, Mar. 1974.

[12] E. Bassous, R. Feder, E. Spiller, and J. Topalian, "High transmission X-ray masks for lithographic applications," *Solid State Technol.*, vol. 19, no. 9, pp. 55-58, Sept. 1976.

[13] W.T. Tsang, C.C. Tseng, and S. Wang, "Optical waveguides fabricated by prefrential etching," *Appl. Opt.*, vol. 14, no. 5, pp. 1200-1206, May 1975.

[14] C.C. Tseng, D. Botez, and S. Wang, "Optical bends and ring fabricated by prefrential etching," *Appl. Phys. Lett.*, vol. 26, no. 12, pp. 699-702, June 1975.

[15] J.S. Harper and P.F. Heidrich, "High density multichannel optical waveguides with integrated couplers," *Wave Electronics*, vol. 2, pp. 369-377, 1976.

[16] J.D. Crow, L.D. Comerford, R.F. Laff, M.J. Brady, and J.S. Harper, "GaAs laser array source package," *Opt. Lett.*, vol. 1, no. 1, pp. 40-42, July 1979.

[17] T.O. Sedgwick, A.N. Broers, and B.J. Agule, "A novel method for fabrication of ultrafine metal lines by electron beams," *J. Electrochem. Soc.*, vol. 119, no. 12, pp. 1769-1771, Dec. 1972.

[18] A.I. Stoller, " The etching of deep vertical-walled patterns in silicon," *RCA Rev.*, vol. 31, pp. 271-275, June 1970.

[19] W.T. Tsang and S. Wang, "Prefrentially etched diffraction grating in silicon," *J. Appl. Phys.*, vol. 46, no. 5, pp. 2163-2166, May 1975.

[20] D.L. Kendall, "On etching very narrow groves in silicon," *Appl. Phys. Lett.*, vol. 26, pp. 195-198, Nov. 1974.

[21] I.L. Berry and A.L. Caviglia, "High resolution patterning of silicon by selective gallium doping," *J. Vac. Sci. Technol. B*, vol. 1, no. 4, pp. 1059-1061, Oct./Dec. 1983.

[22] E. Bassous, "Nozzles formed in monocrystalline silicon," U.S. Patent 3 921 916, Nov. 1975.

[23] E. Bassous, L. Kuhn, A. Reisman, and H.H. Taub, "Ink jet nozzles," U.S. Patent 4 007 464, Feb. 1977.

[24] E. Bassous, H.H. Taub, and L. Kuhn, "Ink jet printing nozzle arrays etched in silicon," *Appl. Phys. Lett.*, vol. 31, no. 2, pp. 135-137, July 1977.

[25] K. Peterson, "Fabrication of an integrated, planar silicon ink-jet structure," *IEEE Trans. Electron Devices*, vol. ED-26, no. 12, pp. 1918-1920, Dec. 1979.

[26] E. Bassous anf E.F. Baran, "The fabrication of high precision nozzles by the anisotropic etching of (100) silicon," *J. Electrochem. Soc.*, vol. 125, no. 8, pp. 1321-1327, Aug. 1978.

[27] D.A. Kiewit, "Microtool fabrication by etch pit replication," *Rev. Sci. Instrum.*, vol. 44, no. 12, pp. 1741-1742, Dec. 1973.

[28] C.L. Huang and T. Van Duzer, "Schottky diodes and other devices on thin silicon membranes," *IEEE Trans. Electron Devices*, vol. ED-23, no. 6, pp. 579-583, June 1976.

[29] T.J. Rodgers and J.D. Meindl, "Epitaxial V-groove bipolar integrated circuit process," *IEEE Trans. Electron Devices*, vol. ED-20, pp. 226-232, Mar. 1973.

[30] T.J. Rodgers and J.D. Meindl, "VMOS: high speed TTL compatible MOS logic," *IEEE J. Solid-State Circiuts*, vol. SC-9, pp. 239-249, Oct. 1974.

[31] M.J. Declercq, "A new CMOS technology using anisotropic etching of silicon," *IEEE J. Solid-State Circuits*, vol. SC-10, no. 4, pp. 191-197, Aug. 1975.

[32] P. Ou-Yang, "Double ion implanted V-MOS technology," *IEEE J. Solid-State Circuits*, vol. SC-12, no. 1, pp. 3-10, Feb. 1977.

[33] K.E. Bean and J.R. Lawson, "Application of silicon crystal orientation and anisotropic effects to the controll of charge spreading in devices," *IEEE J. Solid-State Circuits*, vol. SC-9, no.3, pp. 111-117, June 1974.

[34] K.E. Bean and W.R. Runyan, "Dielectric isolation: comprehensive, current and future," *J. Electrochem. Soc.*, vol. 124, no.1, pp. 5C-12C, Jan 1977.

[35] E.S. Ammar and T.J. Rodgers, "UMOS transistors on (110) silicon, *IEEE Trans. Electron Devices*, vol. ED-27, no. 5, pp. 907-914, May 1980.

[36] H. Guckel, S. Larsen, M.G. Lagally, G. Moore, J.B. Miller, and J.D. Wiley, "Electromechanical devices utilizing thin silicon diaphragms," *Appl. Phys. Lett.*, vol. 31, no. 9, pp. 618-619, Nov. 1977.

[37] L.M. Roylance and J.B. Angell, "A batch fabricated silicon accelerometer," *IEEE Trans. Electron Devices*, vol. ED-26, no. 12, pp. 1911-1917, Dec. 1979.

[38] S.K. Clark and K.D. Wise, "Pressure sensitivity in anisotropically etched thin-diaphragm pressure sensors," *IEEE Trans. Electron Devices*, vol. 26, no. 12, pp. 1887-1896, Dec. 1979.

[39] K.E. Peterson, A. Shartel, and N.F. Raley, "Micromechanical accelerometer integrated with MOS detection circuitry," *IEEE Trans. Electron Devices*, vol. ED-29, no. 1, Jan. 1982.

[40] P.L. Chen, R.S. Muller, R.D. Jolly, G.L. Halac, R.M. White, A.P. Andrews, T.C. Lim, and M.E. Motamedi, "Integrated silicon microbeam PI-FET accelerometer," *IEEE Trans. Electron Devices*, vol. ED-29, no. 1, Jan. 1982.

[41] S.C. Terry, "A gas chromatography system fabricated on a silicon wafer using integrated circuit technology," Ph.D. dissertation, Stanford Univ. Elect. Engr. Dept., 1975.

[42] K.E. Peterson, "Micromechanical light modulator array fabricated on silicon," *Appl. Phys. Lett.*, vol. 31, no. 8, pp. 521-523, Oct. 1977.

[43] J.B. Price, "Anisotropic etching of silicon with potassium hydroxide water-isopropyl alchohol," in H.R. Huff and R.R. Burgess, Eds., *Semiconductor Silicon*, The Electrochemical Society Softbound Symposium Ser., Princeton, NJ, p. 339, 1973.

[44] A.I. Stoller, "The etching of deep vertical-walled patterns in silicon," *RCA Rev.*, vol. 31, p. 271, 1970.

[45] D.L. Kendall, "Vertical etching of silicon at very high aspect ratios, *Ann. Rev. Materials Sci.*, vol. 9, p. 373, 1979.

[46] D.F. Weirauch, "Correlation of the anisotropic etching of single crystal silicon spheres and wafers," *J. Appl. Phys.*, vol. 46, p. 1478, 1975.

[47] D.M. Allen and I.A. Routledge, "Anisotropic etching of silicon: a model diffusion-controlled reaction," *IEE Proc.*, vol. 130, Pt. I, no. 2, pp. 49-56, Apr. 1983.

[48] G. Kaminsky, "Micromachining of silicon mechanical strucures," *J. Vac. Sci. Technol. B*, vol. 3, no. 4, pp. 1015-1024, Jul./Aug. 1985.

[49] C.M. Drum and M.J. Rand, "A low-stress insulating film on silicon by chemical vapor deposition," *J. Appl. Phys.*, vol. 39, p. 4458, 1968.

[50] J.C. Greenwood, "Ethylenediamine-catechol-water mixture shows prefrential etching of p-n junctions," *J. Electrochem. Soc.*, vol. 116, p. 1325, 1969.

[51] A. Bohg, "Ethylenediamine-pyrocatechol-water mixture show etching anomaly in boron-doped silicon," *J. Electrochem. Soc.*, vol. 118, p. 401, 1971.

[52] A. Reisman, M. Berkinblit, S.A. Chan, F.B. Kaufman, and D.C. Green, "The controlled etching of silicon in catalyzed ethylene diamine-pyrocatechol-water solutions," *J. Electrochem. Soc.*, vol. 126, p. 1406, 1979.

[53] R.M. Finne and D.L. Klien, "A water-amine-complexing agent system for etching silicon," *J. Electrochem. Soc.*, vol. 114, no. 9, pp. 965-970, Sep. 1967.

[54] X.P. Wu, Q.H. Wu, and W.H. Ko, "A study on deep etching of silicon using EPW," *Proc. International Conference on Solid-State Sensors and Actuators*, pp. 291-293, June 1985.

[55] E.F. Baran, E. Bassous, and J. Wilson, "Anisotropic etching solution with high etch rate on single crystal silicon," *IBM Technical Disclosure Bulletin*, vol. 19, no. 10, p. 3953, Mar. 1977.

[56] E. Bassous, "Controlled anisotropic etching of single crystal silicon, *IBM Technical Disclosure Bulletin*, vol. 19, no. 9, pp. 3623-3624, Feb. 1977.

[57] N.F. Raley, Y. Sugiyama, and T. Van Duzer, "(100) Silicon etch-rate dependence on boron concentration in ethylenediamene-pyrocatechol- water solutions," *J. Electrochem. Soc.*, vol. 131, no. 1, pp. 161-171, Jan. 1984.

[58] K.E. Bean, "Anisotropic etching of silicon," *IEEE Trans. Electron Devices*, vol. ED-25, no. 10, pp. 1185-1193, Oct. 1978.

[59] E. Bassous, "Fabrication of novel three-dimensional microstructures by the anisotropic etching of (100) and (110) silicon," *IEEE Trans. Electron Devices*, vol. ED-25, no. 10, pp. 1178-1185, Oct. 1978.

[60] K.E. Peterson, "Silicon as a mechanical material," *IEEE Trans. Electron Devices*, vol. ED-70, no. 5, p. 420, May 1982.

[61] K.E. Peterson, "Silicon sensor technologies," *Proc. International Electron Devices Meeting*, Washington D.C., pp. 2-7, 1985.

[62] C.D. Fung, P.W. Cheung, W.H. Ko, and D.G. Fleming, *Micromachinig and Micropackaging of Transducers*, Elsevier Science Publishing Company Inc., New York, 1985.

[63] Boron+ Planar Sources, Type GS-245, Owens Illinois, Inc.

[64] J.M. Crishal and A.L. Harington, "A selective etch for elemental silicon," *Electrochem. Soc. Extended Abstract (Spring Meeting)*, 1962, Los Angeles, CA, Abstract. no. 89.

[65] M. Hirata, S. Suwazono, and H. Tanigawa, "A silicon diaphragm formation for pressure sensor by anodic oxidation etch-stop," *Proc. International Conference on Solid-State Sensors and Actuators*, pp. 287-290, June 1985.

[66] D.B. Lee, "Anisotropic etching of silicon," *J. Appl. Phys.*, vol. 40, no. 11, pp. 4569-4574, Oct. 1969.

[67] M.J. Declercq, L. Gerzberg, and J.D. Meindl, "Optimization of the hydrazine-water solution for anisotropic etching of silicon in integrated circuit technology," *J. Electrochem. Soc.*, vol. 122, no. 4, pp. 545-552, Apr. 1975.

[68] Prefrential Silicon Etchant, Type PSE-100, Transene Company, Inc., Bulletin No. 207, Nov. 1982.

[69] Boron+ Planar Sources, Product Bulletin 415, Owens Illinois, Inc.

[70] S.K. Ghandhi, *VLSI fabrication principles*, John Wiley & Sons, New York, 1983.

[71] Hydrazine Badge, American Gas and Chemicals, Type H-5-R, New York, NY.

[72] Y.S. Lee and K.D. Wise, "A batch-fabricated silicon capacitive pressure transducer with low temperature sensitivity," *IEEE Trans. Electron Devices*, vol. ED-29, no. 1, pp. 42-48, Jan. 1982.

[73] W.H. Ko, M.H. Bao, and Y.D. Hong, "A high-sensitivity integrated-circuit capacitive pressure transducer," *IEEE Trans. Electron Devices*, vol. ED-29, no. 1, pp. 48-56, Jan. 1982.

[74] J.G. Smits, H.A.C. Tilmans, and T.S.J. Lammerink, "Pressure dependence of resonant diaphragm pressure sensor," *Proc. International Confrence on Solid-State Sensors and Actuators*, pp. 93-96, June 1985.

[75] T.S.J. Lammerink and W. Wlodarski, "Integrated thermally excited resonant diaphragm pressure sensor," *Proc. International Conference on Solid-State Sensors and Actuators*, pp. 97-100, June 1985.

[76] K.J. Chun and K.D. Wise, "A capacitive silicon tactile imaging array, *Proc. International Conference on Solid-State Sensors and Actuators*, pp. 22-25, June 1985.

[77] K. Chun and K.D. Wise, "A high-performance silicon tactile imager based on a capacitive cell," *IEEE Trans. Electron Devices*, vol. ED-32, no. 7, pp. 1196-1201, July 1985.

[78] D.L. Polla, R.M. White, and R.S. Muller, "Integrated chemical-rection sensor," *Proc. International Confrence on Solid-State Sensors and Actuators*, pp. 33-36, June 1985.

[79] A. Hanneborg, T.E. Hansen, P.A. Ohlckers, E. Carlson, B. Dahl, and O. Holwech, "A new integrated capacitive pressure sensor with frequency modulated output," *Proc. International Conference on Solid-State Sensors and Actuators*, pp. 186-188, June 1985.

[80] R.S. Hijab and R.S. Muller, "Micromechanical thin-film cavity structures for low pressure and acoustic transducer applications, *Proc. International Conference on Solid-State Sensors and Actuators*, pp. 178-181, June 1985.

[81] C.W. Wilmsen, E.G. Thompson, and G.H. Meissner, "Buckling of thermally grown $SiO_2$ thin films," *IEEE Trans. Electron Devices*, vol. ED-19, no. 1, p. 122, Jan. 1972.

[82] R.D. Jolly and R.S. Muller, "Miniature cantilever beams fabricated by anisotropic etching of silicon," *J. Electrochem. Soc.*, vol. 127, no. 12, pp. 2750-2756, Dec. 1980.

[83] K.E. Peterson, "Dynamic micromechanics on silicon: techniques and devices," *IEEE Trans. Electron Devices*, vol. ED-25, no. 10, pp. 1241-1250, Oct. 1978.

[84] W. Benecke, L. Csepregi, A. Heuberger, K. Kuhl, and H. Seidel, "A frequency-sensitive, piezoresistive silicon vibration sensor, *Proc. International Conference on Solid-State Sensors and Actuators*, pp. 105-108, June 1985.

[85] K. Warren, "An improved monolithic accelerometer," *Proc. IEEE Solid-State Sensor Conferenece*, Hilton Head Island, pp. 28-30, June 1984.

[86] J.C. Greenwood, "Etched silicon vibrating sensor," *J. Phys. E: Sci. Instrum.*, vol. 17, pp. 650-652, 1984.

[87] K.D. Wise, M.G. Robinson, and W.J. Hillegas, "Solid-state process to produce hemispherical components for inertial fusion targets," *J. Vac. Sci. Technol.*, vol. 18, no. 3, pp. 1179-1182, Apr. 1981.

[88] K.H. Nicholas, I.J. Stemp, and H.E. Brockman, "Dielectric isolation by orientation-dependent etching," *Electronic Letters*, vol. 20, no. 24, pp. 1014-1015, Nov. 1984.

[89] B. Petit and J. Pelletier, "A novel processing technique for the fabrication of thick silicon grids by anisotropic etching," *J. Electrochem. Soc.*, vol. 132, no. 4, pp. 982-984, Apr. 1985.

[90] P.W. Barth, P.J. Shlichta, and J.B. Angell, "Deep narrow vertical-walled shafts in (110) silicon," *Proc. International Conference on Solid-State Sensors and Actuators*, pp. 371-373, June 1985.

[91] S. Sriram and E.P. Supertzi, "Novel V-groove structures on silicon," *Applied Optics*, vol. 24, no. 12, pp. 1784-1787, June 1985.

[92] K.D. Wise and K. Najafi, "A micromachined integrated sensor with on-chip self-test capability," *Proc. IEEE Solid-State Sensor Conference*, Hilton Head Island, pp. 12-16, June 1984.

[93] K. Najafi, K.D. Wise, and T. Mochizuki, "A high-yield IC-compatible multichannel recording array," *IEEE Trans. Electron Devices*, vol. ED-32, no. 7, pp. 1206-1211, July 1985.

[94] D.S. Campbell, "Mechanical properties of thin films," in L.I. Maissel and R. Glang, Eds., *Handbook of Thin Film Technology*, McGraw-Hill, New York, pp. 12-24, 1970.

[95] R.J. Jaccodine and W.A. Schlegel, "Measurement of strain at Si-$SiO_2$ interface," *J. Appl. Phys.*, vol. 37, no. 6, pp. 2429-2434, May 1966.

[96] J.W. Beams, "Mechanical properties of thin films of gold and silver," in C.A. Neugebauer, J.B. Newkirk, and D.A. Vermilyea, Eds., *Structure and Properties of Thin Films*, John Wiley & Sons, New York, pp. 183-192, 1959.

[97] W.K. Ford, Jr., A.L. Stamper, and J.W. Beams, "Mechanical strength of thin films of silver and gold," *Bull. Am. Phys. Soc. II*, vol. 1, p. 333, 1956.

[98] D.B. Kraft, T.P. Strider, and J.W. Beams, "Mechanical properties of thin metallic films," *Bull. Am. Phys. Soc. II*, vol. 3, p. 299, 1958.

[99] R. Papirno, "Stress and strain in thin films bulged over circular opennings," *J. Appl. Phys.*, vol. 32, pp. 1175-176, 1962.

[100] S. Jovanovic and C.S. Smith, "Elastic modulus of amorphous nickel films," *J. Appl. Phys.*, vol. 32, pp. 121-122, 1961.

[101] A. Catlin and W.P. Walker, "Mechanical properties of thin single-crystal gold films," *J. Appl. Phys.*, vol. 31., no. 12, pp. 2135-2139, Dec. 1960.

[102] H. Leidheiser, Jr.G and B.W. Sloop, "Mechanical properties of copper films," *J. Appl. Phys.*, vol. 41, no. 1, pp. 402-406, Jan. 1970.

[103] W.M.C. Yang, T. Tsakalakos, and J.E. Hilliard, "Enhanced elastic modulus in composition-modulated gold-nickel and copper-palladium foils," *J. Appl. Phys.*, vol. 48, no. 3, pp. 876-879, Mar. 1977.

[104] T. Tsakalakos and J.E. Hilliard, "Elasic modulus in composition-modulated copper-nickel foils," *J. Appl. Phys.*, vol. 52, no. 2, pp. 734-737, Feb. 1983.

[105] W.Y. Pickhardt and D.L. Smith, "Fabrication of high-strength unsupported metal membranes," *J. Vac. Sci. Technol.*, vol. 14, no. 3, pp. 823-825, May/June 1977.

[106] J.L. Vossen, J.J. O'Niell, Jr., O.R. Mesker, and E.A. James, "Extremely high stress in graded interfacial layers: Thin films of HF on sapphire," *J. Vac. Sci. Technol.*, vol. 14, no. 1, pp. 85-87, Jan./Feb. 1977.

[107] G. Gerard and R. Papirno, "Dynamic biaxial stress-strain characteristics of aluminium and mild steel," *Trans. Am. Soc. Metals*, vol. 49, pp. 132-148, 1957.

[108] A. Gleyzal, "Plastic deformation of a circular diaphragm under pressure," *J. Appl. Mechanics, ASME*, vol. 15, no. 3, p.288, 1949.

[109] G. Sachs, G. Espey, and G.B. Kasik, "Circular bulging of aluminum-alloy sheet at room and elevated temperatures," *Transactions, ASME*, vol. 68, no. 2, p. 161, 1946.

[110] W.F. Brown, Jr. and G. Sachs, "Strength and failure characteristics of thin circular membranes," *Transactions, ASME*, vol. 70, no. 3, p. 241, 1948.

[111] J.G. Williams, *Fracture mechanics of polymers*, Ellis Horwood Limited, England, ch. 2, 1984.

[112] H. Dannenberg, "Measurement of adhesion by a blister method," *J. Appl. Polymer Sci.*, vol. 5, no. 14, pp. 125-134, 1961.

[113] M.L. Williams, "The continuum interpretation for fracture and adhesion," *J. Appl. Polymer Sci.*, vol. 13, pp. 29-40, 1969.

[114] S. Timoshenko and S. Woinowsky-Krieger, *Theory of plates and shells*, 2nd ed., McGraw-Hill, New York, 1959.

[115] A.C. Ugural, *Stresses in plates and shells*, McGraw-Hill, New York, ch. 8, 1981.

[116] L.H. Donnell, *Beams, plates, and shells*, McGraw-Hill, New York, ch. 4-5, 1976.

[117] W.D. Weber and M.R. Gupta, "Molecular weight/property relationships in a series of polyimide copolymers," *Proc. Second International Conference on Polyimides*, pp. 335-350, Oct. 1985.

[118] Pressure Transducer, Type LQ-5-516, Kulite Semiconductor Products, Inc.

[119] Pressure Transducer, Type 140PC, Micro Switch, A Honeywell Division.

[120] P. Geldermans, C. Goldsmith, and F. Bedetti, "Measurement of stresses created during cureing and in cured polyimide films," in K.L. Mittal, Ed., *Polyimides*, Plenum Press, NY, Vol. 2, pp. 695-711, 1984.

[121] L.B. Rothman, "Properties of thin polyimide films," *J. Electrochem. Soc.*, vol. 127, no. 10, pp. 2216-2220, Oct. 1981.

[122] H. Guckel, T. Randazzo, and D.W. Burns, " A simple technique for the determination of mechanical strain in thin films with application to polysilicon," *J. Appl. Phys.*, vol. 57, no. 5, pp. 1671-1675, Mar. 1985.

[123] R.B. Hopkins, *Design Analysis of Shafts and Beams*, McGraw-Hill, N.Y., p. 250, 1970.

[124] J.M. Gere and S.P. Timoshenko, *Mechanics of Materials*, PWS Publishers, Boston, pp. 407-414, 1984.